UNIVERSITY OF CALIFORNIA
Los Angeles

J/Ψ Production in Au+Au Collisions at $\sqrt{s_{NN}} = 200$ GeV

A dissertation submitted in partial satisfaction
of the requirements for the degree
Doctor of Philosophy in Physics

by

Johan Enmanuel Gonzalez

2006

The dissertation of Johan Enmanuel Gonzalez is approved.

Hong Wu

Nu Xu

Chun W. Wong

Charles Whitten Jr.

Huan Z. Huang, Committee Chair

University of California, Los Angeles

2006

To my siblings José and Iola . . .

who—among so many other things—

refused to be at the mercy of the wind

Table of Contents

List of Figures

List of Tables

ACKNOWLEDGMENTS

First, I would like to thank my advisor, Huan Huang, and my other mentors at UCLA, Charles Whitten and George Igo, for their guidance and for providing me with the resources and opportunity to grow in the field. I feel particularly lucky to have worked with Huan because he often granted me the freedom to pursue my own ideas. I would like give special thanks to Zhangbu Xu for taking me under his wing during my first days in STAR. Zhangbu showed exemplary patience and understanding during my initial struggles with the STAR analysis software. I would also like to take a moment to give special thanks to Nu Xu for all the support and fatherly advice he provided me during my stay at the Lawrence Berkeley National Laboratory.

I want to give thanks to my fellow UCLA graduate students and the folks at LBL for all the good times and without whom I would still be debugging C++ code. I'd like to thank the people in the spectra and heavy flavor working groups for providing me with constant peer review and making sure I made effective use of the scientific method. I am eternally thankful of having been part of the STAR collaboration and part of such a tremendous scientific endeavor.

Vita

June 14, 1979	Born, Santo Domingo, Dominican Republic
1992	Migrated to United States
2001	B.A. Physics Florida State University
2002	M.S. Physics University of California – Los Angeles
Fall, 2002	Teaching Assistant Department of Physics and Astronomy University of California – Los Angeles
Fall, 2003	Teaching Assistant Department of Physics and Astronomy University of California – Los Angeles
Spring, 2004	Teaching Assistant Department of Physics and Astronomy University of California – Los Angeles
2002–2006	Graduate Research Assistant Intermediate Energy Group University of California – Los Angeles

Publications

J. Adams *et al.*

Evidence from d+Au measurements for final-state suppression of high p_T hadrons in Au+Au collisions at RHIC.

Phys. Rev. Lett. **91** (2003) 072304.

J. Adams *et al.*

Identified particle distributions in pp and Au+Au collisions at $\sqrt{s_{NN}} = 200$ GeV

Phys. Rev. Lett. **92** (2004) 112301.

J. Adams *et al.*

Measurements of transverse energy distributions in Au+Au collisions at $\sqrt{s_{NN}} = 200$ GeV

Phys. Rev. C **70** (2004) 054907.

J. Adams *et al.*

K(892)* Resonance Production in Au+Au and p+p Collisions at $\sqrt{s_{NN}} = 200$ GeV at STAR

Phys. Rev. C **71** (2005) 064902.

J. Adams *et al.*

Φ meson production in Au+Au and p+p collisions at $\sqrt{s_{NN}} = 200$ GeV

Phys. Lett. B **612** (2005) 181.

J. Adams *et al.*

Pion, kaon, proton and anti-proton transverse momentum distributions from p+p and d+Au collisions at $\sqrt{s_{NN}} = 200$ GeV.

Phys. Lett. B **616** (2005) 8.

J. Adams *et al.*
Open charm yields in d+Au collisions at $\sqrt{s_{NN}} = 200$ GeV
Phys. Rev. Lett. **94** (2005) 062301.

J. Adams *et al.*
Experimental and Theoretical Challenges in the Search for the Quark Gluon Plasma: The STAR Collaboration's Critical Assessment of the Evidence from RHIC Collisions
Nucl. Phys. A **757** (2005) 102.

J. Adams *et al.*
Distributions of Charged Hadrons Associated with High Transverse Momentum Particles in p+p and Au+Au Collisions at $\sqrt{s_{NN}} = 200$ GeV
Phys. Rev. Lett. **95** (2005) 152301.

J. Gonzalez *et al.*
Pseudorapidity Asymmetry and Centrality Dependence of Charged Hadron Spectra in d+Au Collisions at $\sqrt{s_{NN}} = 200$ GeV
Phys. Rev. C **70** (2004) 064907.

ABSTRACT OF THE DISSERTATION

J/Ψ Production in Au+Au Collisions at $\sqrt{s_{NN}} = 200$ GeV

by

Johan Enmanuel Gonzalez

Doctor of Philosophy in Physics
University of California, Los Angeles, 2006
Professor Huan Z. Huang, Chair

The first STAR measurements of J/ψ meson production in $Au+Au$ collisions at $\sqrt{s_{NN}} = 200$ GeV are reported. Using the STAR Time Projection Chamber, J/ψ mesons were reconstructed via the dielectron decay channel. Scrutiny of the dielectron invariant mass spectrum in minimum bias events revealed a signal of 3.5σ significance. A systematic study of the scaled invariant yields as a function of collision centrality was carried out. In central events, where no significant signal was found, an upper limit on the invariant yield was quoted. Comparisons of the measured J/ψ scaled invariant yields to the expectations of a Statistical Hadronization model were made. Our findings rule out the possibility of strong enhancement of J/ψ production through the coalescence of charm-anticharm pairs via the mechanism of Statistical Hadronization.

CHAPTER 1

Introduction

The quest to explore the subatomic realm began with the first and lowest energy nuclear collisions performed by Ernest Rutherford. By bombarding gold atoms with alpha particles, Rutherford was able to resolve the charged nucleus inside the neutral atom. Since then, increasingly high energy collisions have been able to resolve the existence of nucleons and eventually smaller constituents bound within these nucleons. Rapid evolution of new theoretical and experimental techniques lead to the development of the Standard Model (SM) of particle physics. The SM provides a comprehensive description of the fundamental particles and their interactions (Figure 1.1). The component of the SM that describes the strong interaction of subatomic particles is called Quantum Chromodynamics (QCD). In QCD, the structure of the protons and neutrons (or more generally hadrons) that comprise most of the Universe is understood in terms of elementary entities (*quarks*) that are held together by the so-called Strong force. These elementary entities interact so strongly that they can only be directly observed in "color-neutral" groups of two (mesons) or three (baryons).

The primary goal of relativistic heavy ion collisions is to produce matter where the quarks effectively decouple from hadrons and behave as quasi-free particles. This new state of matter is known as the Quark-Gluon Plasma (QGP), which can be formally defined to be *a (locally) thermally equilibrated state of matter in which quarks and gluons are deconfined from hadrons, so that color degrees of freedom*

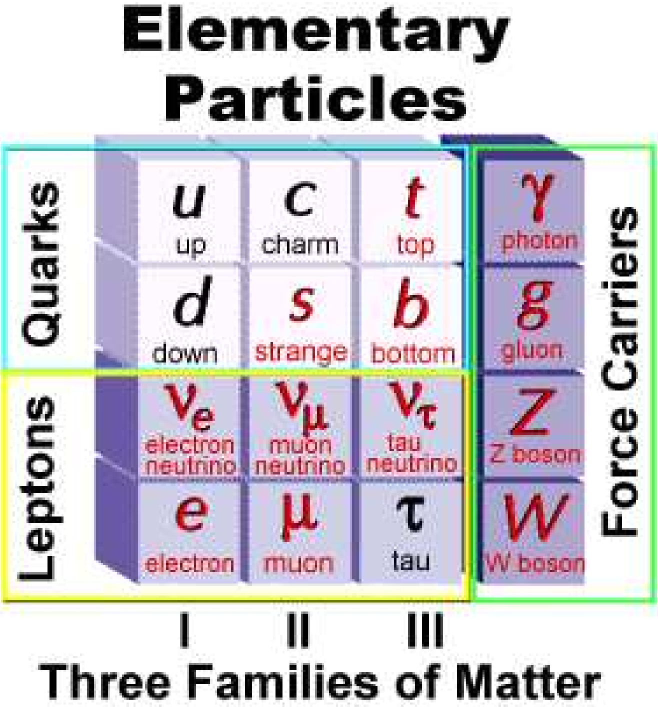

Figure 1.1: The elementary particles and forces contained in the Standard Model.

become manifest over nuclear, rather than merely nucleonic, volumes [Ada05a]. The mere observation of the QGP, while the subject of intense experimental effort, is by no means the ultimate goal. More generally, the goal of relativistic heavy ion physics is to understand QCD at extreme temperatures and energy over large volumes. Under such extraordinary conditions, it is believed that the symmetries of QCD will reveal themselves: color will be deconfined and chiral symmetry will be restored. The conditions that would give rise to such a scenario are believed to have occurred in nature microseconds after the “Big Bang”, and presumably at the center of very dense neutron stars. The environment created by heavy ion collisions is currently the only means in the laboratory to study QCD in the macroscopic limit. Figure 1.2 shows a QCD phase diagram and the means by which relativistic heavy ion collisions make the exploration of this landscape possible.

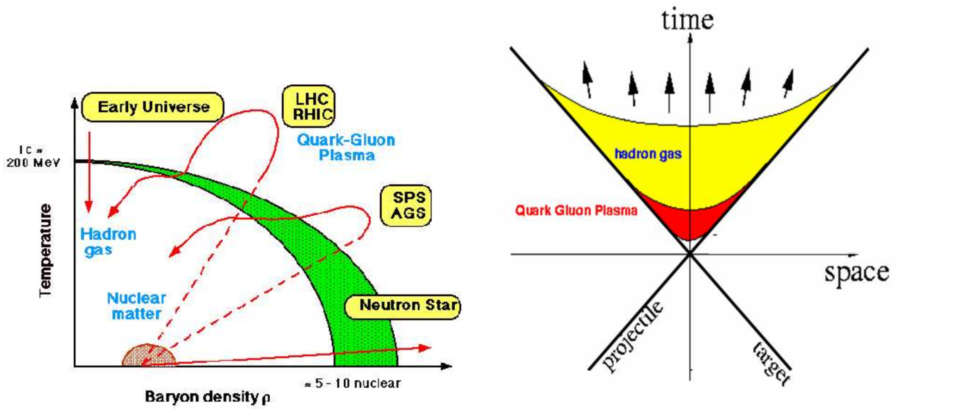

Figure 1.2: The left panel illustrates the QCD phase diagram (taken from [Yam01]). The major features of the QCD phases possibly accessible in nature and heavy ion collisions are shown. The right panel shows the expected evolution of a nuclear collision. The Quark-Gluon Plasma stage lasts approximately 10 fm/c.

In the past, high-energy nuclear accelerator experiments were conducted with the hope of observing deconfinement and chiral symmetry restoration. These first few experiments were of the "fixed target" type, primarily accelerating ions to speeds approaching the speed of light and smashing them into a target of similar heavy ions. Great focus was applied in the late 1990s to symmetric systems of gold beams on gold targets at Brookhaven National Laboratory's Alternating Gradient Synchrotron (AGS) and lead beams on lead targets at CERN's Super Proton Synchrotron (SPS). Results from the AGS and the SPS proved that a direct observation of the QGP through the "haze" created by hadronic interactions is difficult. In other words, in heavy ion collisions it is difficult to disentangle novel phenomena from ordinary nuclear effects. Currently, high-energy nuclear physics experiments are being conducted at Brookhaven National Laboratory's Relativistic Heavy Ion Collider (RHIC). By virtue of being a collider, RHIC achieves energies that are 10 times greater than the previous energies studied in relativistic heavy ion collisions. With its nucleus-nucleus collisions at unprecedented high energy density and temperature, RHIC provides the unique scientific opportunity to better understand QCD in the high density and high temperature regime.

1.1 Overview of Relativistic Heavy-ion Collisions

1.1.1 Quantum Chromodynamics

As previously discussed, Quantum Chromodynamics (QCD) is the theory of the strong interaction, a fundamental force describing the interactions of the quarks and gluons found in nucleons. QCD is a quantum field theory of a special kind called a non-Abelian gauge theory. QCD is an unbroken $SU(3)$ color gauge theory, one of the two components of the SM, the other one being the spontaneously broken $SU(2)\times U(1)$ electroweak theory. QCD enjoys two peculiar properties:

- **asymptotic freedom**, which means that at very high momentum transfer or very short distances, quarks and gluons interact very weakly. That QCD possesses this property was first discovered in the early 1970s by David Politzer and by Frank Wilczek and David Gross. For this work they were awarded the 2004 Nobel Prize in Physics.

- **confinement**, which means that the force between quarks does not diminish as they are separated. Because of this, it would take an infinite amount of energy to separate two quarks; they are forever bound into hadrons such as the proton and the neutron. Although analytically unproven, confinement is widely believed to be true because it explains the consistent failure of free quark searches.

With the invention of bubble chambers and spark chambers in the 1950s, experimental particle physics discovered a large and ever-growing number of hadrons. It seemed that such a large number of particles could not all be fundamental. First, the particles were classified by charge and isospin; then (in 1953) according to strangeness by Murray Gell-Mann and Kazuhiko Nishijima. To gain greater insight, the hadrons were sorted into groups having similar properties and masses using the eightfold way, invented in 1961 by Gell-Mann and Yuval Ne'eman. Gell-Mann and George Zweig went on to propose in 1963 that the structure of the groups could be explained by the existence of three flavors of smaller particles inside the hadrons: the aforementioned quarks.

At this stage, one particle, the Δ++ remained mysterious; in the quark model, it is composed of three up quarks with parallel spins. However, since quarks are fermions, this combination is forbidden by the Pauli exclusion principle. In 1965, Moo-Young Han with Yoichiro Nambu and Oscar W. Greenberg independently resolved the problem by proposing that quarks possess an additional $SU(3)$ gauge degree of freedom, later called color charge. Han and Nambu noted that quarks would interact via an octet of vector gauge bosons: the gluons. Unlike the neutral photon of Quantum Electrodynamics (QED), gluons themselves participate in strong interactions. The gluon has the ability to do this as it itself carries the color charge and so interacts with itself, making QCD significantly harder to analyze than QED.

Since free quark searches consistently failed to turn up any evidence for the new particles, it was then believed that quarks were merely convenient mathematical constructs, not real particles. Richard Feynman argued that high energy experiments showed quarks to be real: he called them *partons* (since they were parts of hadrons). James Bjorken proposed that certain relations should then hold in deep inelastic scattering of electrons and protons, which were spectacularly verified in experiments at SLAC in 1969.

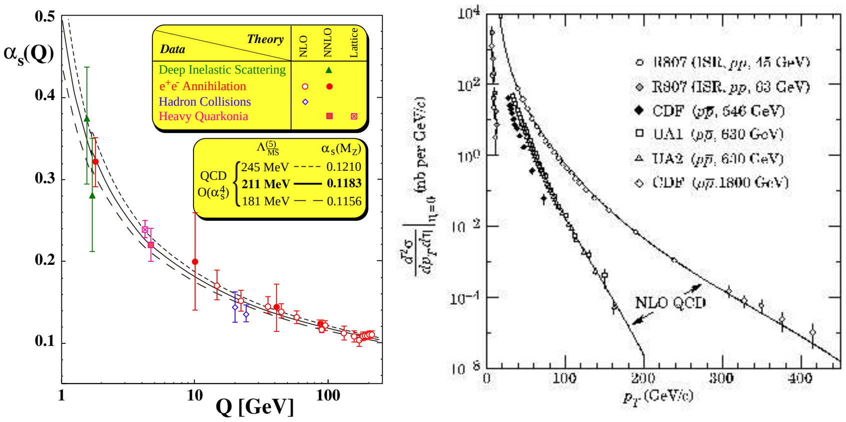

Figure 1.3: The left panel shows the QCD running coupling constant $\alpha_s(Q)$ determined from a variety of processes. Figure taken from [Bet03]. The right panel (taken from [Eid04]) shows differential cross sections for the observation of a single jet of pseudorapidity $\eta = 0$ as a function of the transverse momentum of the jet, which is well described by perturbative QCD.

Although the study of the strong interaction remained daunting, the discovery of asymptotic freedom by David Gross, David Politzer and Frank Wilczek allowed people to make precise predictions of the results of many high energy experiments using the techniques of perturbation theory. The dependence on the QCD coupling, α_s, on momentum transfer, Q, is shown in Figure 1.3(left panel) from various experiments. At sufficiently high energies, $\alpha_s \rightarrow 0$, the quarks and gluons behave as free particles. A lowest order QCD calculation parameterizes the above data as

$$\alpha_s(Q^2) = \frac{1}{\beta_0 \ln Q^2/\Lambda^2} \tag{1.1}$$

where β_0 is a constant that depends on the number of active quark flavors and Λ is the energy scale where $\alpha_s(Q^2)$ diverges to infinity. The Λ parameter in the lowest order calculation is approximately 0.1 GeV and effectively sets the lower bound for the predictive power of QCD. The left panel of Figure 1.3 shows fits to the data from higher order calculations which illustrate the model dependent variance of Λ.

QCD has been extensively verified by experiment. Shown in Figure 1.3(right panel) are next-to-leading order (NLO) calculations that beautifully describe data from $p + \overline{p}$ collisions at 630 GeV and 1800 GeV. Furthermore, evidence of gluons was discovered in three jet events at PETRA in 1979. Experiments became more and more precise, culminating in the verification of perturbative QCD at the level of a few percent at the LEP in CERN.

The other side of asymptotic freedom is confinement ($\alpha_s \rightarrow \infty$). Since the force between color charges does not decrease with distance, it is believed that quarks and gluons can never be liberated from hadrons. This aspect of the theory is verified within lattice QCD computations, the topic of our next discussion.

1.1.2 Lattice QCD and Deconfinement

Lattice Quantum Chromodynamics (Lattice QCD) is the QCD theory of quarks and gluons formulated on a space-time lattice. Analytic or perturbative solutions in QCD are hard or impossible due to the highly nonlinear nature of the strong force. Lattice QCD is a computational approach to solve QCD. In principle, it is exact, but practical implementations employ many approximations. This approach uses a discrete set of space-time points (called the lattice) to reduce the analytically intractable path integrals of the continuum theory to a very difficult numerical computation which is then carried out on supercomputers. The formulation of QCD on a discrete rather than continuous space-time resolves many difficulties (e.g. divergences) associated with the continuum field theories. While it is a slow and resource-intensive approach, it has wide applicability, giving insight into parts of the theory inaccessible by other means.

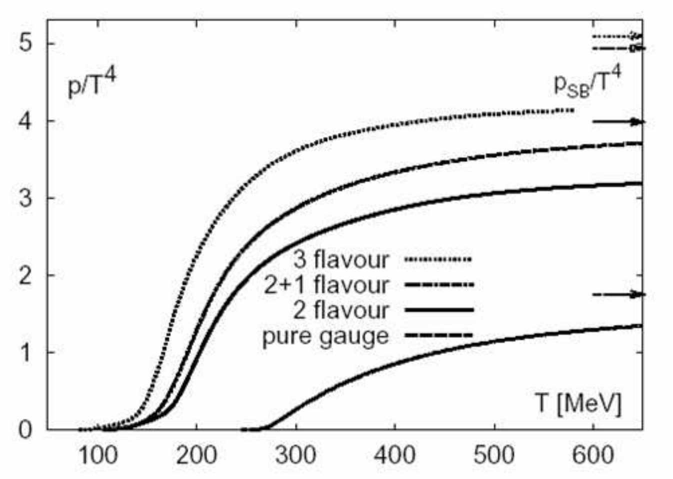

Figure 1.4: Various kinds of Lattice QCD calculations predict a sudden jump in the effective number of degrees of freedom in systems heated beyond ~170 MeV. Figure is taken from [Kar02]

Lattice QCD calculations portend a number of exciting phenomena. First there is the transition of normal nuclear matter to the QGP. This phase transition, of which it is not clear whether it is of first or second order, will lead to a dramatic jump in the energy density of the state at a certain critical temperature T_c. This temperature is expected to be around 170 MeV, which is more than 100,000 times the temperature of the sun's core. The approximately six-fold increase in energy density, a density many orders of magnitude higher than that of water, is due to the increase in number of degrees of freedom (Figure 1.4): there are more states available to the quarks and gluons in different spin and colour states than there are states available to hadrons. The second important prediction is another transition to a state in which chiral symmetry is restored. Chiral symmetry essentially implies that the number of left-handed quarks is not related to the number of right-handed quarks anymore. This chiral symmetry is spontaneously broken in our normal world, but will be restored at about the same temperature of 170 MeV.

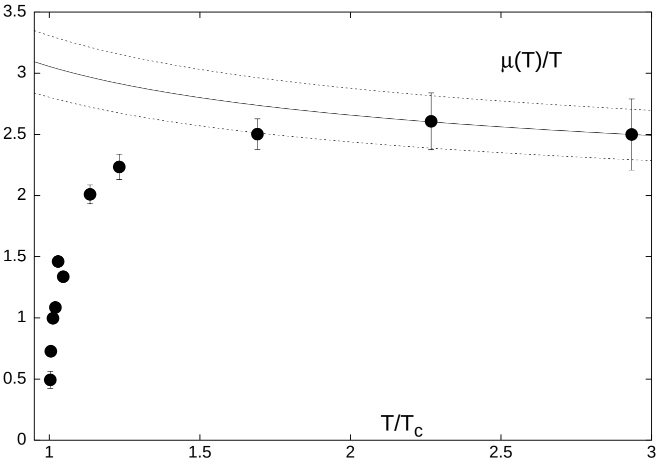

Figure 1.5: Temperature-dependence of the heavy-quark screening mass (divided by temperature) as a function of temperature (in units of the phase transition temperature), from Lattice QCD calculations. The curves represent perturbative expectations of the temperature-dependence. Figure is taken from [KKL00]

Of interest to this analysis is another intruiging prediction by Lattice QCD. Calculations have converged on the fact that above T_c, the effective potential between a heavy quark-antiquark pair takes the form of a screened Coulomb potential, with screening mass (or inverse screening length) rising rapidly as temperature increases above T_c [KKL00]. As seen in Figure 1.5, the screening mass deviates strongly from perturbative QCD expectations in the vicinity of T_c , indicating large non-perturbative effects. The increased screening mass leads to a shortening of the range of the heavy $q\overline{q}$ interaction, and to an anticipated suppression of charmonium production. The notion of (Debye) color screening can be understood by considering solid hydrogen [KS86]. Under ordinary pressures, it is an insulator; the proton and electron are bound, and the solid consists of these bound states. At sufficiency high density, however, a transition to metallic hydrogen is expected, with non-zero electric conductivity and "deconfined" electrons. With increasing density, the electric charge of the proton, as seen by "its" electron, becomes Debye-screened due to the presence of other protons and electrons. When the Debye radius λ_D has reached the size of the atomic radius, the screening neutralizes the Coulomb force previously binding the proton and electron: the electrons are then quasi-free in the lattice, thus giving rise to a metal. According to Lattice QCD calculations, the an analogous situation occurs in a lattice of strongly interacting matter, where the normal hadron matter—a color insulator—is turned into a color conducting QGP.

In the following sections, we will discuss how scrutiny of heavy flavor production in relativistic heavy ion collisions can help validate this attribute of Lattice QCD and, in turn, help verify the formation of the QGP at RHIC.

1.2 Probing QCD Matter with Heavy Quarks

Heavy ion collisions represent our best opportunity to make the QGP in the laboratory, but we place exceptional demands on these collisions: they must not only produce the matter, but then must serve "pump and probe" functions. The goal is to probe this strongly interacting matter, so we do what comes naturally to high-energy physicists: we send "something" in to scatter off of this high-density matter. Unfortunately, we lack the ∼1 fm wavelength laser that would be so ideal for this task. One can follow the suggestion of Bjorken and use hard-scattered partons, created in the earliest stages of the very same collision, as our probe of the medium. The interaction of these energetic particles with the medium provides a class of unique, penetrating probes that are analogous to the method of computed tomography (CT) in medical science. Other possible efforts to probe the strongly interacting matter involve studying electroweak collision products, where the absence of final-state interactions with the evolving strongly interacting matter is exploited, hoping to isolate those produced during the early collision stages and bearing the imprints of the bulk properties characterizing those stages, e.g. thermal leptons and photons [Joh02]. But those experimental endeavors must deal with the relative scarcity of such products, and competing origins from hadron decay and interactions during later collision stages. Most of the RHIC results to date utilize instead the far more abundant produced hadrons, some of which (through a lack of hadronic interactions) can carry information from the initial stages of the collision, such as the ϕ meson [Yam01]. In this analysis, we focus on probing the medium using heavy quarks, charm quarks in particular, produced in the inital stages of the collision.

1.2.1 Charm Quarks as Probes of Initial Stages

Because of their large mass, charm quarks can only be created in the initial, most energetic epoch of the collision. This is known as the hard-scattering stage of the collision. One of the attractive features of charm quarks is that they can be readily treated with perturbative QCD (pQCD). This is in distinct contrast to the production of particles of light quarks which can be evaluated within the pQCD framework only for sufficiently large momenta. Charm quarks are primarily produced via gluon fusion, as illustrated in Figure 1.6. NLO calculations

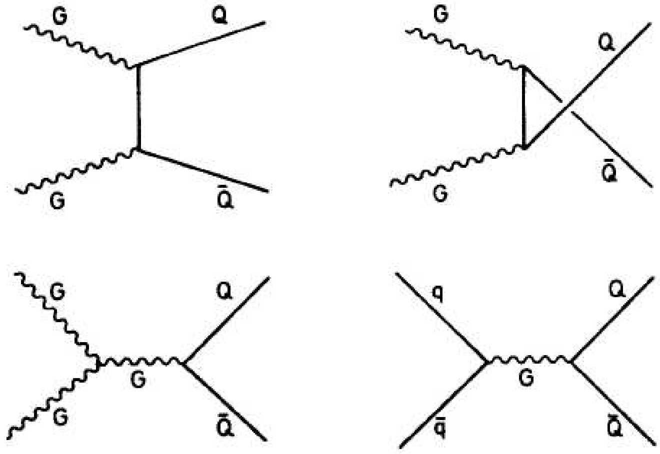

Figure 1.6: The dominant Feynman diagrams for charm production.

add more complicated diagrams but most of these still involve gluons. While the vast majority of charm quark pairs coming from gluon fusion hadronize into particles carrying open charm, some of the produced pairs form bound charmonia. The former not only provide a crucial baseline for charmonia measurements but also are of prime interest on their own. Figure 1.7 illustrates the fact that charm quarks can be used to probe the hot, dense medium produced in relativistic heavy ion collisions. Recent studies [Adl06b] have used the semileptonic decays of open charm hadrons to infer the nuclear modification factor of heavy quarks, with the results indicating substantial heavy quark energy loss in the medium.

Of interest to this analysis is the production of charmonium (charm-anticharm) bound states created in the initial stages of the collision. Among these, the 1S state, also known as the J/ψ meson, is the most notable one. The J/ψ meson was discovered in 1974 by experimenters at Stanford (Burton Richter) and Brookhaven National Laboratory (Samuel Ting). Slightly more than three times as massive as the proton (M = 3.096 GeV/c^2), this particle decayed slowly and didn't fit into the framework of the up, down, and strange quarks. The discov-

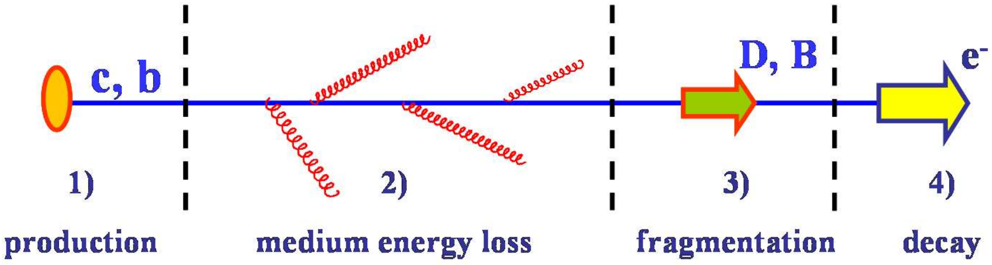

Figure 1.7: Diagram of heavy quark production, propagation and modification in the medium, and observation. Figure taken from [Djo05].

ery of the J/ψ was the first firm experimental evidence for the fourth quark. Richter and Ting shared the 1976 Nobel Prize for their discovery. The χ_c ($M =$ 3.42 GeV/c^2) and the ψ' ($M =$ 3.68 GeV/c^2) are some of the excited states of charmonium. These higher charmonium states are currently out of experimental reach due to limited RHIC luminosities. Therefore, in this analysis we only focus on measuring J/ψ production in STAR.

The J/ψ meson has long been thought of as the probe of "Smoking Gun" quality—the kind of probe that could definitively prove the formation of a QGP in relativistic heavy ion collisions. Both calculations performed by Matsui and Satz [MS86] in the 1980s and Lattice QCD results (of the time) predicted that charmonium bound states would "melt" in the QGP, and that this process would lead to a suppression of charmonium yields when compared to nominal pQCD calculations. As we will show in Section 1.2.3, the fate of the J/ψ in relativistic heavy ion collisions could, in fact, be even more interesting than people originally thought. Recent theoretical developments state that J/ψ's may be spawned from coalescence of thermal charm-anticharm pairs in the final stages of the collision, which could, for sufficiently high parton densities, lead to an enhacement of charmonium yields when compared to nominal pQCD calculations. In Section 1.2.4, we will briefly touch upon a number of ideas that can help us discriminate among enhacement and suppression scenarios.

1.2.2 J/ψ Dissociation Mechanisms

The story of the J/ψ in the context of relativistic heavy ion collisions began with a publication in the 1980's by T. Matsui and Helmut Satz [MS86]. Their calculation revolved around the idea of Debye color screening and its effects on the stability of charmonium bound states. Figure 1.8 shows an artist's conception of color screening. Generally speaking, the primordially produced J/ψ's will be subsequently dissociated by:

1. Nuclear absorption
2. Debye color screening or parton-induced destruction in the QGP [Shu78]
3. Inelastic scattering on "co-moving" hadrons in the final, hadron gas phase of the reaction

We will first give a basic overview of the formal treatment of charmonium dissociation, as originally formulated by Matsui and Satz. In ordinary vacuum, the $c\bar{c}$ system will exhibit the following non-relativistic interaction potential[QR79]:

$$V(r) = \sigma r - \frac{\alpha_{eff}}{r} \tag{1.2}$$

where σ is the string tension and α_{eff} is the coulombic interaction coupling. The values of aforementioned parameters are temperature dependent, and for $T = 0$, $\sigma \simeq 0.16$ GeV^2 and $\alpha_{eff} \simeq 1/2$. The energy of the bound state can be estimated semiquantitatively by

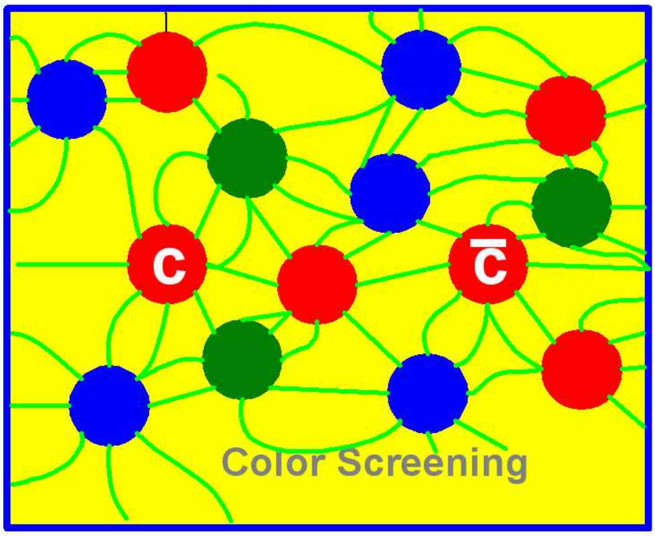

Figure 1.8: A caricature of a charm-anticharm pair subjected to color screening. Picture taken from [Lei06].

$$E(r) = 2m + \frac{1}{2mr^2} + V(r) \tag{1.3}$$

including the c-quark kinetic energy and their rest mass m. Now, with increasing temperature, $\sigma(T)$ decreases, and at at the point of deconfinement $\sigma(T_c) = 0$. Above deconfinement ($T \geq T_c$) it follows that [KS86]

$$V(r) = -(\frac{\alpha_{eff}}{r}) \exp\left(-r/r_D(T)\right) \tag{1.4}$$

is the modified, color-screened coulombic potential, where $r_D(T)$ is the Debye screening radius. This potential can still allow for bound states to form. Pluging Equation1.4 into Equation1.3 and minimizing $E(r)$, one arrives at

$$x(x+1)\exp\left(-x\right) = (m\alpha_{eff}r_D)^{-1} \tag{1.5}$$

with $x \equiv r/r_D$ as the critical condition for a bound state. Invoking Lattice QCD calculations [Cra78], Matsui and Satz then arrive at $r^{max}_{J/\psi}/r_D = 1.61$ as the universal coulombic J/ψ radius at the last point where such a state is possible. They argued that the existence of the J/ψ is excluded down to $T/T_c = 1.2$ or less. The formation of a QGP therefore prevents the formation of a J/ψ bound state already just above T_c. Because deconfinement is an essential ingredient in the arguments formulated here, an observed suppression would imply that there is deconfinement in relativistic heavy ion collisions.

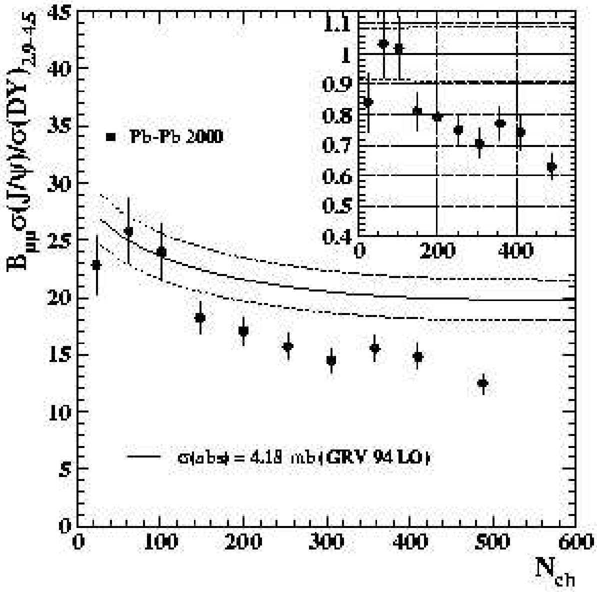

Figure 1.9: The J/ψ cross section scaled by the corresponding Drell-Yan process as a function of charged multiplicity for NA50's Pb-Pb 2000 data sample. The inset shows the ratio of Measured/Expected, i.e. data over normal nuclear absorption. Figure taken from [Ale05].

As enumerated earlier, J/ψ's will also undergo a "normal" suppression of sorts, which will be induced by ordinary nuclear effects. In a heavy ion environment, the first phase of the normal suppression is characterized by interactions of the bound state with interpenetrating nucleons. This leads to a rather well understood ($N_{p1}N_{p2}^{\alpha}$) suppression of the production cross section with $\alpha = 0.92 \pm 0.01$ as inferred from $p - A$ and $A - B$ reactions with light projectile nuclei [HKP01]. The combined effect of all possible modifications due to normal nuclear matter, as well as collisions with co-movers in the hadron gas phase of the collision, is often parametrized in the form of a nuclear absorption cross section. Although the impact of hadronic interactions is not as well understood as nuclear absorption in the initial stages, the effect has been demonstrated to be rather moderate (see, e.g., Ref. [KS94, Hag00]).

The NA38 and NA50 experiments have carried out a systematic study of J/ψ and ψ' production at the CERN-SPS in $p + p$, $p + A$, light ion, and $Pb + Pb$ collisions providing intruiging results. The NA50 experiment observed a suppression, whenceforth dubbed "anomalous" suppression, of J/ψ production in central $Pb + Pb$ collisions at $\sqrt{s_{NN}} = 17.2$ GeV [Abr00]. The suppression, which is of the order of 25% with respect to the normal suppression in nuclear matter (Figure 1.9), has been interpreted by the NA50 authors as evidence for deconfinement of quarks and gluons. This conclusion has not been universally shared, but what is worthy of note is that normal suppression mechanisms can be accounted for and may not impose large, "show-stopping" complications that would hinder the observation of suppression induced by novel mechanisms.

The original treatment of J/ψ suppression was a potential model that was based on a heavy quark interaction which considerably underestimated the actual $c\bar{c}$ potential, and thus grossly overestimated the suppression factor measured by the NA50 experiment. Recent spectral function studies of the behavior of charmonium states in a deconfined medium show that the J/ψ (ground state) can sur-

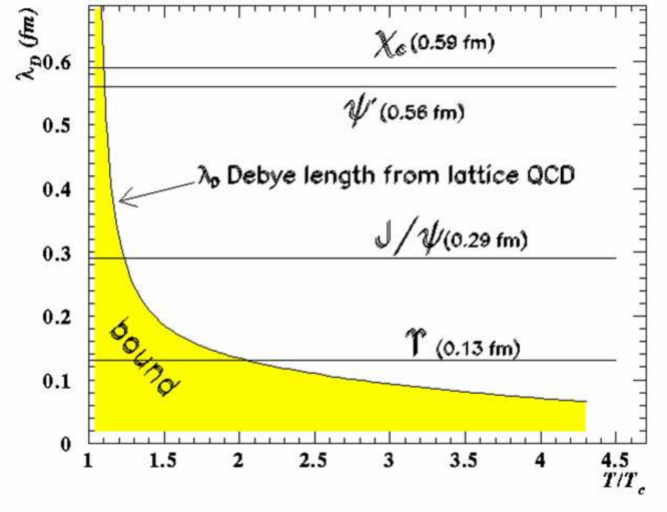

Figure 1.10: Debye screening length as a function of system temperature (in units of T_c). The region in which the various states of charmonium become unbound are indicated by the intersection of the horizontal lines and the yellow region. Recent calculations indicate that the J/ψ and the ground state of *bottomnium*, the Υ, actually become unbound at substantially higher values of T/T_c than shown above. Figure taken from [Lei06].

vive up to 2 - 2.5 T_c [AH04, MOU01, DKW04, Mor05], while the higher excited states seem to dissappear in the vicinity of T_c [DKW04]. New potential model analyses [Won05b, ABD05, Won05a], based on more realistic heavy quark potentials, further support these spectral function studies. The concensus between these different approaches is that there is a hierarchy of suppression temperatures, which leads to a sequential suppression pattern [KKS05]—with an early suppression of the ψ' followed by χ_c and eventually the J/ψ. Figure 1.10 illustrates the idea of sequential suppression. To futher complicate matters, hadron-hadron collisions [Ant92] have shown that about 60% of the observed J/ψ's are directly produced as $1S$ states, with the remainder coming to about 30% from χ_c

and 10% from ψ' decay ("feed-down"). Proponents of the suppression paradigm claim that the contribution to J/ψ production from feed-down processes must be taken seriously, and that the NA50 results and recent PHENIX data [Per05] may be explained as the manifestation of sequential suppression.

Another dissociation mechanism that can operate besides Debye color screening is parton-induced destruction in the QGP. This mechanism is essentially the dynamic counterpart of static Debye color screening. Originally proposed by E.V. Shuryak in the late 1970s [Shu78], and further elucidated by others [GR01, TSR01], this dissociation mechanism is essentially the QCD analog of photo-dissociation, $g + J/\psi \rightarrow c\bar{c}$. At RHIC energies, the more relevant process is the quasifree inelastic parton scattering, $g(q,\overline{q}) + J/\psi \rightarrow g(q,\overline{q}) + c + \overline{c}$. Although worthy of note and potentially significant, the current theoretical endeavors that use parton-induced dissociation are not sufficiently mature to be experimentally distinguishable from the more established color screening mechanisms. Since both approaches lead to nearly identical results [GR01], we will not concern ourselves with a detailed description of the former here.

1.2.3 J/ψ Regeneration Mechanisms

In their 1986 paper, Matsui and Satz asked themselves:"Could the J/ψ suppression mechanism be compensated in the transition or hadronization stage?" Years later, a number of new theoretical developments took up this question rather seriously. The essential idea of J/ψ production via regeneration in the late stages of the collision was made popular by Peter Braun-Munzinger and collaborators [BS00, BZ], as well as Robert Thews [The]. The idea consisted of primordial charm and anti-charm quarks reaching thermal equilibrium and coming together on a statistical basis to form bound states near or at the phase boundary between hadron matter and the QGP.

The concept of a possible alternative, thermal origin of charmonia was initially introduced [GG99] to explain the measurement of the J/ψ/hadron ratio in nuclear collisions. This theoretical endeavor claimed that J/ψ production was strictly of thermal origin and that it exhibited no direct connection to color deconfinement. Because of their large mass and small production cross section at thermal energies charm quarks are, however, not likely to be thermally produced. On the other hand, significant production of charm quark pairs takes place in the initial, hard-scattering epoch of the collision. This notion led to the idea of statistical hadronization of charm quarks [BS00, BZ]. The treatment of statistical hadronization of charm quarks was achieved in the framework of Braun-Munzinger *et al.*'s successful statistical model [BHS99], which gave a comprehensive description of particle ratios at SPS and later at RHIC (Figure 1.11).

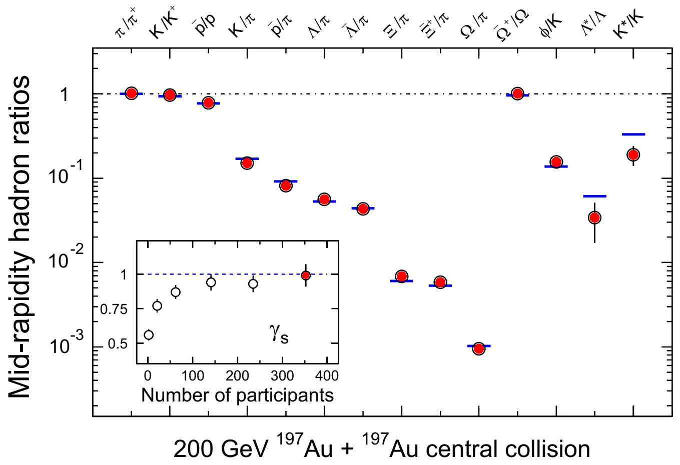

Figure 1.11: Particle ratios observed at RHIC are well described by a statistical model, which served as the basis for a description of J/ψ production via statistical hadronization. Figure taken from [Ada05a].

The efforts of [BS00, BZ] sparked intense activity in the theoretical sector [GR01, GKS02, TSR01]. Some of these models [GR01, GKS02, ABR03] contain regeneration mechanisms that follow the prescription of canonical ensemble thermodynamics, while others [TSR01] are based on a kinetic model. The common denominator between these models is that, for sufficiently high initial parton flux and high parton densities in the QGP, regeneration mechanisms might kick in with force and lead to an enhancement of J/ψ production. Most of the models first treat the dissociation of the charmonium bound state via either static color-screening or dynamic, parton-induced destruction. They then proceed to add regeneration that typically follows a centrality and collision-energy dependence that is opposite to that of dissociation mechanisms. The ensuing competition between regeneration and dissociation is beautifully illustrated by Figure 1.12. At low energies, considerations solely based on dissociation dominate the behavior J/ψ production. Regeneration scenarios then become more relevant with higher collision energies and, at maximal energies, may lead to an enhancement of J/ψ production. The interplay between regeneration and dissociation mechanisms will determine the behavior of J/ψ abundances at a given energy.

One of the theoretical implementations of regeneration via Statistical Hadronization [ABR03] takes the notion of enhancement to another level. In that scenario, there is complete screening of primordially produced J/ψ's, i.e. no initially produced charmonium bound states survive exposure to the hot, dense matter created. According to [ABR03], regeneration mechanisms could lead to an *overwhelming* production of charmonium bound states in the final stages of the collision, leading to extreme enhancement if the charm quark production cross section is large.

The important physics message from all of these models is that an observation of enhancement would not only imply deconfinement, but may also imply

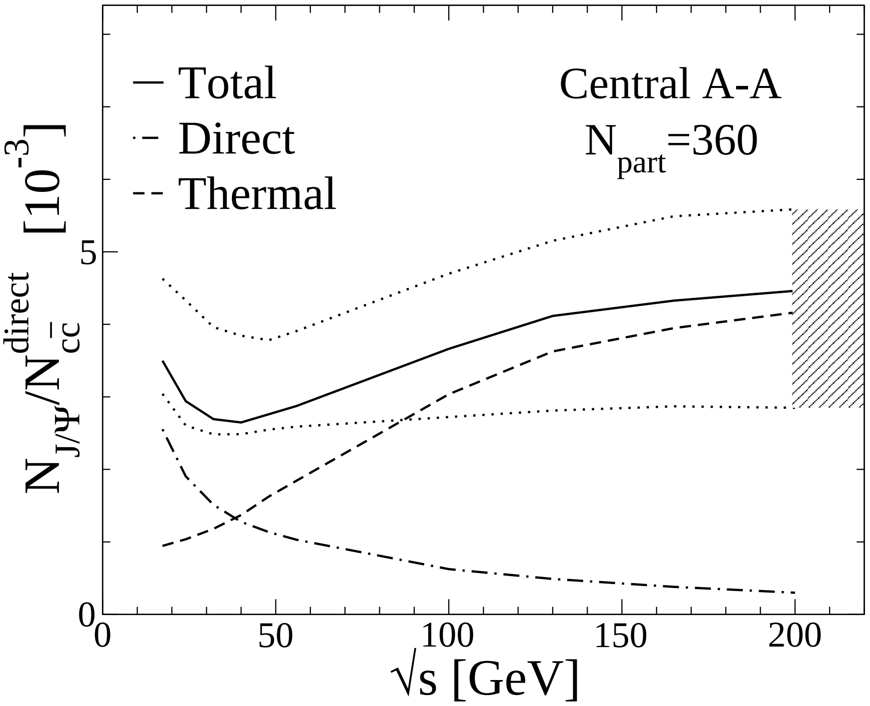

Figure 1.12: Ratio of the number of observed J/ψ's to the number of primordial $c\bar{c}$ pairs (solid curve). The dashed (dash-dotted) curve shows the statistical contribution (direct production with nuclear and QGP suppression) to this ratio. Figure taken from [GR01].

thermalization (in the case where the model assumes thermalization). The latter is a critical requirement for the formation of a QGP as defined in Section 1. It should be noted that observation of J/ψ suppression may not necessarily rule out the possibility for some level of J/ψ production via regeneration. Indeed, recent results from PHENIX [Per05] were interpreted to suggest that suppression scenarios alone cannot describe the data, and that regeneration mechanisms are necessary in order to fully describe it.

It is worth noting that in all of the above discussions, including Lattice QCD calculations, thermal models, and statistical calculations, the partonic source is treated as a static source. Since the hot and dense medium created in high-energy heavy ion collisions is extremely dynamical [Ada05a], those predictions can only be considered as qualitative. Detailed experimental results on both total yields and transverse momentum spectra as a function of collision centrality are necessary for us to understand the underlying dynamics. In the following Section, we will discuss a number of promising observables that can help disentangle the contribution from regeneration and dissociation scenarios.

1.2.4 Experimental Observables

We have described (Section 1.2.2) how the J/ψ will undergo a number of ordinary and exotic dissociation mechanisms that could lead to a suppression of J/ψ production, which can be interpreted as evidence of deconfinement. On the other hand, a number of regeneration (Section 1.2.3) scenarios can become an additional source of J/ψ production in the late stages of the collision. The proponents of some of the regeneration models believe that an observation of enhancement can be a promising signal of deconfinement *and* thermalization, but it is not clear how much the contribution by these mechanisms will be to the total production. Although the notion of regeneration may add some ambiguities to the situation, it has the potential of reinforcing the J/ψ as the "Smoking Gun" of observables in relativistic heavy ion collisions.

As noted earlier, the interplay between regeneration and dissociation mechanisms will determine the behavior of J/ψ abundances in high-energy nuclear collisions. Such an interplay could be mapped out by a systematic variation in collision energies accessible at RHIC. In all models with regeneration mechanisms, the quadratic dependence on initial charm production, coupled with the increase of the charm production cross section with energy as calculated in pQCD, gives rise to a strong dependence of the predicted yields on the collision energy. If such a strong increase is observed at RHIC, it would signal the existence of a production mechanism, i.e. regeneration, nonlinear in initial charm. If no such strong development is observed, then it is likely that the underlying mechanism of J/ψ production will be predominantly due to dissociation mechanisms. For a given collision energy, a similar study, though more statistically demanding, can be carried out by systematically varying the collision centrality.

As noted in Section 1.2.2, it is believed that about 60% of the observed J/ψ's are directly produced as $1S$ states, with the remainder coming to about 30% from χ_c and 10% from ψ' decay. Per recent Lattice QCD calculations, it is possible that J/ψ's survive exposure to energy densities experimentally attainable thus far. The higher excited states, on the other hand, are relatively loosely bound are expected to be completely dissociated even at energy densities achievable at the SPS. The corresponding survival rate, $S_{J/\psi}$, for the J/ψ can then be parametrized as

$$S_{J/\psi} = 0.6 S_\psi + 0.4 S_x \tag{1.6}$$

where S_ψ is the survival rate of directly produced J/ψ's and the second term S_x is for those coming from the decay of the higher excited states χ_c and ψ'. If the above is true, then, according to the authors of Reference [KKS05], the J/ψ suppression seen at RHIC and SPS should follow a similar pattern. As shown in Figure 1.13, it appears that this is fulfilled quite well both in the onset of the suppression and its possible "saturation" in the vicinity of 0.5-0.6. These formulations can be further studied in the future by scrutinizing the corresponding suppression pattern of the ψ', which should follow Equation 1.6.

It should be noted that the various theoretical treatments of J/ψ production,

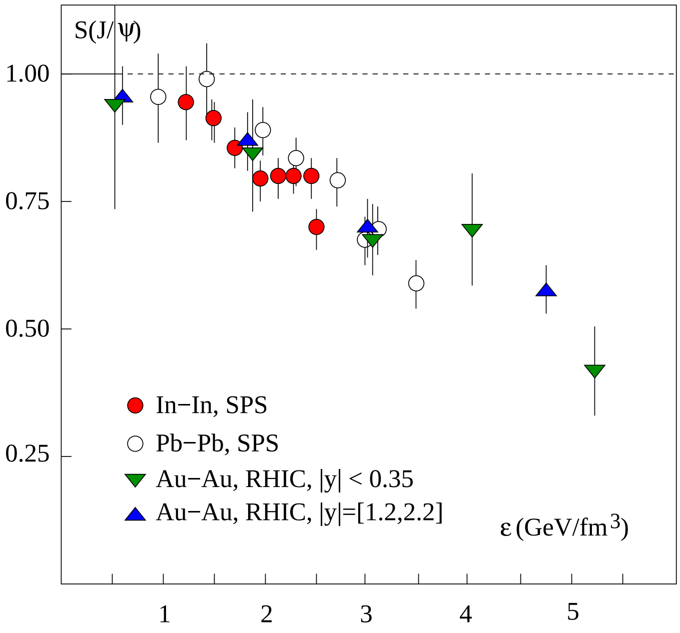

Figure 1.13: J/ψ suppression as a function of energy density from SPS [Ale05, Sha05] and RHIC [Per05] measurements. Figure taken from [KKS05].

whether they be inspired by regeneration or solely by dissociation scenarios, might imply significant changes in the J/ψ transverse momentum (p_T) spectrum. In the context of regeneration scenarios, in which thermalization is often assumed, at the highest RHIC energies one expects essentially thermal p_T shapes (accompanied by a "flow" [PV98] component from the QGP phase), which should be distinguishable from hard production prevalent at the SPS. The effects of regeneration and dissociation mechanisms may leave, however, far more obvious fingerprints in the J/ψ p_T spectrum. Let us consider, for the sake of argument, a situation where there are no novel phenomena taking place in heavy ion collisions and that the underlying physics may be described by a simple superposition of elementary nucleon-nucleon collisions. In this case, barring residual effects brought about by interactions with cold nuclear matter, the J/ψ will follow a p_T shape pre-

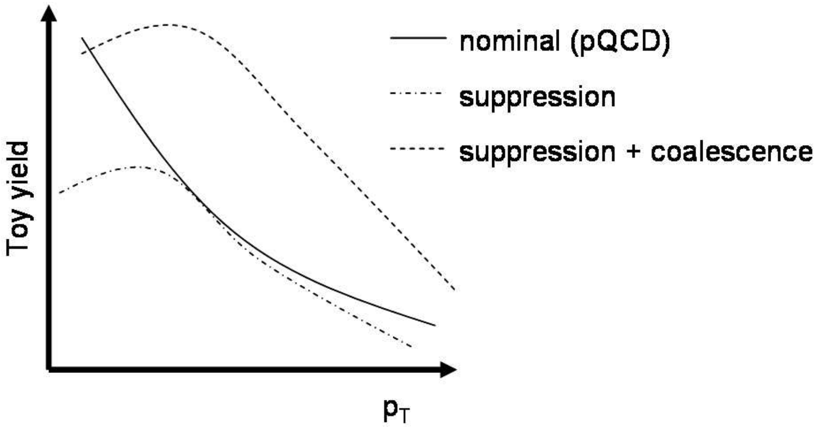

Figure 1.14: A "Toy" J/ψ yield as a function of p_T for various scenarios as explained in the text.

scribed by pQCD (Figure 1.14). Now, if a QGP is created in the collision then the J/ψ will be subjected to dissociation. One can imagine a scenario [ZZX05], in which low-p_T J/ψ's spend more time in the (primarily) longitudinally expanding medium, and are thus more vulnerable to the effects of dissociation. The measured J/ψ p_T spectrum would exhibit a deficit of counts at low p_T which, in addition to demonstrating suppression, would also induce an increase in the $\langle p_T \rangle$ of the distribution. If we were to turn on regeneration mechanisms, then one can imagine that the resulting p_T spectrum would be higher than the nominal pQCD calculation by virtue of enhanced production. Additionally, because the coalescence of a $c\bar{c}$ pair into J/ψ favors the case where the pair has a similar momentum vector, one would see a bump in the corresponding spectrum that would be indicative of a migration of J/ψ's from low p_T to a higher p_T by the aforementioned mechanism.

It has been pointed out in the past that the effect of J/ψ suppression could also manifest itself in the J/ψ transverse momentum squared, $\langle p_T^2 \rangle$ [KNS97]. The

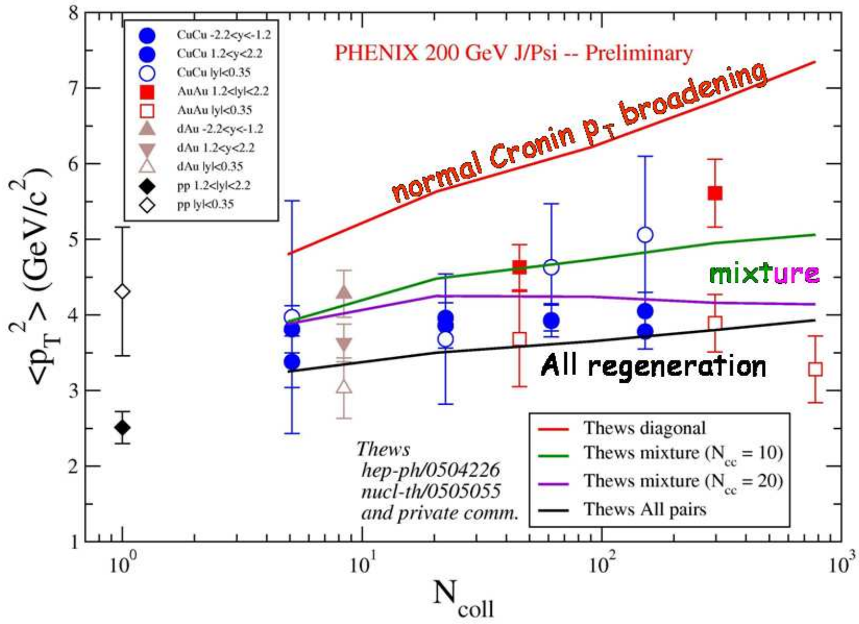

Figure 1.15: J/ψ transverse momentum behavior at RHIC from data [Lei06] and theory (references are indicated in the figure). The statistics are rather lacking at this time to derive anything conclusive.

basic effect of a nuclear medium on the transverse momentum behavior of hard processes is a collision broadening of the participating partons—also known as the "Cronin effect"; here this in turn leads to a broadening of the p_T distribution of the J/ψ's formed by initial hard interactions. In fact, the pattern resulting from dissociation mechanisms [KKS05] stand in contrast to the corresponding predictions from regeneration [The05]. Scrutiny of the J/ψ transverse momentum dynamics, as characterized by $\langle p_T^2 \rangle$, can therefore help to further discriminate between regeneration and dissociation scenarios. Figure 1.15 shows PHENIX preliminary results for the behavior of the J/ψ $\langle p_T^2 \rangle$ in comparison to predictions from a regeneration model. Explicit predictions for the J/ψ rapidity distributions have also been made by both models solely based on dissociation and models that include regeneration, but as in the case of $\langle p_T^2 \rangle$ the statistisc are too scarce at this time to make strong conclusions.

A thorough disentanglement of regeneration and dissociation scenarios will require a complete characterization of the J/ψ as a function of transverse momentum and collision centrality, which will require that further, higher-luminosity runs be carried out at RHIC.

CHAPTER 2

Experimental Apparatus

2.1 The Relativistic Heavy-Ion Collider Complex

The Relativistic Heavy Ion Collider (RHIC) at Brookhaven National Laboratory (BNL) is the first hadron accelerator and collider consisting of two quasi-independent rings. Construction was begun during 1991 and was completed in 1999, for a total cost of $500 million [Oza]. RHIC is the world's newest facility for basic research in relativistic nuclear collisions. It is designed to operate at high collision luminosity over a wide range of beam energies and with particle species ranging from polarized protons to heavy ions. All other nucleus-nucleus collisions to date were performed with an accelerated beam on a fixed target. A colliding beam has many advantages. By having two beams colliding at the center of mass, more energy is provided to the collision rather than the translation of the entire system. Due to RHIC's two quasi-independent rings, it can collide protons on protons ($p+p$). All previous colliding beam experiments at the same or greater energy [Aln86] can only collide protons on anti-protons ($p+\overline{p}$). RHIC can also handle asymmetric collisions, such as protons on gold.

The RHIC accelerator complex (Figure 2.1) is made up of the RHIC rings, the Alternating Gradient Synchrotron (AGS), the Booster Synchrotron, and the Tandem Van de Graaff (TVDG) facility. Gold (Au) atoms are produced in the Pulsed Sputter Ion Source, located in the TVDG facility, where they are ionized

Figure 2.1: Diagram of the AGS - RHIC facility. The heavy ion beam is produced at the Pulsed Sputter Ion Source, accelerated through the Tandem Van de Graaff, booster and AGS, fast extracted at 10.8 GeV/n and injected into RHIC where the beam is accelerated to a top energy of 100 GeV/n and stored. Protons do not proceed through the Tandem Van de Graaff but are accelerated through the LINAC and then to the booster, AGS, and injected into RHIC.

to a charge of -1. These negatively charged Au ions are accelerated to about 1 MeV per nucleon (MeV/n) in the TVDG facility's two 14 million volt electrostatic accelerators, aligned in series, one operating as the primary and the other as the backup. After being accelerated to about 1 MeV/n, the ions are then passed through a thin sheet of gold foil, further ionizing the Au atoms to a net +32 charge. The ions are then taken to the Heavy Ion Transfer Line (HITL), where they travel from the TVDG facility to the Booster Synchrotron. The Booster Synchrotron accelerates the ions to 95 MeV/n, strips them to a net +77 charge, and injects them into the Alternating Gradient Synchrotron (AGS). The AGS accepts the beam of Au ions, increases the energy of the ions to 10.8 GeV/n, and creates ion bunches by focusing the beam both horizontally and vertically. These bunches of Au ions are stripped of their remaining electrons (net +79 charge) and transferred to RHIC via the AGS to RHIC (ATR) transfer line. At the end of this line a switching magnet directs each bunch into either the clockwise (blue) RHIC ring or the counter-clockwise (yellow) ring. Once injected into RHIC, the bunches are accelerated to the desired collision energy and stored for data taking.

2.2 The Design of the STAR Detector

The Solenoidal Tracker At RHIC (STAR) [Har94] is a versatile detector of cylindrical geometry with large acceptance and full azimuthal coverage. STAR was designed primarily for measurements of hadron production over a large solid angle, featuring detector systems for high precision tracking, momentum analysis, and particle identification around the center of mass rapidity equal to zero. The large acceptance of STAR makes it particularly well suited for event-by-event characterizations of heavy ion collisions and for the detection of hadron jets. The layout of the STAR experiment is shown in Figure 2.2. A cutaway side view of the

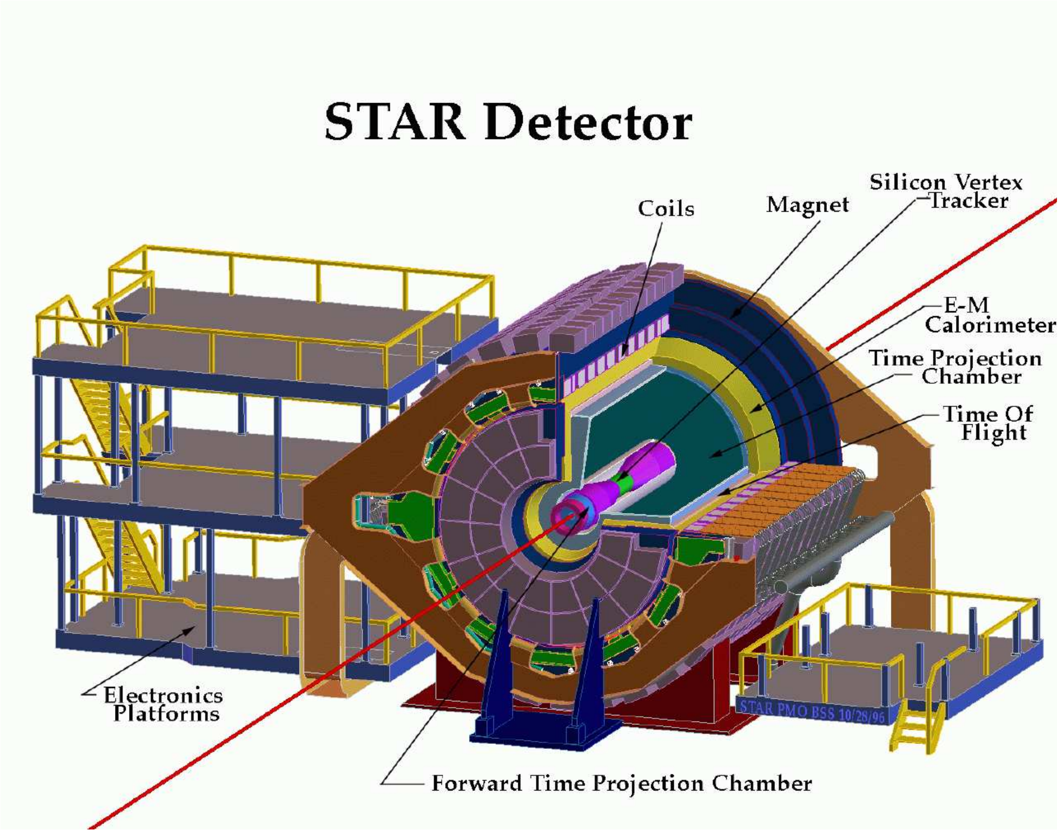

Figure 2.2: Perspective view of the STAR detector, with a cutaway for viewing inner detector systems.

STAR detector as configured for the RHIC 2004 run is displayed in Figure 2.3.

The STAR detector is comprised of several subsystems, each contributing to the functionality and capability of the detector as a whole. The suite of detector elements that constitute the STAR detector sit in a large solenoidal magnet that operates at ±0.25 and ±0.5 Tesla [Ber03]. The main tracking element in STAR is the azimuthally symmetric Time Projection Chamber (TPC) [And03], which provides tracking information for charged particles within $|\eta| < 1.8$ (the kinematic variable, pseudorapidity (η), is defined in Appendix A). Details behind the working principle and functionality of the TPC will be discussed in

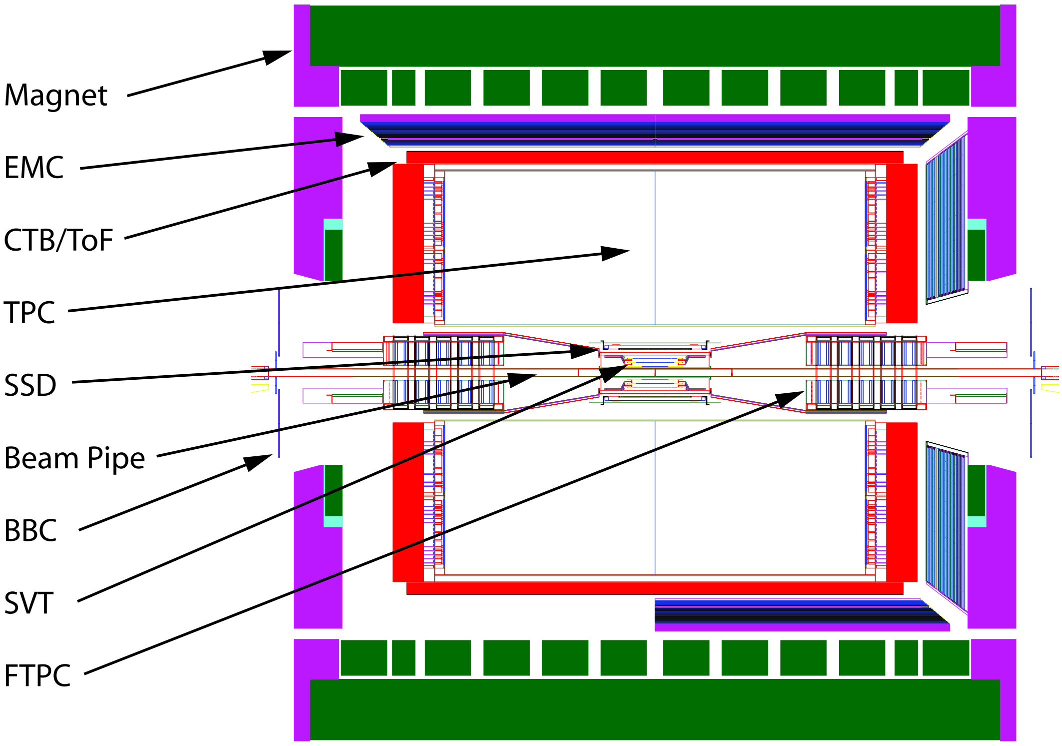

Figure 2.3: Cutaway side view of the STAR detector as configured in 2004.

the following sections. The Forward Time Projection Chamber (FTPC) [Ack03] extends the coverage of the TPC by providing tracking information for charged particles within $2.5 < |\eta| < 4.0$. The Silicon Vertex Tracker (SVT) [Bel03] supplements tracking information provided by the TPC for the precise reconstruction of the decay vertices for particles (resonances) that move from the primary interaction vertex before decaying into charged particles. The Silicon Strip Detector (SSD) [Arn03], which completes the inner tracking layers, provides two dimensional hit position and energy loss measurements for charged particles, improving the extrapolation of TPC tracks through SVT hits. Full coverage of photons and electrons is provided a full-barrel electromagnetic calorimeter (EMC) and the end-cap calorimeter, located on the west portion of STAR [Bed03, All03]. Measurements of the spatial distribution of photons within $2.5 < \eta < 3.5$ is also provided by the Photon Multiplicity Detector (PMD) [Agg03], located behind the west FTPC. There are two Time of Flight (TOF) module prototypes based on multi-gap resistive plate chamber technology [Bon03, Sha02] and scintillation technology [Llo04b] which are located at the five and seven o'clock positions respectively in the east portion of STAR. The lowest level trigger system in STAR is comprised of the Central Trigger Barrel (CTB) [Bie03] and the Zero Degree Calorimeters (ZDCs) [Adl01]. The CTB, which measures event multiplicity, is composed of an array of 240 scintillating slats that surround the TPC in a barrel configuration. The two RHIC-standard ZDCs, located 18 meters upstream and downstream in the beam direction, detect spectator neutrons from the fragmentation of colliding nuclei. Since there is a common design for the ZDCs in all experiments at RHIC, a meaningful comparison of event centrality between all experiments is possible.

For the first year of data taking (2000), the STAR experimental setup consisted of only the TPC, CTB, and ZDCs. As described the previous paragraph, the STAR experimental setup for the year 2004 consisted of a larger array of detector subsystems. A number of detector upgrades are currently being developed to further expand the detection capabilities and physics program of the STAR experiment. Among the future upgrades is the Barrel Time of Flight (TOF) [Llo04a] detector, which will be based on the multi-gap resistive plate chamber technology used by the TOFr prototype module. The TOF detector will provide full azimuthal coverage and two units in pseudorapidity within -1.0 $< \eta <$ 1.0. Combined with existing STAR detectors, the barrel TOF detector will allow STAR to carry out detailed measurement of observables such as correlations and fluctuations, mass and width of resonances, and multi-strange baryon (i.e. Ω) flow. Also under current development is the Heavy Flavor Tracker (HFT) [Wie06], the purpose of which is to extend STAR's capability to measure heavy flavor production, namely of open charm states such as the D meson, by the measurement of displaced vertices. When combined with the TOF upgrade, the proposed HFT detector will also reduce the integrated luminosity needed to measure a statistically robust sample of D^0, D^+ , D_s^+ mesons by approximately an order of magnitude, enabling STAR to make systematic studies of charm thermalization and D^0 meson flow.

2.3 The STAR Time Projection Chamber

The TPC (Figure 2.4) is the primary detector element of the STAR detector. It is a fully pixelized cylindrical drift chamber of 4.2 m in length and 2 m in diameter, with a Multi-Wire Proportional Chamber (MWPC) [BR94] at both of its ends for readout. Its cylindrical geometry affords it an acceptance that covers a range of -1.8 to 1.8 in pseudorapidity through the full azimuthal angle. Information on xy position of tracks is collected by the TPC's 144,000 pads. The TPC has 512

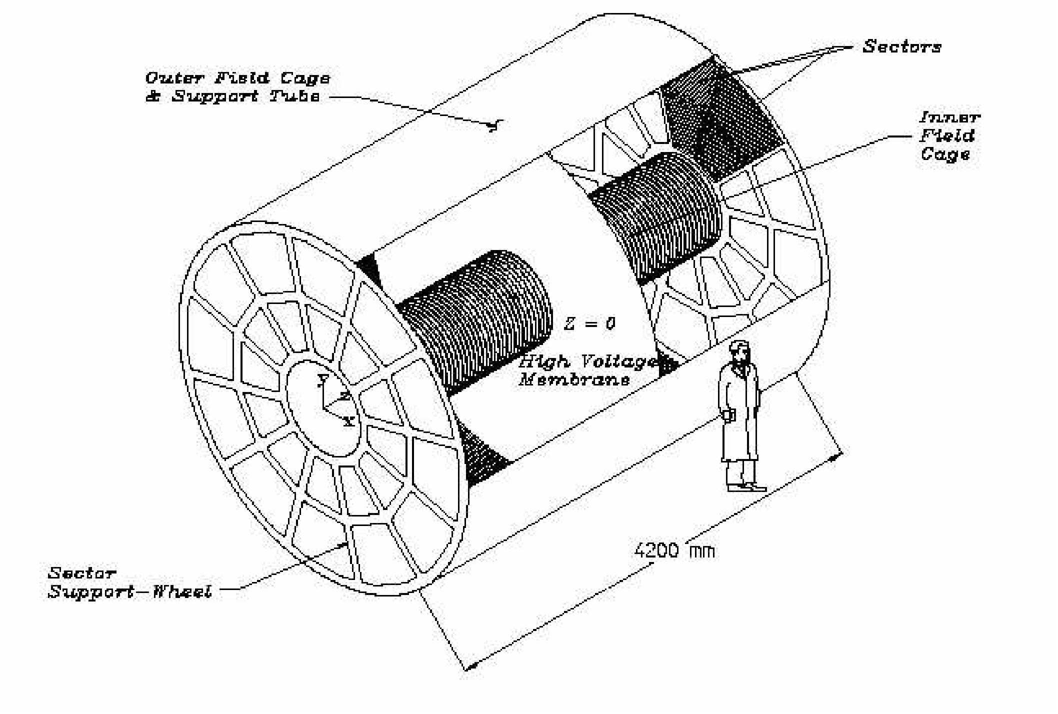

Figure 2.4: The STAR TPC is shown along with major features, among which are inner and outer field cages, the high voltage membrane, and the MWPC sectors.

time buckets which provide z-position information for each hit; hence the "Time Projection" portion of the TPC's name. With over 70 million pixels, the TPC records the ionized tracks that particles leave along their flight path, measures their momenta, and identifies the particles by measuring their ionization energy loss (dE/dx). The TPC is capable of measuring the momenta of charged particles over a range from 100 MeV/c to 30 GeV/c and can identify them (protons, pions, kaons, etc.) over a momentum range from 100 MeV/c to over 1 GeV/c.

The TPC's volume between the inner and outer field cages is filled with P10 gas—comprised of 90% argon and 10% methane—that is regulated at 2 mbar above atmospheric pressure [Koc03]. When a charged particle traverses the gas-filled volume of the TPC, it undergoes inelastic collisions with the gas atoms, leaving behind a trail of ionization along its path. The electrons clusters that are part of the trails are then, under the influence of an externally applied electric field, swept toward the ends of the TPC where their location and drift time is measured. The primary attribute of the P10 gas, through which the electron trails drift, and has long been used in TPCs, is fast drift velocity requiring an electric field of only $\approx$ 135 V/cm. The electric field is provided by the outer field cage (OFC), the inner field cage (IFC), the high voltage central membrane (CM) and the read out end caps (Figure 2.4). In addition to providing a containment volume for the P10 gas, the IFC and OFC insure that the electric field uniformity is high, which is of critical importance since track reconstruction precision is sub–milimeter and electron drift paths are up to 2 meters. The anode and pad planes, located at each end of the TPC, are organized into sectors. The end caps as a whole are held at ground. The CM cathode is located at the center of the TPC and is held at high voltage (-28 kV for the 2004 running year).

2.3.1 The Central Membrane

The CM is constructed from a number of pie-shaped, carbon-loaded kapton film sections, each of which is 70 μm thick. An outer support hoop, which is mounted in the OFC, keeps the CM secured under tension. There is no mechanical coupling to the IFC other than a single electrical connection. This design minimizes material and maintains a good flat surface to within 0.5 mm. Thirty six aluminum stripes are attached to each side of the CM to provide a low work function material as the target for the TPC laser calibration system [Leb02, Abe03]. When ultraviolet photons hit the stripes, electrons are photo-ejected. Since the position of the narrow stripes are precisely measured, the ejected electrons can be used for spatial calibration.

2.3.2 The Field Cages and TPC Outer Shell

The inner and outer field cages have a mechanical design that minimizes construction mass. Minimization of mass is important in reducing background from secondary particle production and track distortions due to multiple coulomb scattering. As the particles make their way from the collision vertex, through the IFC, and eventually to the active detector region of the TPC, the corruption of their kinematic information is kept to a minimum. The light weight, self-supporting cylinders have walls that are effectively a bonded sandwich of two metal layers separated by Nomex honeycomb. Punch through pins were used to electrically connect the layers on the two sides of the sandwich. A cutaway view of the IFC is shown in Figure 2.5. The metal layer, which is actually comprised of kapton with metal on both sides, is etched to form electrically separated 10 mm stripes separated by 1.5 mm. The metal layer is etched into stripes so that, after rolling the whole assembly into a cylinder, the stripes become rings around the cylinder.

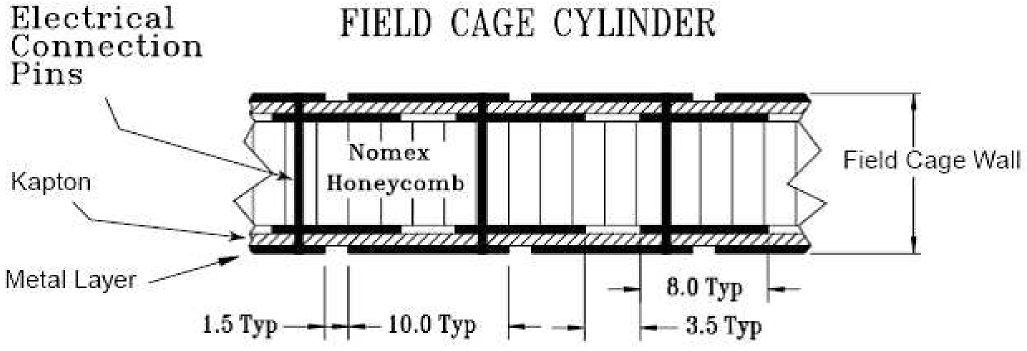

Figure 2.5: A cutaway view of the IFC showing the construction and composition of the cylinder wall. Dimensions are in mm.

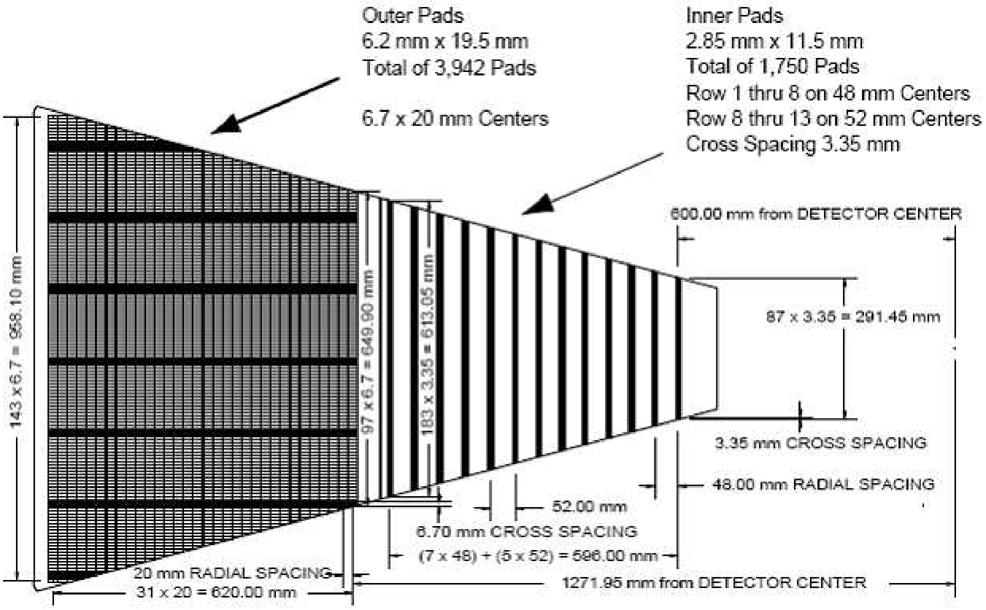

Figure 2.6: Full sector pad plane. The inner sub-sector is shown on the right and the outer sub-sector, with a higher density of pads, is shown on the left.

The sandwich structure of the OFC cylinder wall is 10 mm thick while the IFC has a wall thickness of 12.9 mm. Although thicker than the OFC, the IFC's metal structure is composed of aluminum, which limits the amount of distortion suffered by the particles traversing its thickness. Copper was used for the OFC in order to simplify construction and electrical connectivity, and consequently the OFC significantly adds more distortions to the particles that pass throught it. The OFC's contribution to the distortions of a particle's trajectory are of little concern to the analysis in this dissertation; particles that reach the OFC would have already traversed the active detector volume of the TPC, which is the only detector subsystem used in this analysis.

The outermost component of the TPC in the radial direction is a structure comprised of two aluminum skins separated by an aluminum honeycomb. The structure is separated from the OFC by 5.7 cm of nitrogen gas insulator. The skins are in fact multi-layer wraps of aluminum and the inner most layer, which faces the OFC, is electrically isolated from the rest of the assembly. The inner most layer can be used to monitor any possible corona discharge across the gas insulator. Aluminum support rails are bonded to the outer portion of the assembly in order to carry the CTB trays. The support rails have a central water channel that holds the temperature of the structure at a fixed point, which then acts as a heat sink for the TPC electronics and other STAR detector subsystems.

2.3.3 The TPC End-caps

The STAR end cap readout planes are similar in design to the ones found in TPCs of other experiments such as NA49 and ALEPH. In addition to some refinements to accommodate the high track density at RHIC, some other minor modifications were made to the design of the STAR end cap readout planes to improve reliability and simplify construction. The TPC readout planes, comprised of MWPC chambers with pad readout, are modular units mounted on aluminum support wheels. The readout modules (sectors) are arranged in a circular configuration with 12 sectors around the circle. Each sector is divided into two sub-sectors: an inner radius sector and an outer radius sector (Figure 2.6). The construction and maintenance of the sectors is greatly simplified by their modular nature and their manageable size. As illustrated in Figure 2.7, the MWPC chambers are comprised of four elements, a pad plane and three wire planes. The anode wire plane, with wires of 20 μm in thickness, along with the pad plane on one side and the ground wire plane on the other, comprise the amplification layer. The anode wires are biased to a high voltage to provide the necessary electric field to avalanche the electrons from the track ionization.

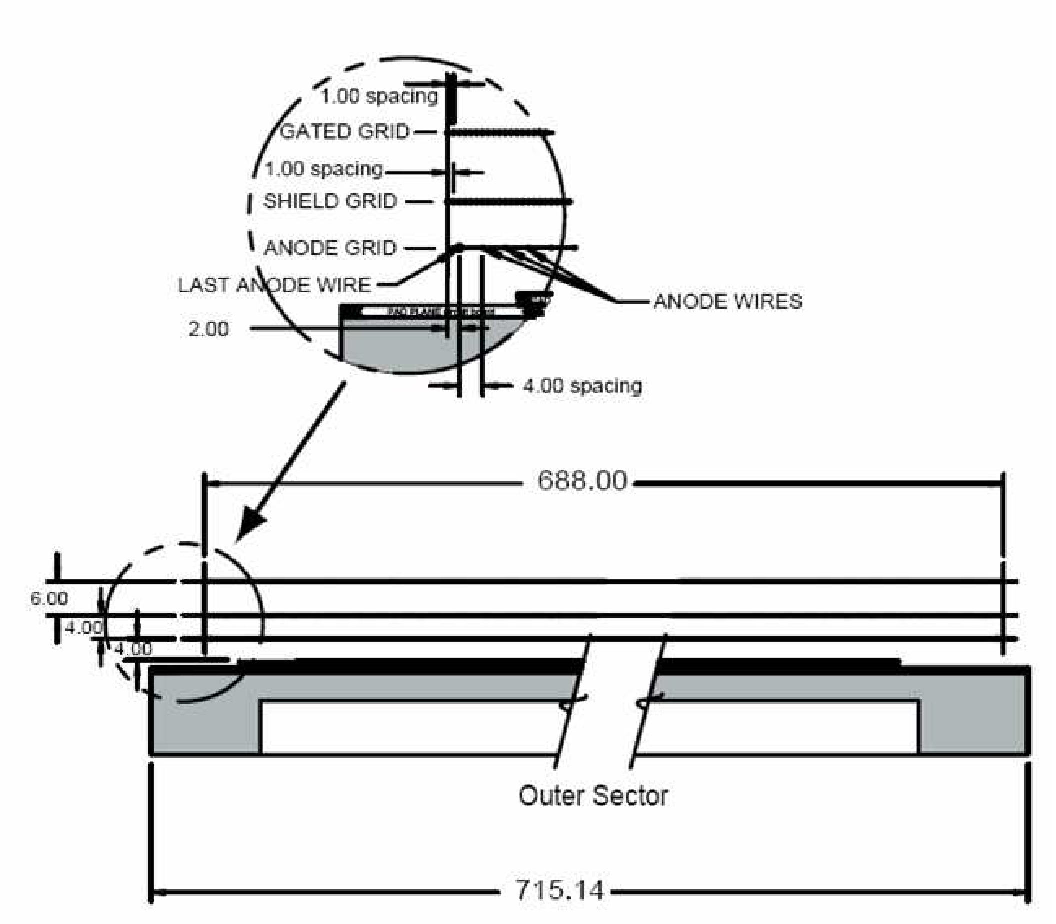

Figure 2.7: Outer sub-sector wire geometry. The inner sub-sector pad plane has the same layout except the spacing around the anode plane is 2 mm instead of the 4 mm shown here.

The gating grid is the third wire plane and its purpose is to establish the boundary conditions defining the electric field in the TPC drift volume at the ends of the TPC. The gating grid also functions as a gate to control the passage of electrons from the active volume of the TPC into the MWPC. The gating grid allows drift electrons to pass through to the MWPC only while an event is being recorded; otherwise, it is electrostatically opaque to electrons. More importantly, it also prevents ions produced in the MWPC from entering the active TPC volume. The drift velocity of ions is much slower than electrons, so they are too slow to move into the active TPC volume while the gating grid is "open". Furthermore, ions produced in the MWPC are drifted to cathode and gating grid electrodes while the gating grid is "closed".

2.3.4 TPC Hit, Track, and Vertex Finding

The TPC reconstruction process begins by creating three dimensional space points from the TPC pixel data. A TPC pixel consists of several pieces of information: pad number, time bucket, and ADC value. The first step in the reconstruction process is then to find groups of pixels which are close together in both position-space and time. This is referred to as TPC cluster finding. This proceeds by the following algorithm: *I*) Identify a pixel with ADC value above a certain threshold; *II*) Search for pixels in adjoining pads and time buckets; *III*) Collect these pixels as being from a common cluster and mark them as used; *IV*) Repeat until no unused pixels remain with ADC value above threshold. Additionally, corrections for bad pads and relative timing are applied during the cluster finding stage. Figure 2.8 illustrates a scenario where two clusters are identified [Lis96]. The next step is to turn clusters into 3D space points called TPC hits. Each cluster is analyzed and a search for one or more maxima within the

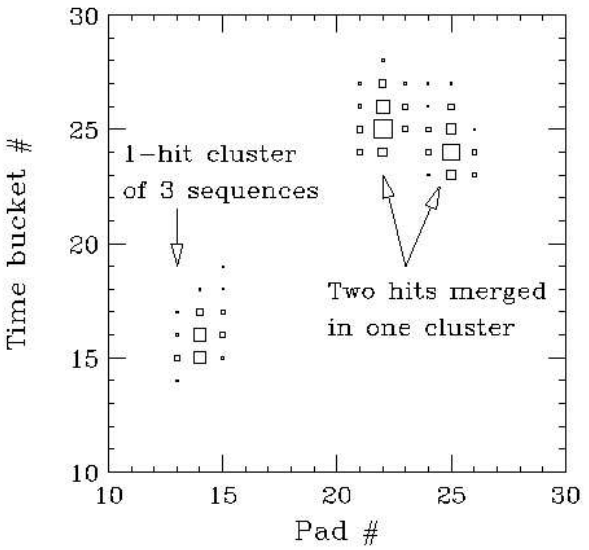

Figure 2.8: An example of single and two hit clusters.

cluster is performed. Clusters that consist of merged hits, which are recognized by studying the cluster width in both pad and time dimensions, are split according to a deconvolution algorithm into two sub-clusters. Once one or more maxima are found, the mean time and space values are characterized by an independent three point Gaussian fit in both the space and time dimensions. The final step of hit finding is to transform from local coordinates (comprised of sector, padrow, pad, time bin) to global 3D Cartesian coordinates. The transverse coordinates x and y are determined by simply mapping the sector, padrow, and pad values into cartesian coordinates. The distance of the hit along the beam direction, z, is determined by mapping the value of the time bucket to a corresponding z-coordinate value. This mapping depends on the drift velocity of an electron in the TPC gas as well as the time offset between the trigger start time and the beginning of the TPC readout. The drift velocity of electrons, which can vary according to a number of factors, in the TPC is closely monitored periodically over several data-taking runs [Leb02].

After TPC hit finding yields a collection of points reported in global cartesian coordinates, pattern recognition algorithms are applied in order to identify hits coming from the same charged particle (track). This is achieved by the STAR TPC tracking algorithm (TPT) [MS94], which identifies points that lie close in space, constructs segments from these points, then successfully merges neighboring segments. Once the hits belonging to a particular track are identified, the TPT package then fits the collection of points to a track model. The track model implemented in STAR is based on the fact that a charged particle traveling through a constant magnetic field along the beam direction follows a helical equation of motion. With a well defined track model one can then make precise extrapolations of a particle's trajectory into non-instrumented regions, e.g., inside the beam pipe.

The results of the TPT helix fit are stored for each track in a container which is used as the basis for the rest of the event reconstruction. A global refit of each track is then performed. The goal of the refit is to correct for momentum reconstruction biases caused by multiple scattering and energy loss in the TPC gas, weight each space point by its relative measurement uncertainty, and discard points from the fit that lie far from the best fit (outliers). These criteria are realized by the application of a Kalman filter routine. The Kalman filter makes a complete and robust statistical treatment by using information about the particle trajectory, the space points and their errors, as well as the material that the particle has traversed. Further details of this procedure can be found in Reference [Bos97].

Reconstruction proceeds to the primary vertex finding stage after the global refit is achieved. The exact algorithm that is used to find the primary vertex—the position of the primary beam-beam interaction—depends on the colliding beam species and the number of global tracks in the event. In Au+Au collisions, the default Event Vertex Reconstruction (EVR) [MC92] algorithm is used for events that have more than 30 tracks. Below that, the Low Multiplicity Vertex (LMV) finding algorithm is used. In a Au+Au event, the resolution of the primary vertex position is about 100-200 μm. This is much better than the typical TPC hit resolution of about 700 μm. The inclusion of the primary vertex results in track finding can therefore bring about a substantial improvement to the transverse momentum resolution. After the primary vertex is found, each track is tested to determine if it originated from the primary vertex. A track is deemed a primary track if its three dimensional distance of closest approach (DCA) to the primary vertex is less than 3 cm. These tracks are then subjected to a primary refit carried out by a constrained Kalman fit that forces the track to originate from the primary vertex location. In addition, the refit takes into accout the momentum bias due to energy loss as well as multiple scattering of the particle in the material between the interaction point and the first padrow of the TPC. Accounting for these effects is of particular importance for primary tracks because the momentum of the track is reported at the location of the primary vertex. Since J/ψ mesons have a mean lifetime of 0.8×10^{-20} seconds, they essentially decay right on top of the primary vertex; therefore, primary tracks are used in this analysis in order to reconstruct the decay of J/ψ mesons.

CHAPTER 3

Analysis Methods

3.1 Trigger

The typical luminosity—number of particle collisions per second—that is achievable at RHIC is much higher than the event sampling rate of slow tracking detectors, such as the STAR TPC. The slow STAR detector subsystems only operate at rates of about 100 Hz. Collision interaction rates approach the RHIC crossing rates (up to ∼10 MHz) [Bie03] for the highest luminosity beams, so fast detectors, such as the CTB, must provide means to reduce the rate by almost 5 orders of magnitude. Interactions are selected based on the distributions of particles and energy obtained from the fast trigger detectors.

Of interest to this analysis is the minimum bias trigger configuration, the goal of which is to maximize acceptance of inelastic Au+Au interactions at all impact parameters. The trigger conditions were defined in real-time data-taking by a logical combination of information from the fast trigger detectors. The trigger detectors in the 2004 run consisted of the east and west ZDCs and the CTB. Minimum-bias triggered events are defined as ones in which the two ZDCs are above threshold (ADC > 5) and the sum of all CTB slats have ADC > 75. The CTB portion of the minimum bias trigger condition was imposed in order to reject non-hadronic events.

For the 2004 Au+Au run, additional timing information from the ZDC was available. Using the independent timing information from the east and west ZDCs, one can locate the approximate position of the collision along the beam direction [Gon01]. This allowed for selection of events that satisfied a vertex position along the beam direction of less than 30 cm from the center of the TPC. Selecting events that occur near $z = 0$ cm allows for the same acceptance on the left and right portions of the STAR detector. Maximizing acceptance ensures that most of the detector volume of STAR subsystems, such as TPC, is used.

3.2 Event Selection

Here, we address the general characteristics of the selected events used in this analysis. Our analysis was restricted to events with a primary vertex within 30 cm of the center of the TPC along the beam direction. Figure 3.1 shows the z position distribution of primary vertices. As discussed in the previous section, an online vertex selection was applied using ZDC time information. For the selected minimum bias trigger configuration, 90% of all events lie within the offline vertex cut of 30 cm. In addition to maximizing the available acceptance for selected tracks, excluding events with a longitudinal vertex position outside 30 cm of the TPC's center avoids any centrality biases associated with the ZDC-based online vertex cut.

In Figure 3.2, we show the uncorrected primary charged particle multiplicity, N_{ch}, in the region of $|\eta| < 0.5$. This is also known as the reference multiplicity. The full range of charged particle multiplicity, $N_{ch} \geq 14$, shown in Figure 3.2 corresponds to 80% of the geometric cross section in Au+Au collisions. This range of multiplicity was further divided into 3 bins: $14 \leq N_{ch} < 150$, $150 \leq N_{ch} < 319$, and $N_{ch} \geq 319$ which respectively correspond to the 40-80%, 20-40%, and the top 0-20% of the geometric cross section. Table 3.1 summarizes the centrality

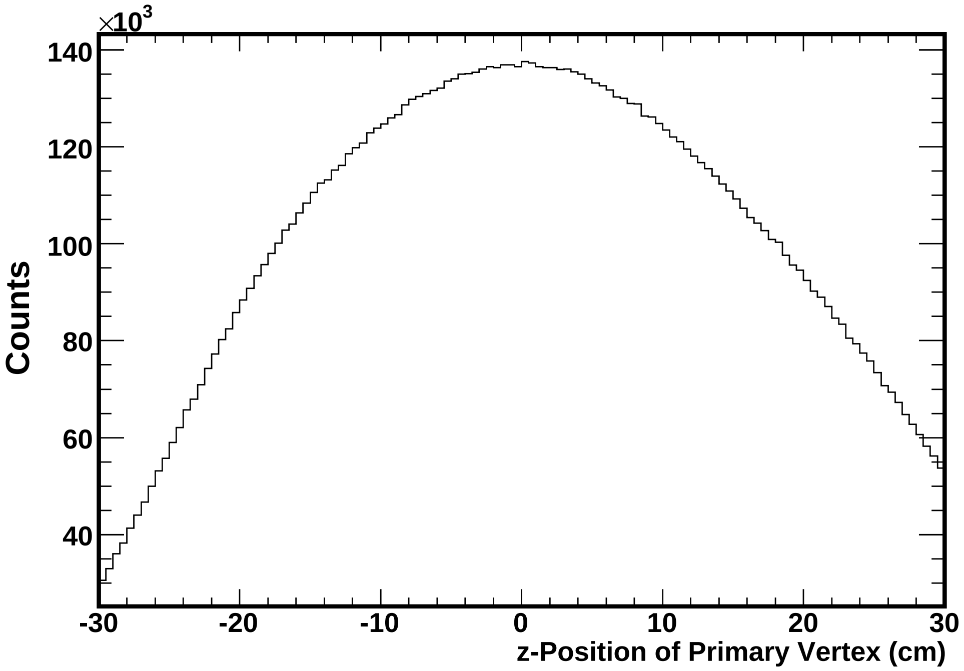

Figure 3.1: The position of the primary vertex in the beam direction for the 2004 Au+Au run.

classes and associated cuts.

Part of the minbias trigger setup consisted of a CTB selection that suppressed non-hadronic events, as previously discussed (Section 3.1). The CTB portion of the minbias trigger rejects 7±2% of low-multiplicity events with vertices; therefore, we decided to exclude events of 80-100% in centrality.

As stated in Section 2.2, the STAR detector is embedded in a magnetic field that is capable of operating at ±0.25 (half-field) and ±0.5 (full-field) Tesla. In this analysis, we only make use of events where the STAR magnet was operating at full field. The reason for this choice is due to the exceedingly high luminosity conditions in the 2004 run, which induced substantial distortions to the recon-

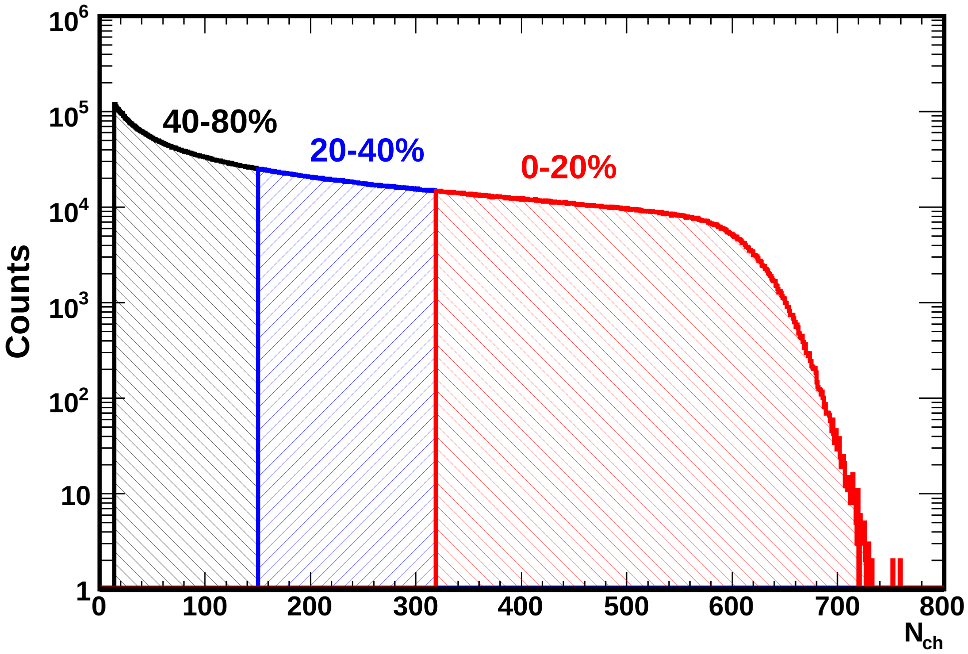

Figure 3.2: The minimum bias primary track charged multiplicity distribution, N_{ch}, in the pseudorapidity region of $|\eta| < 0.5$. The three centrality classes used in this analysis are shown.

struction of charged tracks [Tho]. During the time this analysis was carried out, these distortions, which were rectified in full-field events, had not yet been taken into account in half-field events.

The combination of all event-level cuts yielded a sample of 12×10^6 minimum bias, full-field events.

3.3 Electron Identification

J/ψ mesons have a 5.88% chance of decaying via the dimuon channel, 5.93% via the dielectron channel, and the rest of the time via decays that involve hadronic

centrality	% of most central collisions	reference multiplicity
1	$40 - 80$	$14 - 150$
2	$20 - 40$	$150 - 319$
3	$0 - 20$	$319 - \infty$
minimum bias	$0 - 80$	$14 - \infty$

Table 3.1: The centrality bin, reference multiplicity cut, and corresponding fractional geometric cross sections are listed.

resonances [Eid04]. As will become evident later in this chapter, muons measured by the STAR TPC are difficult to distinguish from charged pions because both types of particles are similar in mass. The J/ψ can decay via a plethora of hadronic decays, but each of them only shares a miniscule fraction of the J/ψ's decay probability. Unlike muons, electrons can be separated to a large extent from the other stable charged particles (e.g. protons, kaons, pions) measured by the TPC; this, in conjunction with the relatively high branching ratio, makes the dielectron channel the only viable way of reconstructing J/ψ mesons in STAR.

This analysis depends mainly on charged track information from the TPC. Since the lifetime of the J/ψ's is such that they decay very close to the primary collision vertex, we are interested in primary charged tracks, as defined in Section 2.3.4. In a given event, a sample of primary tracks is collected from the total track pool by subjecting each track to a series of quality checks. The first of these checks ensures that the results from the track fitting and Kalman filtering procedures yielded good results. Tracks with a flag—the attribute associated with quality of the track fit—value greater than zero, i.e. good tracks, are selected. Only long tracks, ones with at least 25 hit points, were selected. Figure 3.3 shows the hit point distribution for primary tracks in minimum bias events. The selection of tracks with a high number of hit points is motivated by the fact that they will have better momentum resolution than short tracks.

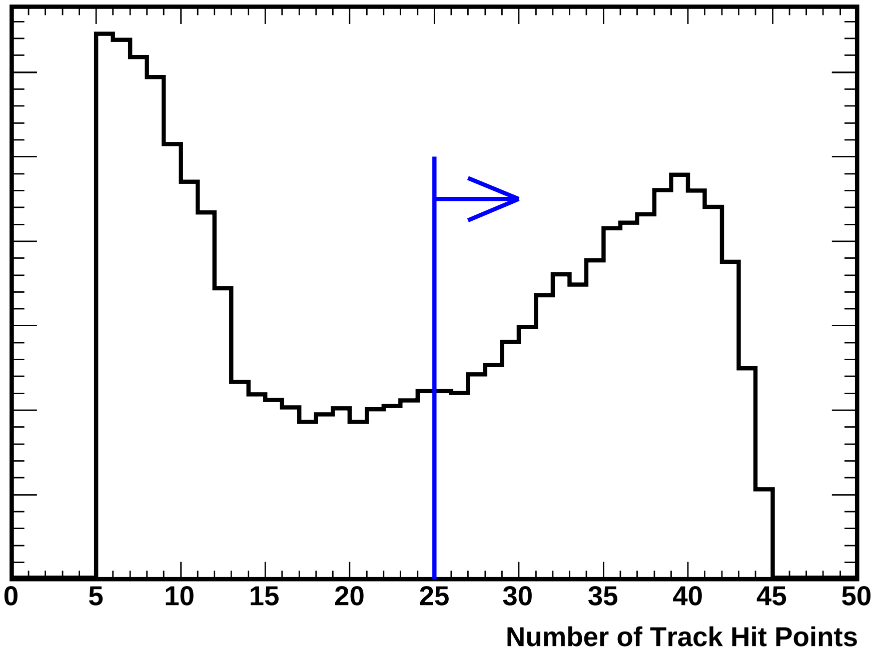

Figure 3.3: The hit point distribution of primary tracks.

Primary tracks were also required to have a projected (Global) distance of closest approach (DCA) to the event primary vertex of less than 2 cm. Tracks with a DCA > 2 cm are a treated as background. The DCA distribution of primary tracks is shown in Figure 3.4. J/ψ decay electrons should, in principle, originate directly from the primary vertex, and would thus have DCA$\sim$0 cm. However, because of the TPC's limited momentum resolution, tracks will only approach this theoretical limit by one or two centimeters.

Because of their low mass, electrons that originate from J/ψ decays typically

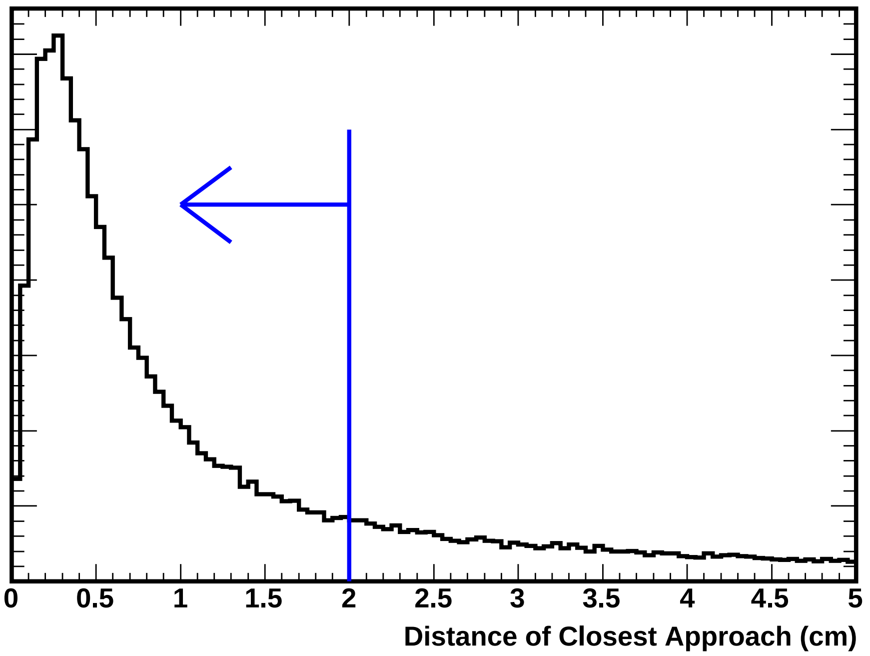

Figure 3.4: The distance of closest approach to the primary vertex. Only tracks with a DCA of less than 2 cm are selected.

have a high momentum. Selecting charged tracks with $p > 500$ MeV reduces the combinatorial background while retaining 99% of electron pairs from J/ψ decays. Charged tracks within a window of $|\eta| < 1.0$ were selected. Beyond $|\eta| = 1.0$, the TPC's reconstruction efficiency drops off sharply and, more importantly, tracks with $|\eta| > 1.0$ do not have many hit points, and are therefore of lesser quality.

Particles that traverse the TPC gas leave a trail of ionization in their wake. The energy loss (dE/dx) suffered by the charged particles as they ionize the TPC gas can be measured. Using the dE/dx information from the TPC one can infer the identity of particles on a statistical basis [Las97]. Figure 3.5 shows the dE/dx distribution of charged tracks measured in the TPC as a function of momentum. Superimposed in Figure 3.5 are Bichsel Functions [Bic02] that describe the momentum dependence of the average ionization energy loss of all particle species. The proton, kaon, and pion bands can be cleanly separated over a kinematic range of approximately 0.2-1.0 GeV/c. The electron band, however, is traversed by all the other bands over the same kinematic range.

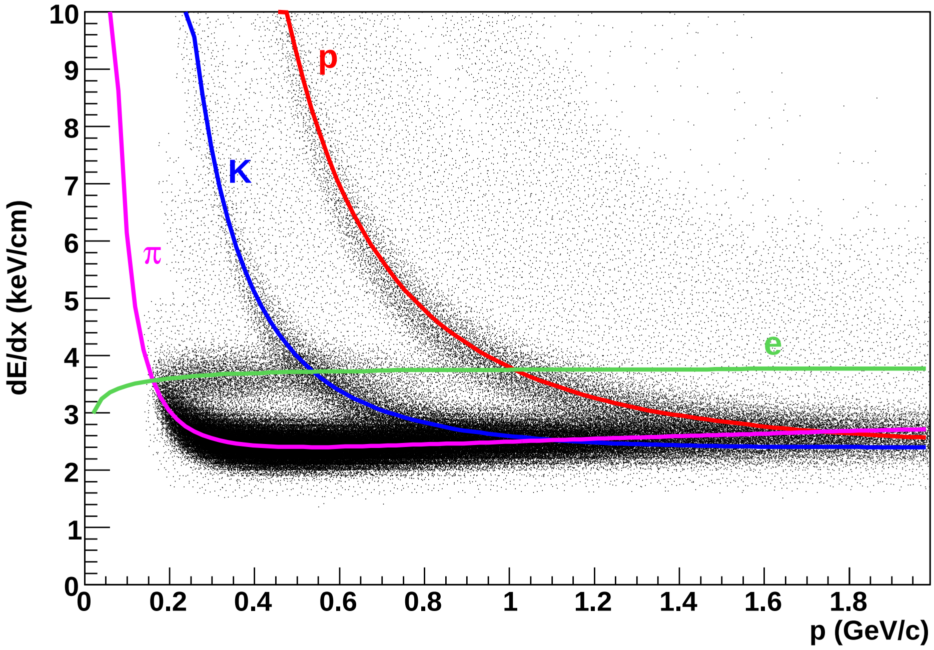

Figure 3.5: The energy loss of positively charged tracks as a function of track momentum. Bichsel functions for protons (p), kaons (K), pions (π), and electrons (e) are also shown. The muon Bichsel function is not shown, but, with the exception of the range of $p < 200$ MeV, muons follow almost the same pattern as pions.

All charged tracks within two standard deviations (2σ) from the mean energy loss of electrons at a given momentum were selected. Furthermore, charged tracks that fall within 2σ of the proton and kaon bands, and $-3.5 < \sigma < 2.5$ of the pion band were not selected. This selection of tracks is motivated by the fact that we are only interested in reconstructing J/ψ's from electron decays; furthermore, exclusion of the hadron bands reduces the combinatorial background in this analysis as well as the computational resources. Figure 3.6 shows the dE/dx distribution of all charged tracks as well as selected ones.

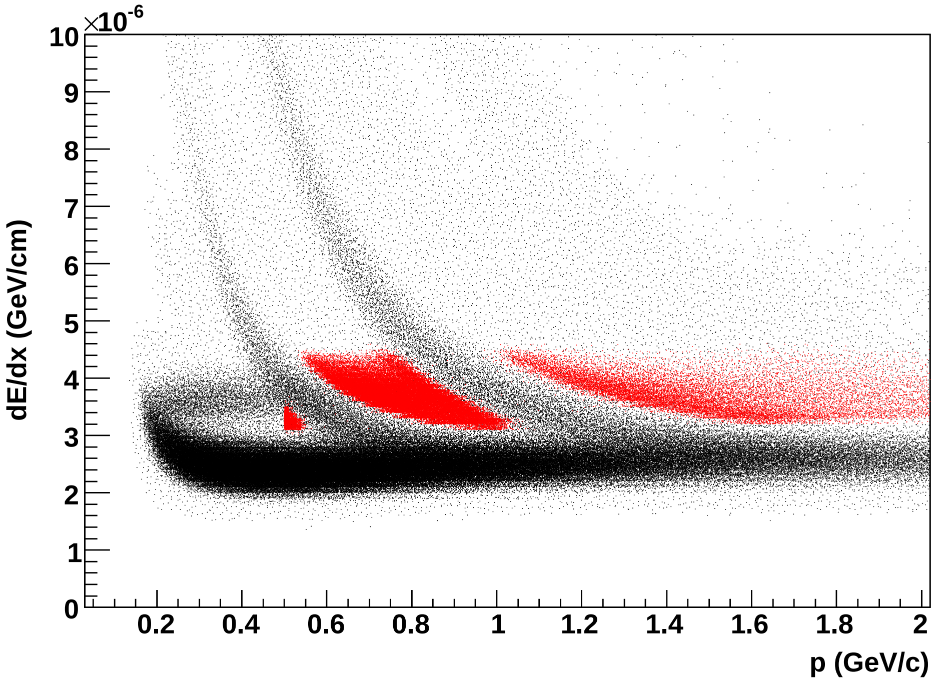

Figure 3.6: The energy loss of positively charged tracks as a function of track momentum. The red distribution indicates the selected tracks.

A number of factors limit the TPC's dE/dx resolution, namely ionization fluctuations and finite track length. Also, there is an effective cross talk across the end cap's padrows that causes a small reduction in the dE/dx resolution. While there is little we can do about the ionization fluctuations and padrow distortions, we can require that charged tracks be a of a minimum length. In our analysis, this is achieved by requiring that all tracks have more than 20 dE/dx hit points. The improved dE/dx resolution brought about by a cut on the number of dE/dx hit points improves the effectiveness of our particle selection criteria because fewer hadrons leak into the electron band. A summary of all kinematic and track quality cuts is shown in Table 3.2.

Cut name	Cut value/range	Comment
flag	> 0	good track fit
nHits	> 25	long tracks, good p resolution
nHitsDedx	> 20	good dE/dx resolution
DCA	< 2 cm	reduce background
p	> 500 MeV	reduce background
η	< 1.0	maximize TPC coverage
$\|n\sigma_e\|$	< 2.0	select electrons
$\|n\sigma_p\|$	> 2.0	reject protons
$\|n\sigma_k\|$	> 2.0	reject kaons
$n\sigma_\pi$	> 2.5, $<$ -3.5	reject pions

Table 3.2: Summary of kinematic and track quality cuts used in this analysis.

3.4 J/ψ Reconstruction and the Event Mixing Technique

After the acquisition of a sample of electron candidates of good quality and a relatively low hadron contamination, as described in the previous section, we can proceed to reconstruct J/ψ mesons by scrutinizing electron-positron pairs. Ideally, if the TPC's momentum resolution capabilities were such that we could identify and separate the J/ψ decay vertex from the primary collision vertex, J/ψ reconstruction would be carried out via the topological technique [Lon02]. Unlike a particle such as the Λ [Lon02, Jia05], where the application of the topological technique is feasible, the J/ψ decay lifetime ($\sim$1$\times$10^{-20} s) and the TPC primary vertex reconstruction resolution are such that the J/ψ decay vertex cannot be distinguished from the primary collision vertex.

The only viable way of reconstructing the J/ψ in STAR is by pairing all selected positively charged tracks with negatively charged ones and calculating kinematic quantities, e.g. invariant mass, for all possible permutations. In this technique, there is no way to distinguish an electron-positron pair from a J/ψ decay from random combinations of electron and positron candidates produced in the collisions and accepted into the TPC. As a result, the J/ψ signal in the dielectron invariant mass spectrum will sit atop a large combinatorial background. The proper description—and subsequent subtraction—of this large background is therefore of critical importance to this analysis. Here, we resort to the use of the event mixing technique in order to describe the background. Originally concieved by Kopylov [Kop74], the event mixing technique was later refined by L'Hote [LH94] and others [DFN84]. The event mixing technique is widely used in analyses such as this one, where the available statistics are low.

The following is a basic description of the event mixing technique. Let's assume that we have an event in which the momenta of all charged tracks are completely uncorrelated. A sample of pairs from the combination of charged tracks in such event will yield an invariant mass distribution whose shape arises from the random sampling of the acceptance and efficiency-modified momentum space distribution of the pair partners. Now, let's further assume that from the sample of pairs described above, a second, mixed-event sample of pairs is formed, in which a pair partner is taken from one event and the other pair partner is taken from a different event. For similar reasons, the shape of the mixed-event invariant mass distribution will be the same as that of the original, same-event distribution. In a real event, the pair partners, such as those emmanating from a J/ψ, will actually be correlated. The same-event distribution from a real event will therefore contain a subset of pair partners whose momenta are indeed correlated. The mixed-event distribution destroys this correlation while maintaining the general shape exhibited by the same-event distribution, i.e. the background shape. In essence, everything of significance to the correlation analysis is contained in the mixed-event distribution except for the correlation itself. A diagram of the event mixing paradigm is shown in Figure 3.7.

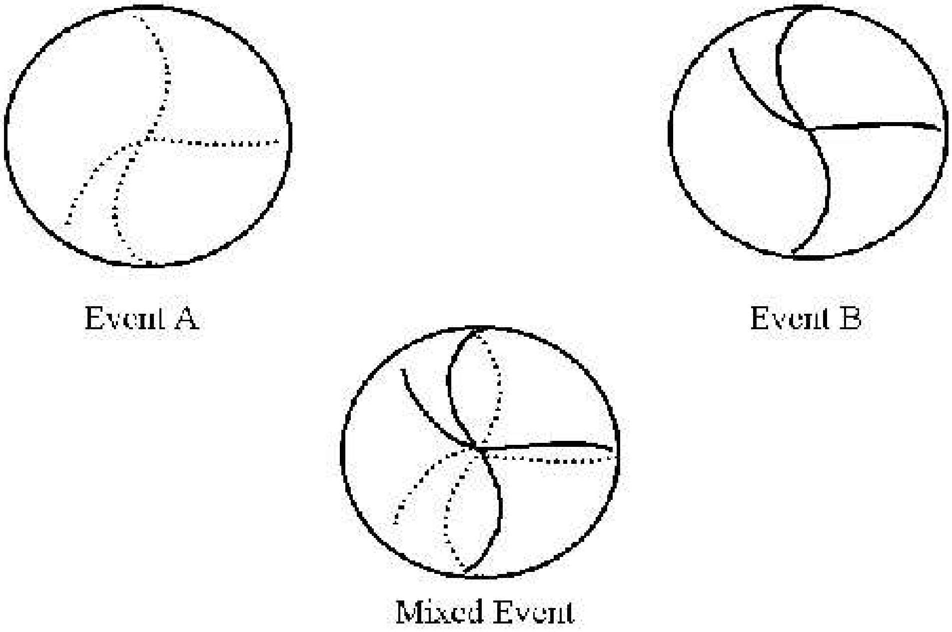

Figure 3.7: A diagram of the event mixing technique is shown. Negative tracks from event A are mixed with positive tracks from event B, from these a mixed event is produced. All possible permutations of positive and negative tracks are considered in the mixed event. Figure is taken from Reference [Yam01].

In this analysis, each event was mixed with fifty other events in order to improve the statistics of the background. The mixing of events was carried out by implementing a First-In-First-Out (FIFO) buffer of $N = 50$ elements. As suggested by the name, when a new event was added to the FIFO and placed in the first element, the events in the FIFO were shifted up one element, and the last element of the FIFO was deleted. The event in the first element was then mixed with all other elements in the FIFO of the same class. Events were deemed to be of the same class if the position of their respective primary collision vertices were within 8 cm in the longitudinal direction ($|\Delta Z_{vertex}| < 8$ cm). Furthermore, the difference in reference multiplicity between events was required to be less than 20%.

The same-event (red markers) and mixed-event (open markers) dielectron invariant mass distributions are shown in Figure 3.8 for minimum bias events, in which $\sim 12 \times 10^6$ events were analyzed. Due to the fact that there can be as many as 50 mixed events per same event, the mixed-event distribution normally lies at least one order of magnitude higher than the same-event distribution. The region of $1.8 < M_{inv} < 2.7$ (GeV/c^2) was used to scale the mixed-event spectrum down to the level of the same-event spectrum. The scale factor was determined by considering the ratio of the area underneath the same-event distribution (in the said region) to the corresponding area in the mixed-event distribution. The shape of the dielectron continuum is such that it is relatively high at low invariant mass and decreases for higher invariant mass values. As discussed earlier, the form of the same-event and mixed-event continuum is mainly dictated by the kinematic cuts imposed on the J/ψ decay daughters. In the vicinity of the J/ψ mass, the dielectron continuum does not vary rapidly with increasing invariant mass. This situation, where the background distribution is relatively flat, allows for the mixed-event distribution to make a good estimate of the exact shape of the background under the peak.

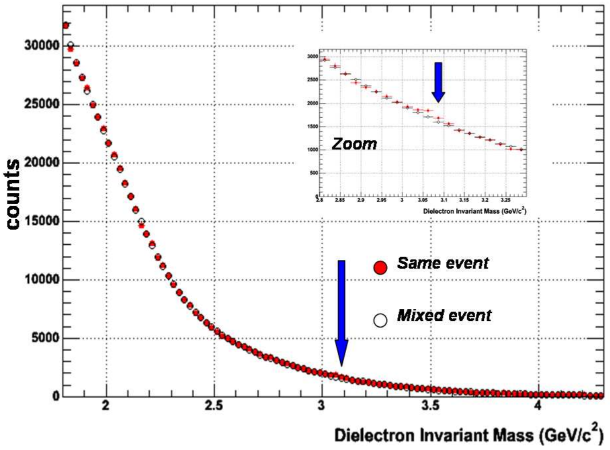

Figure 3.8: The dielectron invariant mass spectra are shown for same events (red circles) and mixed events (open circles). The arrows indicate the expected position of the J/ψ peak as listed in the Particle Data Book [Eid04]. Illustrated by the inset is a zoom of the distributions in the region around the J/ψ mass, where a small peak is discernible.

The background-subtracted dielectron invariant mass spectrum for minimum bias events is shown in Figure 3.9. The bars on the markers in the figure indicate the point-to-point, quadratic sum of the statistical uncertainties in the same-event and mixed-event distributions. There are fluctuations in the high invariant mass region that average out to zero. Fluctuations of higher magnitude are present in the low invariant mass region that nearly average out to zero, and, as will be discussed later, could be induced by residual correlations. There is a clear structure in the vicinity of the J/ψ mass.

Although the mixed event distribution makes a good estimate of the exact shape of the background, there still lie residual correlations that become manifest in the subtracted spectrum. Residual correlations may be brought about by a

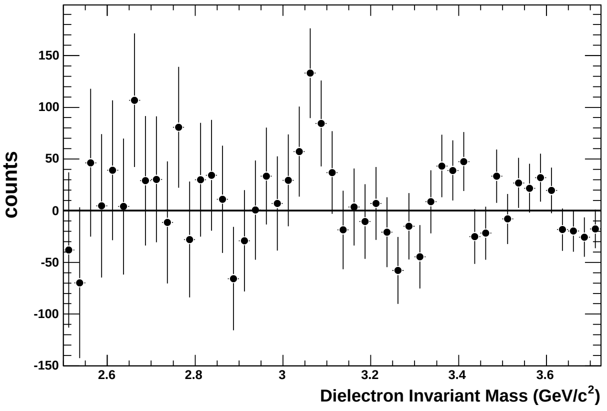

Figure 3.9: The background-subtracted dielectron invariant mass spectrum. The bars on the markers indicate the point-to-point statistical uncertainties.

number of different sources, among which are effects from Coulomb interaction between particles, other resonances, γ conversions to dielectron pairs in detector material, and detector effects such as limited acceptance and track merging. The Coulomb attraction between electron and positron pairs is observed right above the two electron mass threshold in the dielectron invariant mass distribution, which is well below the mass region of interest (~3 GeV/c^2). Since the relative invariant mass of the electron-positron pair from γ conversions is small, their correlation will appear as a residual background near the two electron mass threshold, which, again, is far below the J/ψ mass region. Variation in the collision vertex position between mixed events translates into a non-statistical variation in the single particle inclusive momentum distribution that may, in turn, lead to a mismatch between the mixed-event and same-event invariant mass distributions. This effect is kept to a minimum by requiring that different events have $|\Delta Z_{vertex}|$ $<$ 8 cm, as described earlier. In the vicinity of the J/ψ mass, the majority of the residual correlations will come from open-charm (e.g. D mesons) resonances, as discussed in Reference [Don05]. Although residual open charm correlations induce a positive net of fluctuations in the low invariant mass region of Figure 3.9, they stand below the mass region of interest and are small compared to the raw yield of the structure in the region around the J/ψ mass.

3.5 Extraction of the J/ψ Signal

The background subtracted invariant mass distribution for minimum bias events was fitted to a Gaussian function (Equation 3.1) in order to estimate the quality of the signal,

$$\frac{A}{\sqrt{2\pi}\sigma 40} e^{-(m-m_0)^2/2\sigma^2} \tag{3.1}$$

where A is the area of the Gaussian, m_0 is the resonance position, and σ is the resonance width. All of the aforementioned parameters were free in the fit. For reasons discussed in the previous section, the contribution of residual correlations in this analysis were not large enough to merit the use of an additional background function in the fitting procedure. The fitted minimum bias dielectron invariant mass spectrum is shown in Figure 3.10. The position of the resonance is 3.066 GeV/c^2, or 30 MeV/c^2 lower than the PDG [Eid04] mass of the J/ψ. The lower observed mass value may be attributed to limited detector resolution. Another source of the lower observed mass value could be Bremmstrahlung energy loss of electrons as they traverse detector material, which later manifests as a lower dielectron mass value. Simulations of J/ψ mesons reconstructed in the STAR TPC also indicate that the width of the dielectron mass peak should be about 45±10 MeV/c^2. The statistics available in this analysis are too poor to conclude that the observed width value of 26±10 MeV/c^2 is inconsistent with the expectations from simulation. In the region of two widths around the centroid of the peak, the signal-to-background ratio is about 1:25, and with the ∼330 raw J/ψ's observed this translates to a peak with a Gaussian significance of about 3.6σ.

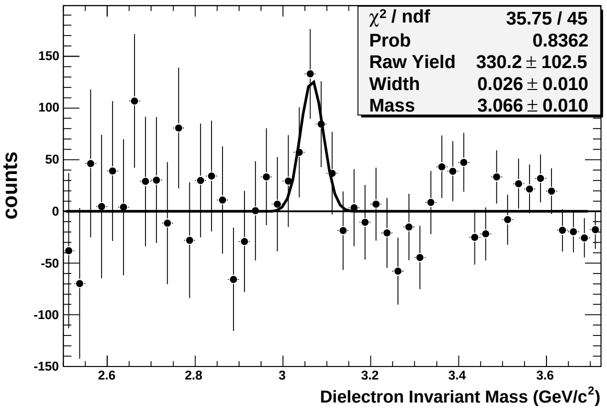

Figure 3.10: The background-subtracted dielectron invariant mass spectrum for minimum bias events. The distribution is fitted to a Gaussian function. Error bars shown are statistical errors only.

The background subtracted, Gaussian-fitted dielectron invariant mass distributions for all centrality classes are shown in Figure 3.11. The width parameter is held fixed to the value obtained in the mininum bias distribution when fitting the 40-80% and 20-40% centrality bins. This choice is motivated by the fact that the statistics are limited for those bins. The raw yield in each bin was obtained by summing up the measured yields in a region two (mininum bias) widths around the centroid of each bin, i.e. a ∼100 MeV/c^2 window around 3.066 GeV/c^2. The invariant mass distribution for the 0-20%, most central case does not exhibit a peak that is larger than the surrounding fluctuations. For this reason, the most central case was not fitted to a Gaussian function; instead, the net positive yield in a window of similar size served as the basis for an upper limit estimate of the J/ψ yield in central collisions. A detailed account of how this was achieved is given in Appendix B.

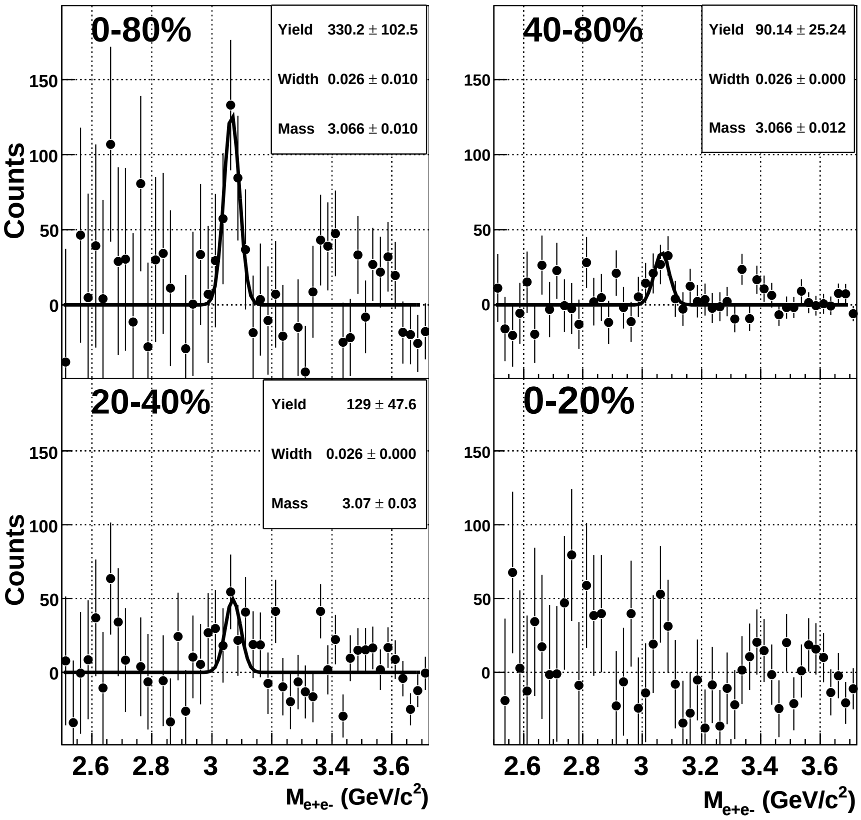

Figure 3.11: The background-subtracted dielectron invariant mass spectrum for minimum bias, 40-80%, 20-40%, and 0-20% events are shown. Error bars shown are statistical errors only.

Table 3.3 summarizes the attributes of the signal in each centrality class.

Centrality Bin	Raw Yield	Significance (σ)
0-80%	338	3.6
40-80%	100	3.4
20-40%	162	3.0
0-20%	178 $\rightarrow$ 0	90% C.L.U.L.

Table 3.3: Summary of dielectron signal attributes for each centrality class. For the most central case, a 90% confidence level upper limit is quoted.

CHAPTER 4

Monte Carlo Studies and Efficiency Corrections

The goal of STAR, as a detector system, is to measure the properties (e.g. kinematic properties and quantum numbers) of stable charged particles that emmanate from various collision systems. The ideal detector system has complete 4π coverage (acceptance) and senses every particle that impinges its active element with 100% probability (efficiency). A real detector system, such as STAR, typically does not have either of these attributes; the detection probability is not ideal and the coverage is not complete. Furthermore, a number of distortions hinder STAR's capacity to make measurements with ideal resolution. It is therefore of critical importance to understand the performance of the detector in order to extract quantitative measurements. In this Chapter, we will delve into techniques for understanding detector performance. We will later describe how studies of detector response are used to carry out efficiency and acceptance corrections for the J/ψ yields.

4.1 Particle Generation and Propagation

As with other large particle/nuclear physics experiments, understanding of detector response, biases, and distortions are carried out by implementing a simulation of the detector description and response. The fundamental concept is based on feeding kinematically known data to a detector response simulator, passing this simulated detector response to the event reconstruction software, and comparing the input with the final kinematic distributions which are output from the event reconstruction. If the detector response simulator is accurate, then this process allows one to quantify and differentiate among various inefficiencies and biases.

4.1.1 GEANT Detector Simulation

The first step is to simulate the passage of particles through the detector material. This is accomplished using the GEANT software package[BHH], which has become a standard simulation tool among many large particle physics experiments. GEANT is a highly refined and robust library that models electromagnetic and nuclear interactions of particles with matter. The software works by loading a detailed three dimensional model of all material present in the STAR interaction region, including the beam pipe, SVT, TPC gas, magnet, support structure, etc. GEANT then provides tools to propagate a given particle type through the detector model, simulating multiple scattering, energy loss, conversion, and particle decay along each step of the trajectory. The final output of GEANT is a full simulation of a particle and its corresponding interactions as it makes its way through the detector volume. Information relevant to the behavior of the TPC, such as the energy liberated at discrete points in the TPC gas, is then extracted from the output of the GEANT simulation.

4.1.2 TPC Response Simulator

A complex software package was developed to mimic the detector response to real data. The TPC Response Simulator (TRS)[Lon02] is the software package that simulates the response of the STAR TPC to the ionization of charged tracks in the TPC gas. The output from the GEANT simulation—the avalanche of electrons produced by the particles that ionize the TPC gas—is fed into the TRS package, which then carries out highly detailed calculations to simulate the drift, collection, amplification, and digitization of the electrons. Here, we will only give a brief description of the TRS algorithm. For a more detailed description of TRS, see Reference [Lon02].

The TRS algorithm follows four basic steps: *I*) ionization transport; *II*) charge collection; *III*) analog signal generation; and *IV*) digital signal generation. In the first step, the ionization transport package begins by transforming the energy loss of a charged particle (taken from GEANT) into a discreet number of electrons and diffuses the ensuing charge cluster, as it drifts toward the end caps, in both the transverse and longitudinal directions. In the second step, the drifting electrons are collected in the MWPC, where the primary signal amplification is modelled by a charge collection routine that implements the Yule-Furry process. The third step follows by considering the charge collected on the MWPC wires, which induces an image charge on the pad plane. The analog signal generation routine models this process by using the distribution of charge induced on a grounded pad plane. Finally, this analog signal is converted into an ADC value, thereby completing the response simulation.

4.1.3 Embedding and Association

The simulation procedure described in the previous section gives, to a good degree, an adequate representation of how the TPC responds to the impingement of charged particles. However, under real experimental conditions, the algorithm's capacity to reconstruct the trajectories of charged particles is influenced by a number of background sources. Among these is noise in the readout electronics, cosmic ray contamination, beam-gas background, and multiple interactions per readout event. The embedding technique takes into account these background sources. The embedding technique consists of mixing real triggered events with purely simulated events at the raw data level, whereupon event reconstruction is carried out. A small number of Monte Carlo tracks, pertaining to a resonance or particle of interest, are embedded into the real data by first running GEANT and TRS to simulate the digital signals of the detector. These digital signals are mixed with the signals from the real data stream and then fed into the event reconstruction chain. After reconstruction, an association algorithm is employed (at the hit level) to associate reconstructed tracks with the corresponding input simulated tracks. The reconstruction efficiency (and acceptance) can then be defined as:

$$\epsilon = \frac{RecTrack}{SimTrack} \tag{4.1}$$

where ϵ is the efficiency and acceptance, $RecTrack$ is the number of reconstructed tracks, and $SimTrack$ is the number of input Monte Carlo tracks. Figure 4.1 shows a diagram that summarizes the essential components of the embedding paradigm. Reconstructed tracks are the subset of input simulated tracks that, in addition to landing within the acceptance of the detector, were successfully detected. In essence, ϵ incorporates losses due to finite acceptance of the TPC and inefficiencies in the cluster finding algorithm, as well. The efficiency depends on the user-cuts, specific to an analysis, that a reconstructed track must pass to be accepted. A detailed account of the algorithms used to determine the efficiencies and their implementation can be found in Reference [Yam01].

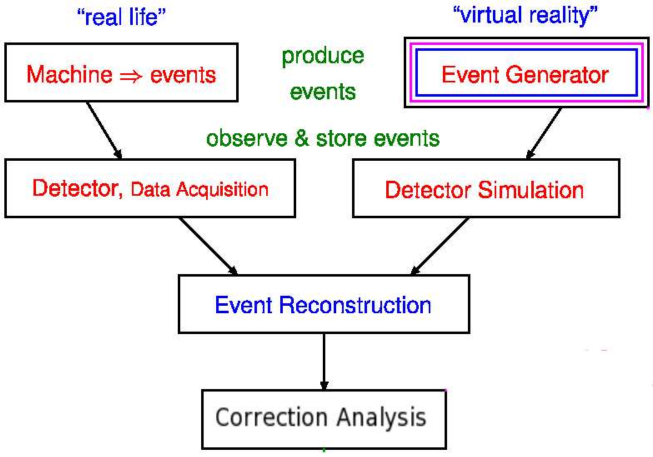

Figure 4.1: A diagram of the embedding process. Simulated tracks from an event generator are fed into a simulation of the detector, the output of which is then fed into event reconstruction software in conjunction with with real data. The correction analysis, via an association algorithm, is then carried out.

4.2 J/ψ Embedding Studies

In this analysis, Monte Carlo J/ψ's were extracted from events generated using the PYTHIA event generator [SMS06]. The PYTHIA program can be used to generate outgoing particles from collisions that closely resemble those in particle physics experiments. PYTHIA is based on a combination of analytical results and various QCD-based models. The J/ψ's generated by PYTHIA were selected so as to follow a flat transverse momentum distribution as well as a flat rapidity distribution. This was motivated by the need to have good statistics in order to adequately describe J/ψ efficiencies across the entire transverse momentum and rapidity spectrum. The electron-positron pairs from J/ψ decays were filtered through a simulated version of the STAR detector, in a manner described in the previous section. Simulated J/ψ's were embedded (one per event) into events that closely remembled those used in this analysis, namely minimum-biased, full-field events. These events were required, as was done in the analysis, to have a primary collision vertex within 30 cm of the center of the TPC in the longitudinal direction.

With the exception of cuts associated with a track's dE/dx attributes, the tracks that were deemed to be associated with input Monte Carlo decay electrons were required to satisfy the track quality cuts described in Section 3.3. Inefficiencies associated with dE/dx quantities are currently not well simulated in STAR [Dun]. Because of this fact, we had to resort to the scrutiny of the real data itself in order to account for inefficiencies brought about by dE/dx particle identification cuts and by requiring a certain number of dE/dx hit points ($nHitsDedx$) for each track. We must therefore take an interlude in the next two sections to describe the treatment of dE/dx-related cuts before considering the J/ψ embedding studies as a whole.

4.2.1 Corrections Related to Number the of dE/dx Hit Points

The number of dE/dx hit points is not completely well described in the current simulation of the STAR TPC. However, other quantities such as the regular number of hit points ($nHits$) of each track is well treated in the simulation. The correlation between the $nHits$ and $nHitsDedx$ can help us determine the number of electron candidates—and by extension, the number of J/ψ mesons—lost by imposing an $nHitsDedx$ cut [Xub]. Figure 4.2 shows a scatter plot of $nHits$ versus $nHitsDedx$.

In the case were no $nHitsDedx$ cut is imposed on each track, the number

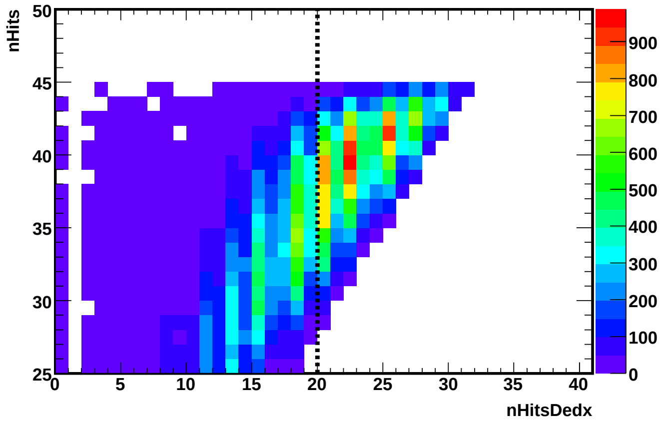

Figure 4.2: The regular number of hit poins is plotted versus the number of dE/dx hit points. The vertical line indicates the cut imposed on $nHitsDedx$.

of electron candidates corresponds to everything shown in the scatter plot, or all tracks with $nHits > 25$. In the event when tracks are also required to have $nHitsDedx > 20$, then the number of electron candidates selected corresponds to everything above the vertical line shown in the figure. Then, the fraction of electron candidates lost due to the imposition of an $nHitsDedx$ cut is simply ratio of the number of candidates in the latter case to the number in the former case. The fraction of pairs lost (J/ψ's) is the square of the aforementioned fraction. The inefficiency associated with an $nHitsDedx$ cut is strongly correlated with event centrality; fewer dielectron pairs are lost in peripheral events than in central events. Table 4.1 lists the fraction of dielectron pairs that survive the imposition of an $nHitsDedx$ cut for each centrality class.

4.2.2 Corrections Related to dE/dx PID Cuts

One of the cornerstones of this analysis is the set of electron selection and hadron rejection dE/dx cuts. An overwhelming number of hadrons would otherwise be

Centrality Bin	Fraction of Surviving Pairs
0-80%	0.327
40-80%	0.612
20-40%	0.430
0-20%	0.178

Table 4.1: The fraction of surviving dielectron pairs after imposing an $nHitsDedx$ cut. The fraction is listed for each centrality class.

selected had these set of cuts not been put in place. The resulting combinatorial background and associated computational time would make the search of the J/ψ impractical. It is therefore of critical importance to this analysis to assess the number of dielectron pairs lost after removing the hadron bands in a manner described in Section 3.3, even it entails not using (currently inadequate) simulation information. The idea was put forth [Sor] that the inefficiency associated with our dE/dx particle identification (PID) cuts can be assessed by isolating the electron band and examining the fraction of the band that remains after PID cuts.

Here, the isolation of the electron band was realized by employing the use TOFr timing information in conjunction with TPC dE/dx information. Charged tracks measured by the TPC were required to project onto the TOFr module, then a TOFr timing cut of $1 - 1/\beta < 0.03$ was applied, where β is the charged particle's velocity relative to the speed of light. Shown in Figure 4.3 is the track dE/dx as a function of momentum after imposing the TOFr timing cut. Unlike dE/dx plots shown in Section 3.3, here the hadron bands are effectively decoupled from the electron band.

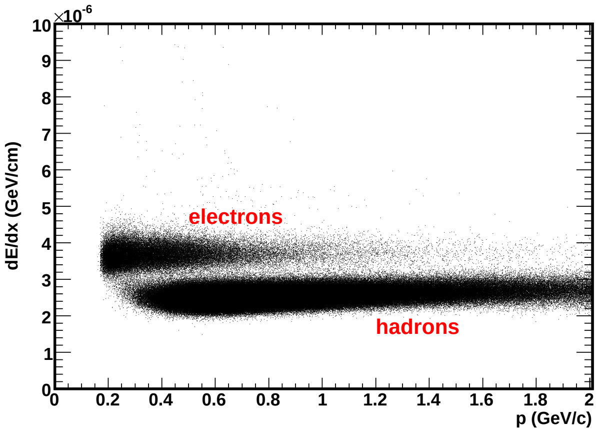

Figure 4.3: The TPC dE/dx versus track momentum. The electron band is isolated by applying TOFr timing cuts, as discussed in the text.

Figure 4.4 shows a projection of Figure 4.3 onto the dE/dx-axis for a momentum slice of $600 < p < 610$ MeV/c. The projection is essentially a superposition of two gaussian-like distributions; the structure located at low dE/dx values corresponds to the residual hadrons left after applying the TOFr quality cut and the structure at higher dE/dx values corresponds to the electrons. It has been established that the region above $dE/dx \sim 2.7 \times 10^{-6}$ GeV/cm can be suitably represented by the superposition of a Gaussian function (electrons) and an exponential function (hadrons) [Don05]. The distribution was fitted to the aforementioned function, the result of which is indicated by the black curve in Figure 4.4. The electron portion of the compound function is indicated by the green-colored Gaussian curve. The subset of tracks obtained after imposing the hadron rejection cuts are indicated by the red histogram. For a given momentum slice, the probability that a track meets the requirements of the dE/dx PID cuts is given by the ratio of the number of selected tracks (red histogram) to the total pool of electron candidates (Gaussian curve).

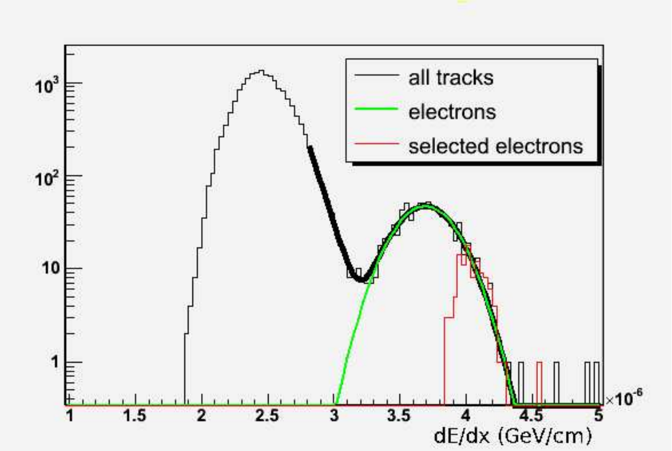

Figure 4.4: Track dE/dx after TOFr quality cuts. The distribution above corresponds to tracks with $600 < p < 610$ MeV/c.

The above scenario can be examined as a function of track momentum. Shown in Figure 4.5 is the probability that a given electron candidate passes the PID cuts as a function of momentum. The probabilities are plotted from 500 MeV/c to 3 GeV/c; the lower limit is motivated by the fact that our analysis is only concerned with tracks above 500 MeV/c (see Section 3.3). Because of relativistic effects, the electron band naturally decouples from the all other bands for $p > 1.5$ GeV/c, hence the saturation of the selection probability in that momentum region. The momentum dependence of the selection probability was determined for the 0-20%, 20-40%, and 40-80% centrality classes. These were then folded into the association algorithm described in Section 4.1.3.

4.2.3 J/ψ Detection Efficiency

In the two previous sections we assessed the inefficiencies associated with dE/dx-related quantities, which were not properly accounted for in the simulations. These were incorporated into the rest of the embedding analysis by folding their

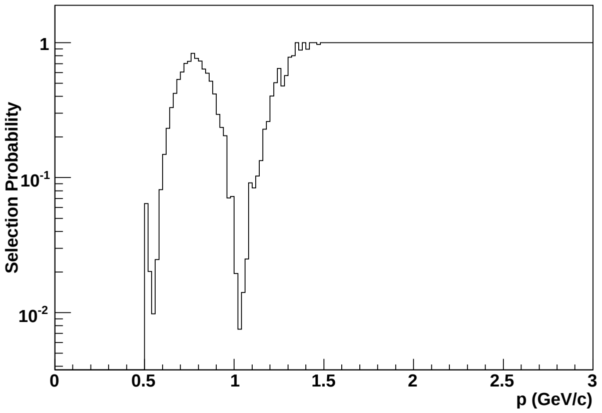

Figure 4.5: Shown is the selection probability for tracks after the application of dE/dx PID cuts. The case shown here pertains to central events.

respective inefficiencies with those already assessed in the simulations. For the dE/dx PID cuts, this was achieved by on a track-by-track basis by weighting a track's reconstruction efficiency with the corresponding selection probabilities. For each centrality class, the fraction of J/ψ's lost due to the $nHitsDedx$ cut was incorporated in the overall J/ψ detection efficiencies as global multiplicative factors.

Figure 4.6 shows the J/ψ reconstruction efficiencies as a function of p_T for all centrality classes. The efficiency is a strong function p_T and centrality. For all centrality classes, the efficiency appears to have a positive slope in the region of $0 < p_T < 0.25$ GeV/c. Beyond that, the efficiency dips down until $p_T \sim 1.5$ GeV/c, where again it raises and eventually reaches a plateau in the vicinity of $p_T \sim 3.5$ GeV/c. The dip in the efficiency is induced by the dE/dx PID cuts, and the strong centrality dependence is induced by the $nHitsDedx$ cuts, which also exhibit a strong centrality dependence.

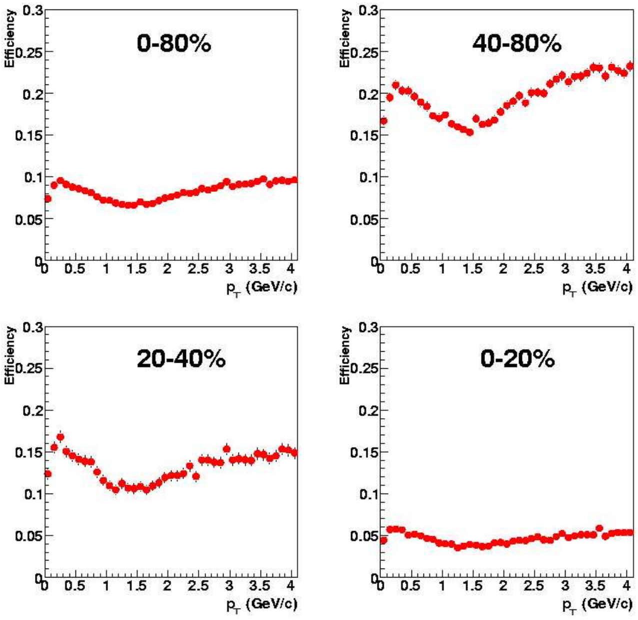

Figure 4.6: Fractional efficiency and acceptance factors as a function of p_T for the 0-20%, 20-40%, 40-80% and 0-80% centrality classes.

4.2.4 Application of Corrections via Monte Carlo Integration

After determining losses due to finite acceptance of the TPC and inefficiencies in the cluster finding algorithm, the raw spectra are typically (see Reference [Yam01]) corrected by scrutinizing the background-subtracted invariant mass distribution in a certain p_T window, extracting the number of candidates, and correcting these by the corresponding efficiency in that p_T window. In this analysis, the available statistics do not allow for corrections to the raw spectra via the application of the aforementioned method. Instead, corrections in this analysis are carried out via Monte Carlo Integration (MCI), also known as Numerical Integration. This kind of technique is particularly useful for correcting data in analyses that are statistically limited [HX].

The MCI algorithm follows these basic steps:

1. *Extract Raw Yield*: Obtain the p_T-integrated number of candidates, N, in a given mass window of the background-subtracted invariant mass spectrum.
2. *Correct the Yield*: Out of the list of J/ψ candidates, randomly select N candidates and weight each of these by its corresponding efficiency factor, then add them to obtain the corrected yield:
$$\frac{dN}{dy} = \sum^{N} \frac{1}{\epsilon_{random}(p_T)} \tag{4.2}$$
3. *Collect Ensemble*: Carry out the previous step over a large number of iterations to obtain a distribution of possible corrected yields.

The first step is carried out in the same fashion described in Section 3.5, where the raw yield in each bin was obtained by summing up the measured counts in a mass window around the centroid of the peak. The size of the mass window was fixed in all centrality classes and extended from 3.0 to 3.125 GeV/c^2. This range was determined by considering the width of the peak in minimum bias events.

In the second step, N dielectron candidates are randomly selected from our total pool of candidates in the kinematic region of interest, i.e. $|y_{pair}| < 0.5$ and $3.0 < M_{pair} < 3.125$ GeV/c^2. Essentially, our total pool of candidates comprises the same-event dielectron invariant mass distribution. Each of the selected candidates is then weighted by the efficiency factor pertinent to its transverse momentum. As indicated by Equation 4.2, the modified contributions by each candidate to the total yield are added up to obtain the corrected yield.

Due to the random element of the procedure discussed thus far, there will be an intrinsic systematic error. This error, along with the most probable value of the corrected yield, is determined in the third step. This step consists of evaluating

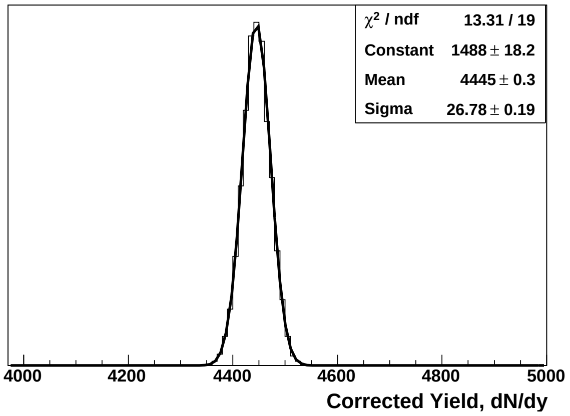

Figure 4.7: Distribution of possible corrected yields as determined by the Monte Carlo Integration algorithm. The case shown above pertains to minimum bias events. The mean of the Gaussian function corresponds to the most probable value of the corrected dN/dy, while the width of the distribution corresponds to the intrinsic error in the correction procedure.

Equation 4.2 many times in order to collect an ensemble of possible corrected yields. Figure 4.7 presents the distribution of corrected yields for minimum bias events. The distribution can be well represented by a Gaussian function; the mean of the Gaussian function corresponds to the most probable corrected yield, and the width corresponds to the intrinsic systematic uncertainty of the MCI procedure. The width of the distribution is quite small compared to its mean value, indicating that the systematic uncertainty brought about by the random element in the MCI procedure is almost negligible.

The second step in the MCI algorithm can be modified to take into account the statistical uncertainty in the measured yields. Instead of randomly selecting a fixed number of N candidates, we can select $N \pm \delta N$ candidates, where δN is the statistical uncertainty in the raw counts—this is determined from the Gaussian

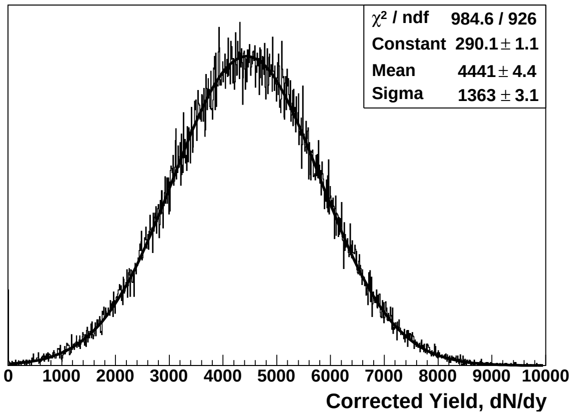

Figure 4.8: Distribution of possible corrected yields as determined by the Monte Carlo Integration algorithm. The algorithm was modified to incorporate the statistical uncertainty in the raw measured yields, indicated by the width of the Gaussian function.

fits to the signal in each centrality bin, as described in Section 3.5. The resulting distribution from the third step then gives a much broader spread of values, as presented in Figure 4.8, that reflect the statistical uncertainty of the measured yields. It should be noted that systematic uncertainty in the correction procedure, though small, is also incorporated in the width of the Gaussian function that is used to fit the distribution. Table 4.2 lists the corrected J/ψ yields in each centrality bin along with their corresponding statistical uncertainties. For the most central case an upper limit with 90% confidence level is quoted. If one takes the net, uncorrected number of counts ($\sim$80) seriously, then the corresponding corrected yield will be 1862±997. This can be interpreted as the most probable value of the yield in central events.

Centrality Bin	Corrected Yield
0-80%	4441±1363
40-80%	565±154
20-40%	1336±481
0-20%	4139 → 0

Table 4.2: Summary of corrected J/ψ yields for each centrality class. For the most central case, the corresponding 90% confidence level upper limit is quoted.

CHAPTER 5

Systematic Uncertainties

In this chapter, we will delve into our assessment of the major systematic uncertainties in our J/ψ yields. As with all analyses of this kind, there are a number of factors that limit the resolution of the measurement. Systematic uncertainties are those which are independent of statistical uncertainties. In this analysis, however, the study of systematic uncertainties was limited due to the relatively low statistics available. This is something that is specially true for the uncertainties in the particle identification technique, as will become evident in Section 5.2.

5.1 Efficiency Calculation

Losses due to limited detector acceptance and detection capacity were carried out in part with a simulation of the detector. While great effort has been taken to assure that simulations properly gauged detector response under a myriad of circumstances, there are uncertainties that lie in the inability of the simulation to completely describe the detector response. In order to gauge disparities between real and simulated detector response, we varied track quality cuts outlined in Table 3.2 and the corresponding effect on the yields were studied. Typically, one would achieve this by varying the cuts in the data itself. The size of the data sample used in this analysis was orders of magnitude higher than in previous years and such a study would require many weeks of computing time, which effectively renders it unpractical. Instead, we opted to vary the corresponding track quality cuts in the embedding analysis.

Special care was taken when varying the $nHits$ cut. In Section 4.2.1 we described how the correlation between $nHits$ and $nHitsDedx$ was used to assess the inefficiency associated with the $nHitsDedx$ cut. When varying the $nHits$ cut, the corresponding modified inefficiency of the $nHitsDedx$ cut was taken into account. The $nHits$ cut was systematically varied away from the nominal value of 25. Setting the $nHits$ cut in minimum bias events to 26, 27, and 28 gives rise to a deviation from the nominal yields of 2.1%, 4.0%, and 6.6%, respectively. The deviation obtained when varying the $nHits$ cut by 2 gives the best assessment of the uncertainty in the yields based on our current understanding of the behavior of $nHits$ cuts in the simulations. We note that, among all track quality cuts, uncertainties in the yield from $nHits$ and $nHitsDedx$ cuts was the highest; each of the other track quality cuts contributed no more than 1% to the yields.

The intrinsic error associated with the Monte Carlo integration technique used to carry out the corrections was already described in Section 4.2.4, and was found to be no more than 1% for each centrality class.

5.2 Particle Identification

In Section 4.2.2 a detailed assessment of losses due to dE/dx particle identification cuts was given. For reasons explained in that section, the method used to carry out that assessment was unconventional. The method consisted of using TOFr timing information to isolate and dissect the electron band. By virtue of being a prototype module, the TOFr only covers $\sim$1% of the total TPC acceptance, which places a great limitation on the number of particles that impinge the detector, and thus the available statistics. The resulting small TOFr data sample placed, in turn, substantial limitations on the certainty by which PID inefficiencies were determined.

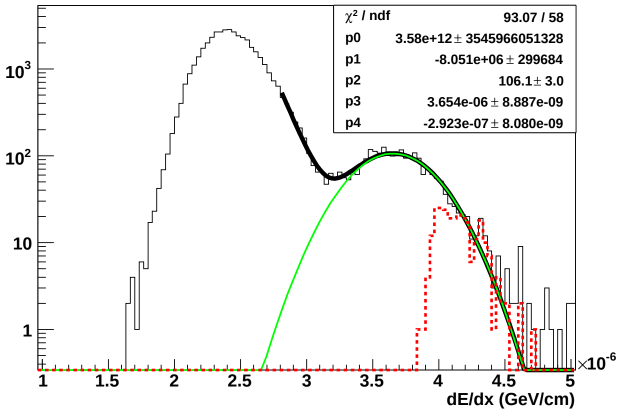

Figure 5.1: The dE/dx distribution for a given momentum window. The distribution is fitted to a compound function, the quality of which depends on the available statistics.

For a given momentum window, the number of tracks within the electron band was obtained by fitting the dE/dx distribution to a compound function (Figure 5.1). The electron band was represented by the Gaussian component of this function. The available statistics in a given momentum window was reflected in the quality of the fit; a dE/dx distribution with poor statistics yielded a fit with parameters carrying large uncertainties. The uncertainty in the area underneath the Gaussian represented the uncertainty in the number of tracks in the electron band. This uncertainty was determined for each momentum window. The effect on the corrected yield was gauged by running the embedding analysis with modified PID probability factors, which incorporated the aforementioned uncertainties. The ensuing systematic uncertainty in the corrected yields was found to be 11.7%, 8.6%, 7.9%, and 15.2% for the 0-80%, 0-20%, 20-40%, and 40-80% centrality bins. The strong centrality dependence is due to the fact that there is a greater number of tracks in a central event than in a peripheral event, so the limitations induced by limited statistics are even more pronounced for the peripheral centrality bin.

5.3 Background Subtraction

The event mixing technique was used to describe the combinatorial background from the random combination of oppositely charged tracks. Alternatively, the combinatorial background could have been assessed by constructing the invariant mass distribution of like-signed charged tracks. Although the like-sign distribution has a shape identical to the mixed-event distribution, large statistical fluctuations hinder its ability to accurately describe the background in the vicinity of the J/ψ mass. Nevertheless, the statistical fluctuations were mitigated by fitting the like-sign distribution to a polynomial, and assigning *that* as our background. The same-event distribution was subtracted by the polynomial function, and the resulting invariant mass spectrum was fitted to a Gaussian, in the same fashion described in Section 3.5. As shown in Figure 5.2, the dielectron peak is clearly discernible but the corresponding raw yield is about 10% less than normally obtained when using mixed-event subtraction. We assigned the observed disparity in the raw yield between the two methods as a systematic uncertainty. Again, the available statistics limit our ability to assess this uncertainty, and thus we assume that this 10% systematic error is common to all centrality classes.

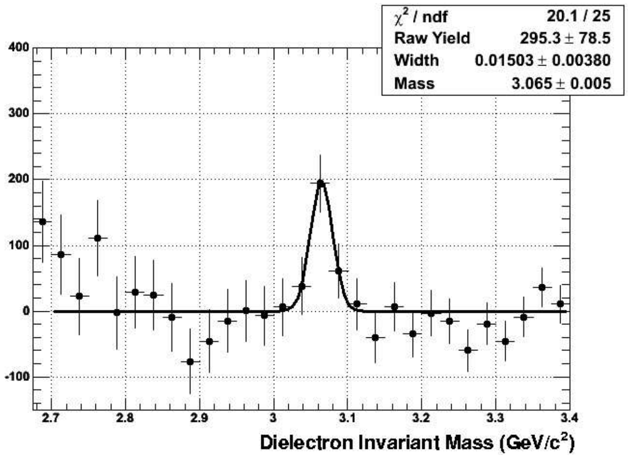

Figure 5.2: Dielectron invariant mass distribution for minimum bias events obtained using like-sign subtraction, as explained in the text.

5.4 Summary of Systematic Uncertainties

The contributions to the overall systematic uncertainty in the corrected yields for each centrality class were assessed. Table 5.1 lists the relative error in the yield from each source. The total systematic uncertainty for each centrality class was determined by adding the individual contributions from each source in quadrature. The largest source of uncertainty is attributed to the dE/dx PID cuts, followed by the uncertainty in background subtraction.

Error Source	0-80%	0-20%	20-40%	40-80%
Track quality	4.1	6.6	3.9	3.1
MCI technique	0.5	0.9	1.0	1.0
Bkg. subtraction	10	10	10	10
dE/dx PID cuts	11.7	8.6	7.9	15.2
Total	15.9	14.8	13.4	18.5

Table 5.1: Summary of relative systematic uncertainties in the corrected J/ψ yields for all centrality classes.

CHAPTER 6

Results and Discussion

6.1 Centrality Dependence of Scaled J/ψ Yields

In Section 1.2.4 we enumerated a number of experimental observables associated with J/ψ measurements. These mainly involve studying the centrality (or, alternatively, the collision energy) dependence of J/ψ production and the transverse momentum dynamics. In this analysis, due to limited statistics, we will restrict ourselves the scrutiny of the centrality dependence of J/ψ production. Of particular interest here is the centrality evolution of the J/ψ invariant rapidity density per event, dN/dy, at mid-rapidity ($|y_{J/\psi}| < 0.5$). The J/ψ dN/dy will naturally increase with increasing centrality because of the higher parton flux in central collisions. The trivial dependence of the invariant yield on the size of the collision system can be factored out by scaling dN/dy by the average number of binary collisions. Quantities such as the average number of binary collisions and average number of participating nucleons cannot be directly measured. In STAR, the average value of these quantities was determined by the implementation of a Monte Carlo Glauber (MCG) model of relativistic heavy ion collisions. In the MCG model, many body interactions are approximated as the simple superposition of elementary nucleon-nucleon interactions. A detailed treatement of Glauber calculations in STAR can be found in Appendix E of Reference [Mil03]. The average number of collisions and participants for each centrality class is listed in

Table 6.1.

centrality	$\langle N_{bin} \rangle$	$\langle N_{part} \rangle$
$0 - 20$	765±67	280±7.35
$20 - 40$	294±45	141±9.9
$40 - 80$	57±14	42±6.9
$0 - 80$	293±41	126±7.9

Table 6.1: The average number of binary collisions and average number of participants for each centrality class.

The corrected yield per event, $B_r dN/dy$, where B_r is the branching ratio of J/$\psi \rightarrow e^+e^-$, scaled by the average number of binary collisions ($\langle N_{bin} \rangle$) and plotted as a function of the average number of participants ($\langle N_{part} \rangle$) is shown in Figure 6.1. Here, we chose to scale dN/dy by $\langle N_{bin} \rangle$ instead of other quantities such as $\langle N_{part} \rangle$ because the production of J/ψ's is more directly related to $\langle N_{bin} \rangle$. By and large, the resolution of the measurement is limited by statistics. The bars indicate the statistical uncertainty and the systematic uncertainty is represented by the bands. The errors associated with the MCG model calculations are incorporated in the bands shown in the figure.

Figure 6.2 shows our results in comparison to binary collision scaling [Adl06a] (indicated by the horizontal line), which is obtained from the corresponding results in elementary $p + p$ collisions. The uncertainties in our measurements are too large at the moment to make a strong conclusion about the exhibited trend. If one takes the most probable value of the scaled $B_r dN/dy$ in the most central bin seriously, a downward sloping trend is somewhat discernible; which can be loosely interpreted as the onset of J/ψ suppression. The majority of the J/ψ yield is supposed to originate in central events, so one could argue that the absence

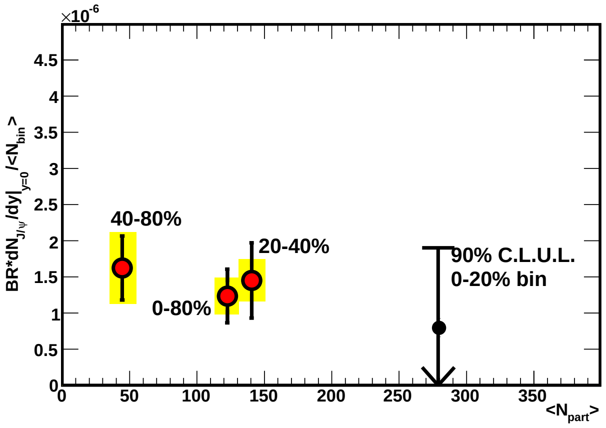

Figure 6.1: The J/ψ yield per event scaled by the number of binary collisions versus the number participants for all centrality classes, as indicated in the figure. For the most central case, the most probable value and the 90% confidence level upper limit are shown.

of a strong signal is indicative of suppression mechanisms at play. However, we cannot make this conclusion with confidence because the lack of a signal in central events could very well be due to the higher background conditions present. Furthermore, ordinary nuclear effects can become prominent in central collisions and have an effect on the observed scaled yields.

Figure 6.3 shows a comparison between our results and PHENIX results from Run 2 [Adl04]. The statistics available to PHENIX in Run 2 were extremely limited, so they opted to quote upper limits for all three exclusive centrality classes. For the mid-central and most peripheral centrality classes they indicated the most probable values for the scaled invariant yields (shown by the markers). Given the limited statistics in our results and PHENIX Run 2 results, there is a fair level of agreement between the two, particularly for the mid-central and most peripheral collisions.

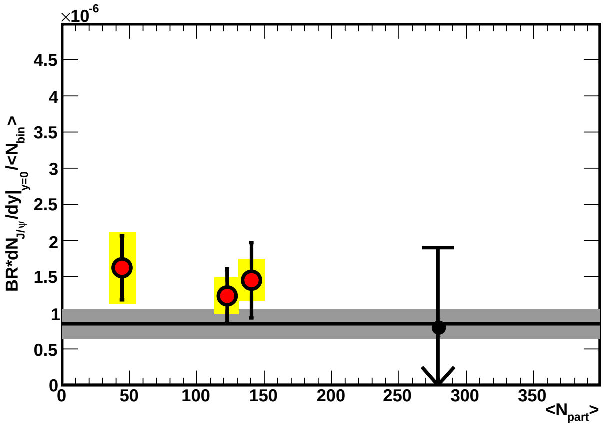

Figure 6.2: The J/ψ yield per event scaled by the number of binary collisions versus the number participants for all centrality classes. Binary collision scaling, along with its corresponding uncertainty (grey band), is also shown for reference.

A similar comparison to PHENIX's recent Run 4 [Per05] results is shown in Figure 6.4. The available statistics to PHENIX in Run 4 were at least an order of magnitude more than in Run 2, which is quite evident by the small uncertainties in their recent measurements. Our results are consistently higher than PHENIX results from Run 4. Because of the large error bars (both systematic and statistical) in our measurements, the two results are consistent within one standard deviation. The constrasting agreement between the results shown in Figure 6.3 and Figure 6.4 simply indicates the sensitivity of the measurement to the available statistics.

6.2 Comparison to Theoretical Models

In Sections 1.2.2 and 1.2.3 we gave a description of a plethora of models that make various predictions about fate of the J/ψ in heavy ion collisions. Most of

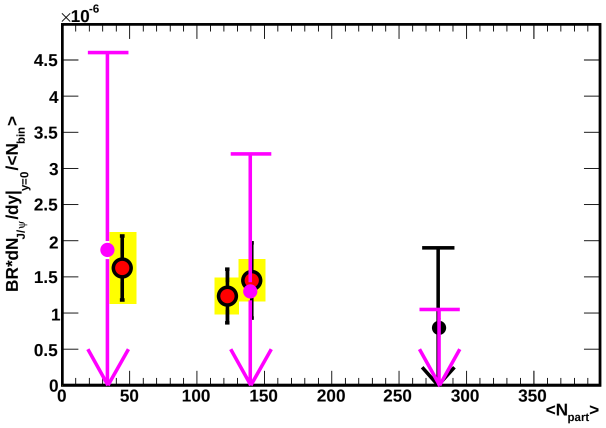

Figure 6.3: Comparison between our results and PHENIX results from Run 2.

these models can be categorized as either based on dissociation mechanisms or also containing regeneration mechanisms; the latter allowing for the possibility of an enhanced abundance of produced J/ψ's. Most of the models described in Chapter 1, namely those from References [KKS05, GR01], come very close to describing the recent PHENIX results from Run 4 [Per05]. We can therefore conclude here that comparisons to those theoretical models would reveal them to be consistent with our results within large errors. Our measurements, given their rather large uncertainties, lack the discriminatory power to disentangle one model from another.

There is one class of model [ABR03], however, that has the potential of predicting extreme enhancement of J/ψ production. In this model, which is based on Statistical Hadronization, all primordially produced J/ψ's get dissociated in the plasma. Furthermore, the model expects all observed J/ψ's to be exclusively produced from the recombination of thermalized charm-anticharm quarks at chemical freezeout. The aforementioned regeneration mechanism could, under certain circumstances, give rise to copious J/ψ production. The predictions from the model

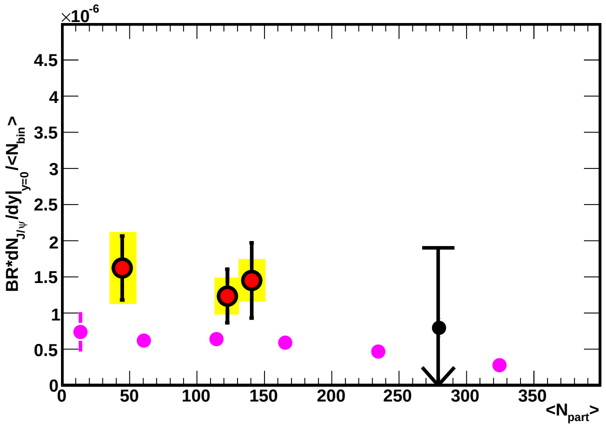

Figure 6.4: Comparison between our results and PHENIX results from Run 4.

are very sensitive to the assumed value of the total charm production cross section, $\sigma_{c\bar{c}}$. The J/ψ production is expected to follow a quadratic dependence on the $\sigma_{c\bar{c}}$. Figure 6.5 shows a comparison between our results and the expectations from Statistical Hadronization when assuming the latest differential charm cross section determined from pQCD [CNV05], $d\sigma^{pQCD}_{c\bar{c}}/dy = 63.7{+}95.6{-}42.3\,\mu$b. The most probable values predicted by the model (indicated dot-dashed curve) seem to reasonably describe the data. The rather large uncertainties in $d\sigma^{pQCD}_{c\bar{c}}/dy$ are reflected in the large range of values expected by the model.

Before continuing with further model comparisons, an interlude is in order. Measurements of $\sigma_{c\bar{c}}$ have been made by both STAR [Ada05b, Don05, Zha06] and PHENIX [Adl06c, Adl05]. Both set of measurements are based on semileptonic decays of open-charm hadrons (Figure 6.6). Initial measurements made by STAR [Ada05b] and PHENIX [Adl05] were barely consistent within large errors; the PHENIX result gave a substantially lower value of $\sigma_{c\bar{c}}$. Recent results from both collaborations improved consistency within errors. It is important to note that results from STAR [Zha06] have the advantage of constraining the value of

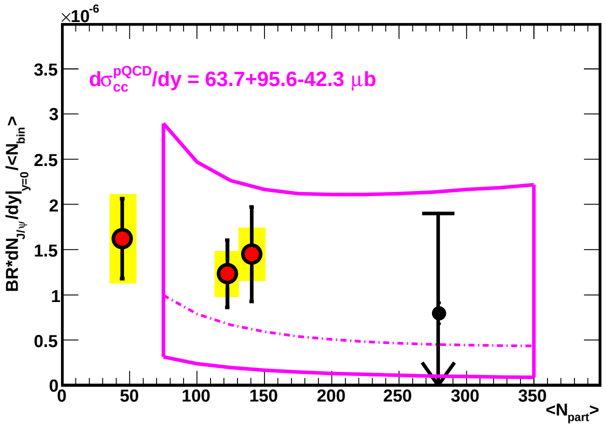

Figure 6.5: Comparison between our results and the expectations from a Statistical Hadronization model [ABR03]. The dot-dashed curve indicates the most probable values for the scaled J/ψ yields and the surrounding solid curve represents the full set of values expected from the model when considering the uncertainty in $d\sigma_{c\bar{c}}^{pQCD}/dy$.

$\sigma_{c\bar{c}}$ with low-p_T measurements, e.g. low-p_T muons, and can therefore be quite accurate. Despite their arguable differences, these experimental endeavors reveal $\sigma_{c\bar{c}}$ to be much larger than the expectations from pQCD as well as predictions from other theoretical models, as illustrated by Figure 6.6. By and large, model expectations do a rather miserable job in describing the experimentally observed cross sections. With this in mind, we carry on with our discussion.

Shown in Figure 6.7 is the comparison between our results and the expectations from Statistical Hadronization while assuming a differential cross section consistent with the STAR and PHENIX measurements of $\sigma_{c\bar{c}}$. By and large, the model grossly overpredicts the magnitude of the scaled J/ψ yields. The model predictions that use the PHENIX $\sigma_{c\bar{c}}$ come close to our measurements only for the lower-most values allowed by the uncertainty in the PHENIX measurement.

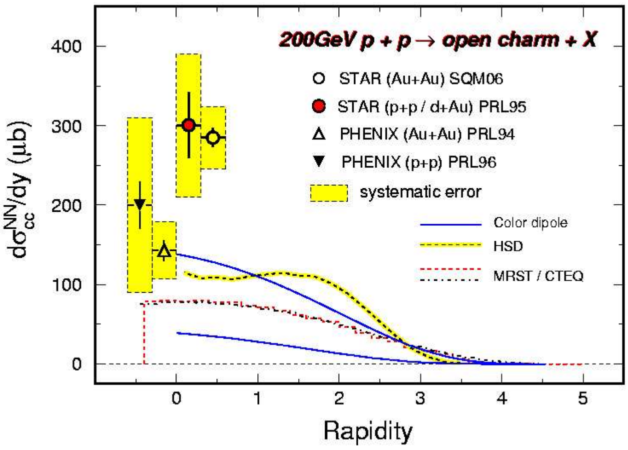

Figure 6.6: The $\sigma_{c\bar{c}}$ is plotted as a function of rapidity. Measurements from PHENIX, STAR, and the expectations from a variety of models are shown. Calculations substantially underpredict the magnitude of $\sigma_{c\bar{c}}$ at mid-rapidity. Figure taken from [Xua].

The model predictions, while assuming the (published) STAR-measured $\sigma_{c\bar{c}}$, are far above our scaled J/ψ yields.

Based on the comparisons made thus far, we can rule out this implementation of Statistical Hadronization as a plausible description of J/ψ production in heavy ion collisions at RHIC. This conclusion reflects the author's bias that the STAR measurement of the total charm cross section is more accurate and reliable than the corresponding measurement by PHENIX, as can be seen in the recent preliminary results shown in Figure 6.6. However, it should be noted that this description of J/ψ production is based on theoretical ideas that were very successful in describing particle-antiparticle ratios in heavy ion collisions [BHS99]. In its current form, the model takes no consideration of the kinematic properties of the J/ψ. Perhaps a more detailed description of J/ψ production, including underlying dynamics such as momentum and space correlations, may allow for a more accurate description of the observed J/ψ yields.

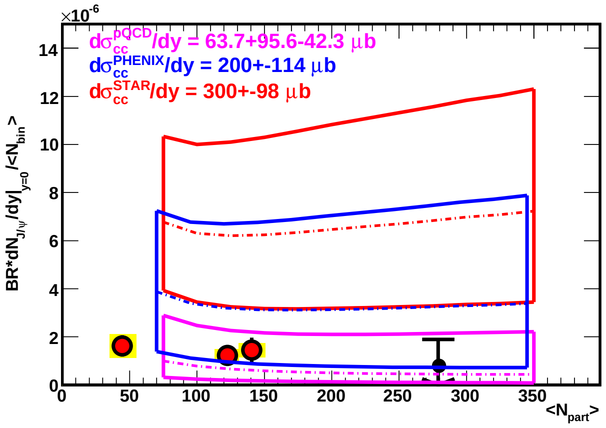

Figure 6.7: Comparison between our results and the expectations from a Statistical Hadronization model [ABR03] when assuming the differential charm cross section measured by PHENIX [Adl06c] (blue curves) and STAR [Ada05b] (red curves). The dot-dashed curves indicates the most probable values for the scaled J/ψ yields and the surrounding solid curves represent the full set of values expected from the model when considering the uncertainty in $d\sigma_{c\bar{c}}^{STAR}/dy$ and $d\sigma_{c\bar{c}}^{PHENIX}/dy$.

6.3 Conclusion

We have measured properties of the J/ψ mesons through the dielectron decay channel in $Au + Au$ collisions at $\sqrt{s_{NN}} = 200$ GeV. A systematic study of the scaled yields as a function of collision centrality was carried out. This constitutes the first measurement of J/ψ meson production by the STAR collaboration at RHIC.

Although the statistics associated with our measurements limit their discriminatory power, our result indicates that a model of J/ψ production in the final stages of the collision via Statistical Hadronization does not adequately describe the data. Essentially, what we can rule out is the notion of extreme enhancement via regeneration mechanisms in $Au+Au$ collisions at RHIC energies. The aforementioned model consisted of total screening coupled with copious production. Perhaps a more delicate interplay between regeneration and dissociation mechanisms may be required to explain our observations.

A more conclusive statement about regeneration and dissociation models in general, and its implications to the discovery of the QGP, has to a wait the much larger and cleaner data sets that will be attainable in future RHIC runs.

6.4 The Future

The experimental endeavors that have led to the completion of this analysis only mark the beginning of J/ψ studies in STAR. As noted in earlier chapters, a thorough disentanglement of regeneration and dissociation scenarios will require a complete characterization of the J/ψ as a function of transverse momentum and collision centrality, which will require that further, higher-luminosity runs be carried out at RHIC. With the integration of new detector subsystems and topological triggers, the STAR detector will be specially poised to pursue J/ψ studies in relativistic heavy ion collisions.

Among the future upgrades is the barrel Time of Flight (TOF) [Llo04a] detector, which will be based on the multi-gap resistive plate chamber technology used by the TOFr prototype module. The TOF detector will provide full azimuthal coverage and two units in pseudorapidity within -1.0 $< \eta <$ 1.0. Combined with existing STAR detectors, the barrel TOF detector will give STAR extensive electron identification—and by extension J/ψ reconstruction—capabilities. As illustrated in Figure 6.8, the barrel TOF, in conjunction with the barrel EMC, will improve the J/ψ detection efficiency by an order of magnitude. The STAR detector, by virtue of having extensive acceptance, may surpass even the PHENIX detector in the number of J/ψ's recorded.

Of great interest, along with the study of yields and transverse momentum dynamics, is the study of the J/ψ azimuthal anisotropy, i.e. "flow", in heavy ion collisions. If azimuthal anisotropy studies demonstrate that the J/ψ indeed flows, then the fact could constitute strong evidence of thermalization of charm quarks within the hydrodynamic framework. It would take an extensive number of interactions with the light quarks that comprise the QGP in order for charm quarks to develop flow; it would therefore be necessary for the light quarks themselves to be thermalized. Verification of thermalization is of paramount importance in order for one to qualify the hot, dense matter created at RHIC as a QGP.

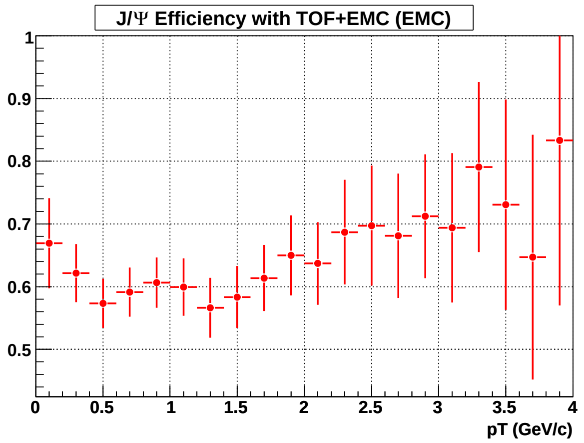

Figure 6.8: The J/ψ detection efficiency and acceptance as a function of p_T when using the full barrel TOF in conjunction with the barrel EMC detector.

Part of the J/ψ studies in STAR involve establishing a reliable baseline by which to understand results from high-energy $A+A$ collisions. In STAR, this will be achieved in part by measuring the properties of J/ψ production in elementary $p+p$ collisions. During the 2005 $p+p$ run, a special J/ψ trigger was commissioned that used tracking information from TPC and energy measurements from the Barrel EMC. The implementation of this trigger showed a promising signal at the 5σ level [DC]. This trigger is being implemented in the 2006 $p+p$ run and will put our current studies into perspective. To date, the trigger has not been used in $Au+Au$ collisions because the high multiplicity environment has made its implementation unfeasable. The barrel TOF detector will augment the trigger's background rejection capabilities, and thus allow for its possible implementation in $Au+Au$ collisions.

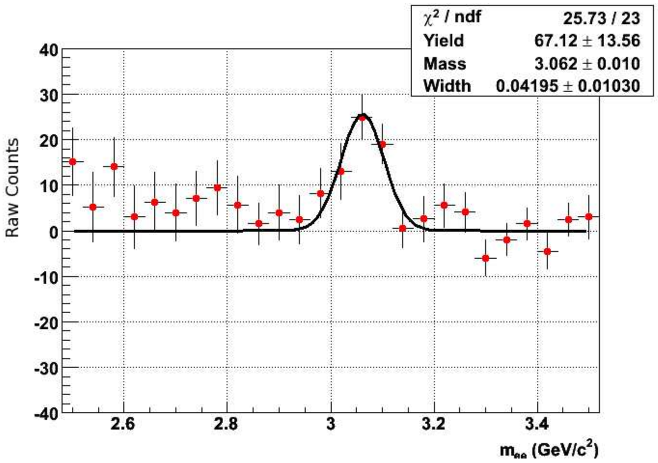

Figure 6.9: Dielectron invariant mass spectrum from $p+p$ collisions at 200 GeV. The result shown above is the product of the implementation of a special J/ψ trigger [DC], as discussed in the text.

As it stands, our knowledge of J/ψ production in elementary processes is incomplete. Studies of J/ψ production in $p+p$ collisions suggests that about

1% of charm quarks contribute to the formation of J/ψ mesons, without firm knowledge about the relevant formation mechanism. In order to come to a good understanding of the role of the J/ψ meson in relativistic heavy ion collisions we will need to understand the J/ψ formation mechanism, which can be achieved by both closed charm and open charm studies. The latter will be addressed in STAR with the integration of the Heavy Flavor Tracker, the purpose of which is to extend STAR's capability to open charm states such as the D meson, by the measurement of displaced vertices.

In essence, the aforementioned future developments in STAR will allow us to carry out detailed experimental work on total yields, transverse momentum spectra, and azimuthal anisotropy as a function of collision centrality. These studies will uncover information about the relevant underlying dynamics of J/ψ formation and propagation in the hot and dense medium created at RHIC.

APPENDIX A

Kinematic Variables

Throughout the content of this thesis a number of kinematic variables were used to describe particle trajectories and differential multiplicities. These were chosen because they are either Lorentz invariant or transform trivially under Lorentz boosts along the collision (beam) axis, which is taken to coincide with the z-axis of our coordinate system. The momentum components p_x and p_y are unchanged by a boost along z so we define and use the transverse momentum of a particle,

$$p_T = \sqrt{p_x + p_y}. \tag{A.1}$$

A longitudinal variable commonly used is rapidity,

$$y = \frac{1}{2} \ln \left(\frac{E + p_z}{E - p_z} \right), \tag{A.2}$$

which essentially provides a gauge of a particle's fractional energy along the beam axis, and has the advantage of being additive under Lorentz transformations along z. This means that under Lorentz transformations along z, differences in rapidity, dy, are invariant. A quantity of similar interest is pseudorapidity,

$$\eta = -\ln \left(\tan \frac{\theta}{2} \right) \tag{A.3}$$

where θ is the particle's emission angle relative to the beam axis. For relativistic particles, i.e. $v/c \approx 1$, we have $\eta \approx y$, while for massless particles $\eta = y$.

The kinematic varible η is commonly used to characterize particle trajectories because, unlike y, it does not require knowledge of the particle's mass. Also, in a high-energy environment such as relativistic heavy ion collisions, conditions are such ($v/c \approx 1$) that that η often provides a good approximation of y.

APPENDIX B

Upper Limit Calculation

In Chapter 3 we gave a description of the J/ψ signal extraction. We concluded that the quality of the signal in central events is such that it would best serve as the basis for an upper limit estimate of the yield in that centrality bin. In this appendix we give a detailed account of a 90% confidence level upper limit for the measured yield in central events. Here, this is achieved with the Bayesian approach. In Bayesian statistics, one can speak of a probability density function (p.d.f.), $p(\theta|\mathbf{x})$, of a parameter θ, which expresses one's state of knowledge, or *degree of belief*, about where its true value lies in a certain region given the vector of data $\mathbf{x}$. This is obtained by using Bayes' theorem [Eid04],

$$p(\theta|\mathbf{x}) = \frac{L(\mathbf{x}|\theta)\pi(\theta)}{\int L(\mathbf{x}|\theta')\pi(\theta')d\theta'}, \tag{B.1}$$

where $L(\mathbf{x}|\theta)$ is the likelihood function, i.e., the joint p.d.f. for the data given a certain value of θ taken in the experiment, and $\pi(\theta)$ is the prior p.d.f. for θ. Now, as is the case of real experiments, the parameter of interest must be constrained (on physical grounds) to be non-negative, so the prior p.d.f. can be set to zero for negative values. We are also interested in the case of a Poisson variable n which counts signal events with an unknown mean s as well as a background with mean b, assumed to be known. For the signal mean s one often uses the prior

$$\pi(s) = \begin{cases} 0 & s < 0 \\ 1 & s \geq 0 \end{cases} . \tag{B.2}$$

Using the likelihood function for Poisson distributed n,

$$L(n|s) = \frac{(s+b)^n}{n!} \exp -(s+b), \tag{B.3}$$

along with with the prior p.d.f (Equation B.2) in Equation B.1 gives the posterior density for s. An upper limit s_{up} at confidence level $1-\alpha$ can be obtained by requiring

$$1 - \alpha = \int_{-\infty}^{s_{up}} p(s|n)ds = \frac{\int_{-\infty}^{s_{up}} L(n|s)\pi(s)ds}{\int_{-\infty}^{\infty} L(n|s)\pi(s)ds}, \tag{B.4}$$

where the lower limit of integration is effectively zero because of the cut-off in $\pi(s)$. By relating the integrals in Equation B.4 to incomplete gamma functions, the equation reduces to

$$\alpha = \exp\left(-s_{up}\right) \frac{\sum_{m=0}^{n} (s_{up}+b)^m/m!}{\sum_{m=0}^{n} b^m/m!}, \tag{B.5}$$

which must be solved numerically for the limit s_{up}. In the mass window of interest, the same-event distribution contains 5065 counts while the (normalized) mixed-event background contains 4984 counts. Setting $n = 5065$ and $b = 4984$, the solution to Equation B.5 is illustrated in Figure B.1. The intercept of the left and right sides of Equation B.5 represents the 90% confidence level upper limit for the raw yield in central events, i.e. 178 raw counts. Correcting this for efficiency and acceptance, as described in Chapter 4, we arrive at 4139+535 (*sys*) as the corrected yield in the 0-20% most central events. The systematic error quoted (∼13%) here is described in detail in Chapter 5.

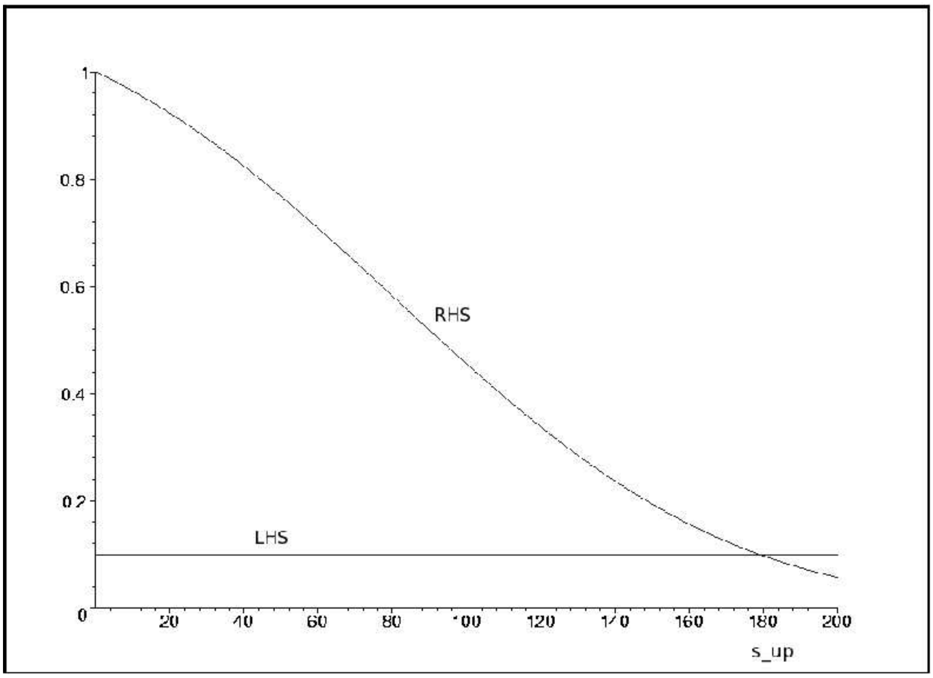

Figure B.1: The left hand side (LHS) of Equation B.5 is represented by the horizontal line while the right hand side (RHS) is represented by the monotonically decreasing curve. The intercept represents the upper limit on the raw yield with a 90% confidence level.

APPENDIX C

The STAR Collaboration

J. Adams[2], M.M. Aggarwal[29], Z. Ahammed[44],J. Amonett[19], B.D. Anderson[19], M. Anderson[6],D. Arkhipkin[12], G.S. Averichev[11], Y. Bai[27],J. Balewski[16], O. Barannikova[32], L.S. Barnby[2],J. Baudot[17], S. Bekele[28], V.V. Belaga[11],A. Bellingeri-Laurikainen[39], R. Bellwied[47],B.I. Bezverkhny[49], S. Bhardwaj[34], A. Bhasin[18],A.K. Bhati[29], H. Bichsel[46], J. Bielcik[49],J. Bielcikova[49], L.C. Bland[3], C.O. Blyth[2],S-L. Blyth[21], B.E. Bonner[35], M. Botje[27],J. Bouchet[39], A.V. Brandin[25], A. Bravar[3],M. Bystersky[10], R.V. Cadman[1], X.Z. Cai[38],H. Caines[49], M. Calderon[6], J. Castillo[27],O. Catu[49], D. Cebra[6], Z. Chajecki[28],P. Chaloupka[10], S. Chattopadhyay[44], H.F. Chen[37],J.H. Chen[38], Y. Chen[7], J. Cheng[42], M. Cherney[9],A. Chikanian[49], H.A. Choi[33], W. Christie[3],J.P. Coffin[17], T.M. Cormier[47], M.R. Cosentino[36],J.G. Cramer[46], H.J. Crawford[5], D. Das[44], S. Das[44],M. Daugherity[41], M.M. de Moura[36], T.G. Dedovich[11],M. DePhillips[3], A.A. Derevschikov[31], L. Didenko[3],T. Dietel[13], P. Djawotho[16], S.M. Dogra[18],W.J. Dong[7], X. Dong[37], J.E. Draper[6], F. Du[49],V.B. Dunin[11], J.C. Dunlop[3], M.R. Dutta Mazumdar[44], V. Eckardt[23], W.R. Edwards[21], L.G. Efimov[11], V. Emelianov[25], J. Engelage[5], G. Eppley[35], B. Erazmus[39], M. Estienne[17], P. Fachini[3], R. Fatemi[22], J. Fedorisin[11], K. Filimonov[21], P. Filip[12], E. Finch[49], V. Fine[3], Y. Fisyak[3], J. Fu[48], C.A. Gagliardi[40], L. Gaillard[2], J. Gans[49], M.S. Ganti[44], V. Ghazikhanian[7], P. Ghosh[44], J.E. Gonzalez[7], Y.G. Gorbunov[9], H. Gos[45], O. Grebenyuk[27], D. Grosnick[43], S.M. Guertin[7], K.S.F.F. Guimaraes[36], Y. Guo[47], N. Gupta[18], T.D. Gutierrez[6], B. Haag[6], T.J. Hallman[3], A. Hamed[47], J.W. Harris[49], W. He[16], M. Heinz[49], T.W. Henry[40], S. Hepplemann[30], B. Hippolyte[17], A. Hirsch[32], E. Hjort[21], G.W. Hoffmann[41], M.J. Horner[21], H.Z. Huang[7], S.L.

Huang[37], E.W. Hughes[4], T.J. Humanic[28], G. Igo[7], P. Jacobs[21], W.W. Jacobs[16], P. Jakl[10], F. Jia[20], H. Jiang[7], P.G. Jones[2], E.G. Judd[5], S. Kabana[39], K. Kang[42], J. Kapitan[10], M. Kaplan[8], D. Keane[19], A. Kechechyan[11], V.Yu. Khodyrev[31], B.C. Kim[33], J. Kiryluk[22], A. Kisiel[45], E.M. Kislov[11], S.R. Klein[21], D.D. Koetke[43], T. Kollegger[13], M. Kopytine[19], L. Kotchenda[25], V. Kouchpil[10], K.L. Kowalik[21], M. Kramer[26], P. Kravtsov[25], V.I. Kravtsov[31], K. Krueger[1], C. Kuhn[17], A.I. Kulikov[11], A. Kumar[29], A.A. Kuznetsov[11], M.A.C. Lamont[49], J.M. Landgraf[3], S. Lange[13], S. LaPointe[47], F. Laue[3], J. Lauret[3], A. Lebedev[3], R. Lednicky[12], C-H. Lee[33], S. Lehocka[11], M.J. LeVine[3], C. Li[37], Q. Li[47], Y. Li[42], G. Lin[49], S.J. Lindenbaum[26], M.A. Lisa[28], F. Liu[48], H. Liu[37], J. Liu[35], L. Liu[48], Z. Liu[48], T. Ljubicic[3], W.J. Llope[35], H. Long[7], R.S. Longacre[3], M. Lopez-Noriega[28], W.A. Love[3], Y. Lu[48], T. Ludlam[3], D. Lynn[3], G.L. Ma[38], J.G. Ma[7], Y.G. Ma[38], D. Magestro[28], D.P. Mahapatra[14], R. Majka[49], L.K. Mangotra[18], R. Manweiler[43], S. Margetis[19], C. Markert[19], L. Martin[39], H.S. Matis[21], Yu.A. Matulenko[31], C.J. McClain[1], T.S. McShane[9], Yu. Melnick[31], A. Meschanin[31], M.L. Miller[22], N.G. Minaev[31], S. Mioduszewski[40], C. Mironov[19], A. Mischke[27], D.K. Mishra[14], J. Mitchell[35], B. Mohanty[44], L. Molnar[32], C.F. Moore[41], D.A. Morozov[31], M.G. Munhoz[36], B.K. Nandi[15], C. Nattrass[49], T.K. Nayak[44], J.M. Nelson[2], P.K. Netrakanti[44], V.A. Nikitin[12], L.V. Nogach[31], S.B. Nurushev[31], G. Odyniec[21], A. Ogawa[3], V. Okorokov[25], M. Oldenburg[21], D. Olson[21], M. Pachr[10], S.K. Pal[44], Y. Panebratsev[11], S.Y. Panitkin[3], A.I. Pavlinov[47], T. Pawlak[45], T. Peitzmann[27], V. Perevoztchikov[3], C. Perkins[5], W. Peryt[45], V.A. Petrov[47], S.C. Phatak[14], R. Picha[6], M. Planinic[50], J. Pluta[45], N. Poljak[50], N. Porile[32], J. Porter[46], A.M. Poskanzer[21], M. Potekhin[3], E. Potrebenikova[11], B.V.K.S. Potukuchi[18], D. Prindle[46], C. Pruneau[47], J. Putschke[21], G. Rakness[30], R. Raniwala[34], S. Raniwala[34], R.L. Ray[41], S.V. Razin[11], J. Reinnarth[39], D. Relyea[4], F. Retiere[21], A. Ridiger[25], H.G. Ritter[21], J.B. Roberts[35], O.V. Rogachevskiy[11], J.L. Romero[6], A. Rose[21], C. Roy[39], L. Ruan[21], M.J. Russcher[27], R. Sahoo[14], I. Sakrejda[21], S. Salur[49], J. Sandweiss[49], M. Sarsour[40], P.S. Sazhin[11], J. Schambach[41], R.P. Scharenberg[32], N. Schmitz[23], K. Schweda[21], J. Seger[9], I. Selyuzhenkov[47], P. Seyboth[23], A. Shabetai[21], E. Shahaliev[11], M. Shao[37], M. Sharma[29], W.Q. Shen[38], S.S. Shimanskiy[11], E

Sichtermann[21], F. Simon[22], R.N. Singaraju[44], N. Smirnov[49], R. Snellings[27], G. Sood[43], P. Sorensen[3], J. Sowinski[16], J. Speltz[17], H.M. Spinka[1], B. Srivastava[32], A. Stadnik[11], T.D.S. Stanislaus[43], R. Stock[13], A. Stolpovsky[47], M. Strikhanov[25], B. Stringfellow[32], A.A.P. Suaide[36], E. Sugarbaker[28], M. Sumbera[10], Z. Sun[20], B. Surrow[22], M. Swanger[9], T.J.M. Symons[21], A. Szanto de Toledo[36], A. Tai[7], J. Takahashi[36], A.H. Tang[3], T. Tarnowsky[32], D. Thein[7], J.H. Thomas[21], A.R. Timmins[2], S. Timoshenko[25], M. Tokarev[11], T.A. Trainor[46], S. Trentalange[7], R.E. Tribble[40], O.D. Tsai[7], J. Ulery[32], T. Ullrich[3], D.G. Underwood[1], G. Van Buren[3], N. van der Kolk[27], M. van Leeuwen[21], A.M. Vander Molen[24], R. Varma[15], I.M. Vasilevski[12], A.N. Vasiliev[31], R. Vernet[17], S.E. Vigdor[16], Y.P. Viyogi[44], S. Vokal[11], S.A. Voloshin[47], W.T. Waggoner[9], F. Wang[32], G. Wang[19], J.S. Wang[20], X.L. Wang[37], Y. Wang[42], J.W. Watson[19], J.C. Webb[16], G.D. Westfall[24], A. Wetzler[21], C. Whitten Jr.[7], H. Wieman[21], S.W. Wissink[16], R. Witt[49], J. Wood[7], J. Wu[37], N. Xu[21], Q.H. Xu[21], Z. Xu[3], P. Yepes[35], I-K. Yoo[33], V.I. Yurevich[11], W. Zhan[20], H. Zhang[3], W.M. Zhang[19], Y. Zhang[37], Z.P. Zhang[37], Y. Zhao[37], C. Zhong[38], R. Zoulkarneev[12], Y. Zoulkarneeva[12], A.N. Zubarev[11], J.X. Zuo[38]

(STAR Collaboration)

[1]Argonne National Laboratory, Argonne, Illinois 60439

[2]University of Birmingham, Birmingham, United Kingdom

[3]Brookhaven National Laboratory, Upton, New York 11973

[4]California Institute of Technology, Pasadena, California 91125

[5]University of California, Berkeley, California 94720

[6]University of California, Davis, California 95616

[7]University of California, Los Angeles, California 90095

[8]Carnegie Mellon University, Pittsburgh, Pennsylvania 15213

[9]Creighton University, Omaha, Nebraska 68178

[10]Nuclear Physics Institute AS CR, 250 68 Řež/Prague, Czech Republic

[11]Laboratory for High Energy (JINR), Dubna, Russia

[12]Particle Physics Laboratory (JINR), Dubna, Russia

[13]University of Frankfurt, Frankfurt, Germany

[14]Institute of Physics, Bhubaneswar 751005, India

[15]Indian Institute of Technology, Mumbai, India

[16]Indiana University, Bloomington, Indiana 47408

[17]Institut de Recherches Subatomiques, Strasbourg, France

[18]University of Jammu, Jammu 180001, India

[19]Kent State University, Kent, Ohio 44242

[20]Institute of Modern Physics, Lanzhou, China

[21]Lawrence Berkeley National Laboratory, Berkeley, California 94720

[22]Massachusetts Institute of Technology, Cambridge, MA 02139-4307

[23]Max-Planck-Institut für Physik, Munich, Germany

[24]Michigan State University, East Lansing, Michigan 48824

[25]Moscow Engineering Physics Institute, Moscow Russia

[26]City College of New York, New York City, New York 10031

[27]NIKHEF and Utrecht University, Amsterdam, The Netherlands

[28]Ohio State University, Columbus, Ohio 43210

[29]Panjab University, Chandigarh 160014, India

[30]Pennsylvania State University, University Park, Pennsylvania 16802

[31]Institute of High Energy Physics, Protvino, Russia

[32]Purdue University, West Lafayette, Indiana 47907

[33]Pusan National University, Pusan, Republic of Korea

[34]University of Rajasthan, Jaipur 302004, India

[35]Rice University, Houston, Texas 77251

[36]Universidade de Sao Paulo, Sao Paulo, Brazil

[37]University of Science & Technology of China, Hefei 230026, China

[38]Shanghai Institute of Applied Physics, Shanghai 201800, China

[39]SUBATECH, Nantes, France

[40]Texas A&M University, College Station, Texas 77843

[41]University of Texas, Austin, Texas 78712

[42]Tsinghua University, Beijing 100084, China

[43]Valparaiso University, Valparaiso, Indiana 46383

[44]Variable Energy Cyclotron Centre, Kolkata 700064, India

[45]Warsaw University of Technology, Warsaw, Poland

[46]University of Washington, Seattle, Washington 98195

[47]Wayne State University, Detroit, Michigan 48201

[48]Institute of Particle Physics, CCNU (HZNU), Wuhan 430079, China

[49]Yale University, New Haven, Connecticut 06520

[50]University of Zagreb, Zagreb, HR-10002, Croatia

APPENDIX D

Acronyms

ADC Analog to Digital Conversion.

AGS Alternating Gradient Synchrotron.

ALEPH ALEPH experiment at CERN. ALEPH was one of the large detectors at the LEP.

BBC Beam Beam Counter. The BBCs are scintillating tiles used to trigger on charged particle multiplicity in the forward rapidity region.

BEMC Barrel Electromagnetic Calorimeter. The BEMC provides electromagnetic calorimetry in the mid-rapidity region.

BNL Brookhaven National Laboratory.

BRAHMS Broad Range Hadron Magnetic Spectrometers Experiment at RHIC.

CDF Collider Detector at Fermilab.

CERN l'Organisation Europèenne pour la Recherche Nucléaire.

CPU Central Processing Unit.

CTB Central Trigger Barrel. The CTB is made of scintillating tiles and is used to trigger on charged particle multiplicity.

DAQ Data Aquisition System.

DCA Distance of closest approach. DCA is most commonly calculated between two helices, a helix and the beam line, or a helix and a point.

DIS Deep Inelastic Scattering.

EEMC Endcap Electromagnetic Calorimeter. The EEMC provides electromagnetic calorimetry in the forward-rapidity region.

EOS Equation Of State.

EVR Default STAR Vertex Finder. EVR is used for heavy ion collisions with charged particle multiplicities greater than $\sim$20.

FPD Forward Pion Detector. The FPD is a prototype for the endcap electromagnetic calorimeter.

FTPC Forward Time Projection Chamber. The FTPC provides charged particle tracking in the forward and backward rapidity regions.

GEANT GEometry ANd Tracking.

HFT Heavy Flavor Tracker. Proposed detector that will extend STAR's capability to measure heavy flavor production.

IFC STAR TPC Inner Field Cage.

LEP Large Electron Positron Collider. LEP ran for over twenty years and was home to many major discoveries, including the W and Z bosons.

LMV Low Multiplicity Vertex Finder. LMV is used for primary vertex finding in extremely low multiplicity collisions.

LO Leading Order.

MCI Monte Carlo Integration.

MCG Monte Carlo Glauber.

MWPC Multi Wire Proportional Counter. The MWPC is part of the TPC readout system.

NA49 North Area 49th Heavy Ion Experiment at CERN.

NLO Next to Leading Order.

NNLO Next to Next to Leading Order.

OFC STAR TPC Outer Field Cage.

PHENIX Pioneering High Energy Nuclear Experiment.

PHOBOS The original experiment MARS (Modular Array for RHIC Spectroscopy) was not approved. A similar setup under the name of one of the moons of Mars was later approved.

PMT Photo Multiplier Tube.

ppLMV Proton-Proton Low Multiplicity Vertex Finder. ppLMV is used for vertex finding in p+p collisions.

pQCD Perturbative Quantum Chromodynamics. pQCD is a perturbative field theory solution to QCD.

QCD Quantum Chromodynamics. QCD is the theory of strongly interacting particles.

QED Quantum Electrodynamics.

QGP Quark Gluon Plasma. The minimal definition of a QGP is a deconfined medium where color charges flow freely. A formal definition is provided in the text.

RHIC Relativistic Heavy Ion Collider.

SLAC Stanford Linear Accelerator Complex.

SM Standard Model.

SSD Silicon Strip Detector.

STAR Solenoidal Tracker at RHIC.

SVT Silicon Vertex Tracker. The SVT provides high precision tracking information close to the interaction point.

TOF Time of Flight detector that will provide full azimuthal coverage at mid-rapidity.

TOFp Time of Flight patch detector based on scintillation technology, located at the seven o'clock position in the east portion of STAR.

TOFr Time of Flight patch detector based on multi-gap resistive plate chamber technology, located at the five o'clock position in the east portion of STAR.

TPC Time Projection Chamber. The TPC is STAR's main tracking detector.

TPT Time Projection Chamber Tracker. TPT is the current track finding software package for the STAR TPC.

TRS Time Projection Chamber Response Simulator. TRS is the software package that simulates the full detector response to charged particles.

ZDC Zero Degree Calorimeter. A ZDC primarily detects neutrons that are remnants of the beam break up.

References

[ABD05] W. M. Alberico, A. Beraudo, A. De Pace, and A. Molinari. “Heavy quark bound states above T(c).” *Phys. Rev.*, **D72**:114011, 2005.

[Abe03] J. Abele et al. “The laser system for the STAR time projection chamber.” *Nucl. Instrum. Meth.*, **A499**:692–702, 2003.

[Abr00] M. C. Abreu et al. “Evidence for deconfinement of quarks and gluons from the J/psi suppression pattern measured in Pb Pb collisions at the CERN-SPS.” *Phys. Lett.*, **B477**:28–36, 2000.

[ABR03] A. Andronic, P. Braun-Munzinger, K. Redlich, and J. Stachel. “Statistical hadronization of charm in heavy-ion collisions at SPS, RHIC and LHC.” *Phys. Lett.*, **B571**:36–44, 2003.

[Ack03] K. H. Ackermann et al. “The forward time projection chamber (FTPC) in STAR.” *Nucl. Instrum. Meth.*, **A499**:713–719, 2003.

[Ada05a] J. Adams et al. “Experimental and theoretical challenges in the search for the quark gluon plasma: The STAR collaboration’s critical assessment of the evidence from RHIC collisions.” *Nucl. Phys.*, **A757**:102–183, 2005.

[Ada05b] J. Adams et al. “Open charm yields in d + Au collisions at s(NN)**(1/2) = 200-GeV.” *Phys. Rev. Lett.*, **94**:062301, 2005.

[Adl01] C. Adler et al. “The RHIC zero-degree calorimeters.” *Nucl. Instrum. Meth.*, **A461**:337–340, 2001.

[Adl04] S. S. Adler et al. “J/psi production in Au Au collisions at s(NN)**(1/2) = 200- GeV at the Relativistic Heavy Ion Collider.” *Phys. Rev.*, **C69**:014901, 2004.

[Adl05] S. S. Adler et al. “Centrality dependence of charm production from single electrons measurement in Au + Au collisions at s(NN)**(1/2) = 200-GeV.” *Phys. Rev. Lett.*, **94**:082301, 2005.

[Adl06a] S. S. Adler et al. “J/psi production and nuclear effects for d + Au and p + p collisions at s(NN)**(1/2) = 200-GeV.” *Phys. Rev. Lett.*, **96**:012304, 2006.

[Adl06b] S. S. Adler et al. “Nuclear modification of electron spectra and implications for heavy quark energy loss in Au + Au collisions at s(NN)**(1/2) = 200-GeV.” *Phys. Rev. Lett.*, **96**:032301, 2006.

[Adl06c] S. S. Adler et al. “Single electrons from heavy flavor decays in p + p collisions at s**(1/2) = 200-GeV.” *Phys. Rev. Lett.*, **96**:032001, 2006.

[Agg03] M. M. Aggarwal et al. “The STAR photon multiplicity detector.” *Nucl. Instrum. Meth.*, **A499**:751–761, 2003.

[AH04] M. Asakawa and T. Hatsuda. “Charm cluster in quark gluon plasma?” *Nucl. Phys.*, **A738**:249–253, 2004.

[Ale05] B. Alessandro et al. “A new measurement of J/psi suppression in Pb - Pb collisions at 158-GeV per nucleon.” *Eur. Phys. J.*, **C39**:335–345, 2005.

[All03] C. E. Allgower et al. “The STAR endcap electromagnetic calorimeter.” *Nucl. Instrum. Meth.*, **A499**:740–750, 2003.

[Aln86] G. J. Alner et al. “ANTI-PROTON - PROTON CROSS-SECTIONS AT 200-GeV AND 900-GeV center-of-mass ENERGY.” *Z. Phys.*, **C32**:153, 1986.

[And03] M. Anderson et al. “The STAR time projection chamber: A unique tool for studying high multiplicity events at RHIC.” *Nucl. Instrum. Meth.*, **A499**:659–678, 2003.

[Ant92] L. Antoniazzi et al. *Phys. Rep.*, **D46**:4828, 1992.

[Arn03] L. Arnold et al. “The STAR silicon strip detector (SSD).” *Nucl. Instrum. Meth.*, **A499**:652–658, 2003.

[Bed03] M. Beddo et al. “The STAR barrel electromagnetic calorimeter.” *Nucl. Instrum. Meth.*, **A499**:725–739, 2003.

[Bel03] R. Bellwied et al. “The STAR silicon vertex tracker: A large area silicon drift detector.” *Nucl. Instrum. Meth.*, **A499**:640–651, 2003.

[Ber03] F. Bergsma et al. “The STAR detector magnet subsystem.” *Nucl. Instrum. Meth.*, **A499**:633–639, 2003.

[Bet03] Siegfried Bethke. “alpha(s) 2002.” *Nucl. Phys. Proc. Suppl.*, **121**:74–81, 2003.

[BHH] R. Brun, R. Hagelberg, M. Hansroul, and J. C. Lassalle. “GEANT: SIMULATION PROGRAM FOR PARTICLE PHYSICS EXPERIMENTS. USER GUIDE AND REFERENCE MANUAL.” CERN-DD-78-2-REV.

[BHS99] P. Braun-Munzinger, I. Heppe, and J. Stachel. "Chemical equilibration in Pb + Pb collisions at the SPS." *Phys. Lett.*, **B465**:15–20, 1999.

[Bic02] H. Bichsel. "Comparison of Bethe-Bloch and Bichsel Functions." Technical report, 2002.

[Bie03] F. S. Bieser et al. "The STAR trigger." *Nucl. Instrum. Meth.*, **A499**:766–777, 2003.

[Bon03] B. Bonner et al. "A single Time-of-Flight tray based on multigap resistive plate chambers for the STAR experiment at RHIC." *Nucl. Instrum. Meth.*, **A508**:181–184, 2003.

[Bos97] R. Bossingham et al. "STAR Simulation and Analysis Software Design." Technical report, 1997.

[BR94] W. Blum and L. Rolandi. *Particle Detection With Drift Chambers.* Springer Verlag, Berlin, second edition, 1994.

[BS00] P. Braun-Munzinger and J. Stachel. "(Non)thermal aspects of charmonium production and a new look at J/psi suppression." *Phys. Lett.*, **B490**:196–202, 2000.

[BZ] (ed.) Braun-Munzinger, P. and (ed.) Zilges, A. "Nuclei and nucleons. Proceedings, International Symposium on the occasion of Achim Richter's 60th birthday, Darmstadt, Germany, October 11-13, 2000." Prepared for International Symposium on the Occasion of Achim Richter's 60th Birthday: Nuclei and Nucleons, Darmstadt, Germany, 11-13 Oct 2000.

[CNV05] Matteo Cacciari, Paolo Nason, and Ramona Vogt. "QCD predictions for charm and bottom production at RHIC." *Phys. Rev. Lett.*, **95**:122001, 2005.

[Cra78] N.S. Craigie. *Phys. Rep.*, **47**:1, 1978.

[DC] P. Djawotho and M. Calderon. Private Communications.

[DFN84] D. Drijard, H. G. Fischer, and T. Nakada. "STUDY OF EVENT MIXING AND ITS APPLICATION TO THE EXTRACTION OF RESONANCE SIGNALS." *Nucl. Instr. Meth.*, **A225**:367, 1984.

[Djo05] M. Djordjevic. "Heavy Flavor Observables at RHIC.", 2005. Heavy Ion Tea Seminar, Lawrence Berkeley National Laboratory.

[DKW04] Saumen Datta, Frithjof Karsch, Soenke Wissel, Peter Petreczky, and Ines Wetzorke. "Charmonia at finite momenta in a deconfined plasma." 2004.

[Don05] X. Dong. *Single Electron Transverse Momentum and Azimuthal Anisotropy Distributions: Charm Hadron Production at RHIC.* PhD thesis, University of Science and Technology of China, 2005.

[Dun] James Dunlop. Private Communications.

[Eid04] S. Eidelman et al. "Review of particle physics." *Phys. Lett.*, **B592**:1, 2004.

[GG99] Marek Gazdzicki and Mark I. Gorenstein. "Evidence for statistical production of J/psi mesons in nuclear collisions at the CERN SPS." *Phys. Rev. Lett.*, **83**:4009–4012, 1999.

[GKS02] M. I. Gorenstein, A. P. Kostyuk, Horst Stoecker, and W. Greiner. "J/psi suppression and enhancement in Au + Au collisions at the BNL RHIC." *Phys. Lett.*, **B524**:265–272, 2002.

[Gon01] J. Gonzalez. "Calibration of the STAR Zero Degree Calorimeters." Technical report, 2001.

[GR01] L. Grandchamp and R. Rapp. "Thermal versus direct J/psi production in ultrarelativistic heavy-ion collisions." *Phys. Lett.*, **B523**:60–66, 2001.

[Hag00] Kevin L. Haglin. "Charmonium dissociation in hadronic matter." *Phys. Rev.*, **C61**:031902, 2000.

[Har94] J. W. Harris. "The STAR experiment at the relativistic heavy ion collider." *Nucl. Phys.*, **A566**:277c–285c, 1994.

[HKP01] Jorg Hufner, Boris Z. Kopeliovich, and Alberto Polleri. "Excitation of color degrees of freedom of nuclear matter and J/psi suppression." *Eur. Phys. J.*, **A11**:457–465, 2001.

[HX] Huan Z. Huang and Zhangbu Xu. Private Communications.

[Jia05] H. Jiang. *Strange Hadron ($K^0_S, \Lambda, and \Xi$) Production in d+Au Collisions at $\sqrt{s_{NN}}$ = 200 GeV at RHIC.* PhD thesis, Univeristy of California, Los Angeles, 2005.

[Joh02] I. Johnson. *Photon and Neutral Pion Production in Au+Au Collisions at $\sqrt{s_{NN}} = 130$ GeV.* PhD thesis, University of California, Davis, 2002.

[Kar02] F. Karsh. *Lecture Notes in Physics*, **583**:209, 2002.

[KKL00] Olaf Kaczmarek, Frithjof Karsch, Edwin Laermann, and Martin Lutgemeier. “Heavy quark potentials in quenched QCD at high temperature.” *Phys. Rev.*, **D62**:034021, 2000.

[KKS05] F. Karsch, D. Kharzeev, and H. Satz. “Sequential charmonium dissociation.” 2005.

[KNS97] D. Kharzeev, M. Nardi, and H. Satz. “The transverse momentum dependence of anomalous J/psi suppression.” *Phys. Lett.*, **B405**:14–19, 1997.

[Koc03] L. Kochenda et al. “STAR TPC gas system.” *Nucl. Instrum. Meth.*, **A499**:703–712, 2003.

[Kop74] G. I. Kopylov. “Like particle correlations as a tool to study the multiple production mechanism.” *Phys. Lett.*, **B50**:472–474, 1974.

[KS86] K. Kanaya and H. Satz. “CORRELATION AND SCREENING IN FINITE TEMPERATURE SU(2) GAUGE THEORY.” *Phys. Rev.*, **D34**:3193, 1986.

[KS94] D. Kharzeev and H. Satz. “Quarkonium interactions in hadronic matter.” *Phys. Lett.*, **B334**:155–162, 1994.

[Las97] B. Lasiuk. “Particle Identification at STAR.” Technical report, 1997.

[Leb02] A. Lebedev. “A laser calibration system for the STAR TPC.” *Nucl. Instrum. Meth.*, **A478**:163–165, 2002.

[Lei06] M. Leitch. “Quarkonia Production in pp, p(d)A, and AA Collisions.”, 2006. Heavy Ion Tea Seminar, Lawrence Berkeley National Laboratory.

[LH94] D. L’Hote. “About Resonance signal extraction from multiparticle data: combinatorics and event mixing methods.” *Nucl. Instrum. Meth.*, **A337**:544–556, 1994.

[Lis96] M.A. Lisa. “The STAR-TPC Clusterfinder/Hitfinder.” Technical report, 1996.

[Llo04a] W. Llope et al. “Proposal for a Large Area Time of Flight System for STAR.” Technical report, 2004.

[Llo04b] W. J. Llope et al. “The TOFp/pVPD time-of-flight system for STAR.” *Nucl. Instrum. Meth.*, **A522**:252–273, 2004.

[Lon02] H. Long. *Mid-rapidity* Λ *and* $\overline{\Lambda}$ *Production in Au+Au Collisions at the Relativistic Heavy Ion Collider.* PhD thesis, Univeristy of California, Los Angeles, 2002.

[MC92] S. Margetis and D. Cebra. “Main Vertex Reconstruction in STAR.” Technical report, 1992.

[Mil03] M. Miller. *Measurement of Jets and Jet Quenching at RHIC.* PhD thesis, Yale University, 2003.

[Mor05] R. Morrin et al. “Charmonium spectral functions in N(f) = 2 QCD.” *PoS*, **LAT2005**:176, 2005.

[MOU01] Hideo Matsufuru, Tetsuya Onogi, and Takashi Umeda. “Numerical study of O(a) improved Wilson quark action on anisotropic lattice.” *Phys. Rev.*, **D64**:114503, 2001.

[MS86] T. Matsui and H. Satz. “J / psi SUPPRESSION BY QUARK - GLUON PLASMA FORMATION.” *Phys. Lett.*, **B178**:416, 1986.

[MS94] J.T. Mitchell and I.M. Sakrejda. “Tracking for the STAR TPC: Documentation and User’s Guide.” Technical report, 1994.

[Oza] Satoshi Ozaki. “RHIC project.” Presented at 1991 IEEE Particle Accelerator Conf., San Francisco, CA, May 6-9, 1991.

[Per05] H. Pereira Da Costa. “PHENIX results on J/psi production in Au + Au and Cu + Cu collisions at s(NN)**(1/2) = 200-GeV.” 2005.

[PV98] Arthur M. Poskanzer and S. A. Voloshin. “Methods for analyzing anisotropic flow in relativistic nuclear collisions.” *Phys. Rev.*, **C58**:1671–1678, 1998.

[QR79] C. Quigg and J.L. Rosner. *Phys. Rep.*, **56**:167, 1979.

[Sha02] M. Shao et al. “Beam test results of two kinds of multi-gap resistive plate chambers.” *Nucl. Instrum. Meth.*, **A492**:344–350, 2002.

[Sha05] R. Shahoyan et al. “Study of dimuon production in indium indium collisions with the NA60 experiment.” 2005.

[Shu78] Edward V. Shuryak. "QUARK - GLUON PLASMA AND HADRONIC PRODUCTION OF LEPTONS, PHOTONS AND PSIONS." *Phys. Lett.*, **B78**:150, 1978.

[SMS06] Torbjorn Sjostrand, Stephen Mrenna, and Peter Skands. "PYTHIA 6.4 physics and manual." 2006.

[Sor] Paul Sorensen. Private Communications.

[The] R. L. Thews. "SOME THEORETICAL ASPECTS OF J / psi SUPPRESSION." Presented at 3rd Conf. on Intersections between Particle and Nuclear Physics, Rockport, ME, May 14-19, 1988.

[The05] R. L. Thews. "In-medium formation of J/psi as a probe of charm quark thermalization." 2005.

[Tho] James Thomas. Private Communications.

[TSR01] Robert L. Thews, Martin Schroedter, and Johann Rafelski. "Enhanced J/psi production in deconfined quark matter." *Phys. Rev.*, **C63**:054905, 2001.

[Wie06] H. Wieman et al. "A Stand-alone Heavy Flavor Tracker for STAR." Technical report, 2006.

[Won05a] Cheuk-Yin Wong. "Effects of dynamical quarks on the stability of heavy quarkonia in quark-gluon plasma." 2005.

[Won05b] Cheuk-Yin Wong. "Heavy quarkonia in quark gluon plasma." *Phys. Rev.*, **C72**:034906, 2005.

[Xua] Nu Xu. Private Communications.

[Xub] Zhangbu Xu. Private Communications.

[Yam01] G. Yamamoto. *Phi Meson Production in Au+Au Collisions at the Relativistic Heavy Ion Collider.* PhD thesis, University of California, Los Angeles, 2001.

[Zha06] Y. Zhang. "Charm→lepton spectra in Au+Au collision at RHIC.", 2006. Contributed Talk, Strange Quark Matter 2006, UCLA.

[ZZX05] Xiang-lei Zhu, Peng-fei Zhuang, and Nu Xu. "J/psi transport in QGP and p(t) distribution at SPS and RHIC." *Phys. Lett.*, **B607**:107–114, 2005.